

Acknowledgments

I would like to express my gratitude to my promotor, Prof Dr. François Peeters, whose expertise, understanding, and patience (in my case he probably needed a lot!) accompanied me for four years. I am indebted with him for giving me the opportunity to pursue a PhD in his group. I appreciate his vast knowledge and skill in many areas and, above all, his humane qualities.

I would like to thank Dr. Joseph Betouras, whose help, support and friendship were fundamental at the beginning of my PhD career.

My gratitude goes to my family and to all my friends here in Antwerp and in Italy. The list with all names will be too long and I do not want to offend anybody putting his name before or after the name of someone else. I must also acknowledge the members of my PhD jury.

I would like to conclude with a quotation from 'The unbearable lightness of being' by Milan Kundera: "In the sunset of dissolution, everything is illuminated by the aura of nostalgia, even the guillotine", just to say that no matter how wonderful or terrible my stay in Belgium was, no matter how good or bad relationships I could establish with the people I met, I will always remember with deep affection and infinite nostalgia this four years and all the persons who I was in contact with. This is the reason why I would like to express my earnest gratitude to everybody and everything, that were a fundamental part of my life for several years.

My PhD work was supported by the EU Research Training Network "Surface Electrons on Mesoscopic Structures", the Flemish Science Foundation (FWO-VI), the Belgian Science Policy IUAP-VI and the "Onderzoeksraad van de Universiteit Antwerpen" (GOA).

Contents

1	Introduction	1
1.1	Wigner crystallization	2
1.2	Quasi-one-dimensional experimental systems	5
1.2.1	Electrons above liquid helium	5
1.2.2	Colloidal systems	8
1.2.3	Complex plasmas	12
1.2.4	Other systems	17
1.3	Related systems	21
1.3.1	Charge density waves	21
1.3.2	Vortices in superfluids and type II superconductors	23
1.3.3	Biological systems	26
1.4	General properties of driven systems	28
2	Model System and Numerical Approach	35
2.1	General Hamiltonian and the classical limit	36
2.2	Scalability and dimensionless units	37
2.3	Energy Minimization	40
2.3.1	Monte Carlo simulations	41
2.3.2	The simulated annealing approach	42

2.4	Molecular Dynamics	43
2.4.1	Different algorithms for the integration of Newton's equations	44
2.4.2	Langevin Molecular Dynamics	47
2.5	Periodic boundary conditions	49
2.6	Short range potentials: smart calculation techniques	50
3	Ground state configuration: the chain-like system	53
3.1	Model and methods	55
3.2	Ground state configurations	56
3.3	Structural transitions	60
3.4	Limit of short range interaction and large density	63
3.5	Conclusions	63
4	Normal modes	65
4.1	Natural modes	66
4.1.1	Natural modes in the absence of friction and in the absence of an external magnetic field	66
4.1.2	Natural modes in the absence of friction and in the presence of an external magnetic field	70
4.1.3	Natural modes in the presence of friction and in the absence of an external magnetic field	72
4.1.4	Natural modes in the presence of friction and in the presence of an external magnetic field	74
4.2	Forced oscillations	77
4.2.1	Forced oscillations in a single chain structure	77
4.2.2	Forced oscillations in the presence of an external magnetic field	83
4.2.3	Forced oscillations in a multi-chain structure	84
4.3	Comparison with experiment	84
4.4	Conclusions	87
5	Melting	89
5.1	General discussion and results	90
5.2	Melting of the single-chain	96
5.3	Comparison with experiment	101
5.4	Conclusions	102

6	Driven systems with a constriction	105
6.1	Model and methods	107
6.2	Ground state configurations	109
6.3	Dynamical properties	112
6.3.1	Pinning	113
6.3.2	Depinning	116
6.3.3	Conductivity	125
6.4	Other Dynamical properties	128
6.5	Comparison with other driven systems	130
6.6	Conclusions	132
7	Summary	135
8	Samenvatting	139
Appendix A Chapter 3		145
A.1	Energy per particle in multi-chain configurations	145
Appendix B Chapter 4		149
B.1	Equations of motion in the harmonic approximation	149
B.2	Eigenfrequencies in multi-chain configurations	151
B.3	Amplitude of displacements	153
References		155

1

Introduction

An appreciable amount of theoretical and experimental research has already been devoted to classical Wigner crystals. Most of the efforts have concentrated on the properties either of finite or infinite three and two dimensional (2D) Wigner crystals. The aim of this work is to study in detail how the structural, dynamical and melting properties of an infinite 2D classical Wigner lattice change by further lowering the dimensionality with the application of an external confining potential. This potential reduces the in-plane motion to one direction of the plane and introduces anisotropy in the system, which results finite in the direction of the external confinement and infinite in the other one. The different characteristics of the system with respect to the two directions, as well as the different features between a strictly one dimensional (1D) and a quasi-1D system, are discussed. The case of finite systems is also investigated in order to make comparisons with real experimental systems. The influence of inter-particle interaction, confining potential, the effect of temperature, the effect of an external driving forces and the presence of constrictions are critically examined. Hereby, we aimed at revealing the basic physics of such a system. Most of the work in this thesis is motivated by experimental results on colloidal systems, complex plasmas and electrons on liquid helium.

In the first chapter, we give a few typical examples of experimental systems which exhibit Wigner crystallization and which can be confined in one direction. The second chapter is devoted to the description of the model system and the

numerical methods which are used to obtain its relevant properties. The Monte Carlo and Molecular Dynamics simulation technique are briefly introduced. In the third chapter we show that depending on density and inter-particle interaction the system crystallizes in a chain-like structure. The ground-state configuration and the structural transitions, which are first (mainly) or second order, are illustrated. The normal modes are treated in the fourth chapter. The dispersion relations are calculated and compared with the experimental results about the phonon spectrum of a quasi-one-dimensional plasma crystal. The normal modes of a chain-like system consist of longitudinal (acoustical) modes and transversal (optical) modes. The number of acoustical branches is equal to the number of optical branches and is equal to the number of chains in the system. In the presence of friction, the free oscillations of the system are exponentially damped in time. We also study the effect of a constant magnetic field on the dispersion relations. The case of forced oscillations induced by an external driving force is discussed. In the fifth chapter, we present the melting properties of our chain-like model. There is evidence that melting is direction dependent and starts first in the unconfined direction. Furthermore, the melting temperature shows a reentrant behavior as a function of the density of the system and a regime of frustration around each point of structural transition can be identified. In the case of the single chain structure, melting shows different features with respect to the multi-chain configurations. Finally, we study the static and dynamical properties in the presence of a local constriction when a constant external driving force is applied in the unconfined direction. The constriction barrier and the friction pin3 the particles up to a critical value of the driving force. For large enough driving force the system can depin in different ways depending on the strength of the constriction potential. The dc conductivity is zero in the pinned regime, it has non-Ohmic characteristics after the activation of the motion and then it is constant. We show that the dependence of the conductivity with temperature is not trivial and that for large drives, even in the case of high constriction barrier, the particles can flow orderly in a well defined channel structure, i.e. the system exhibits the phenomenon of dynamical reordering.

1.1 WIGNER CRYSTALLIZATION

The unusual properties of many-electron systems have lead to a number of spectacular discoveries in condensed matter physics during the last century, including superconductivity and the fractional quantum Hall effect. Both these phenomena are essentially quantum in nature and occur when the de Broglie wavelength of an individual electron is comparable to the inter-electron separation, with electron-electron interactions playing a key role in defining the state of the system. But at the opposite extreme, i.e. at the low-density limit, one

would expect the electron system to behave like a classical fluid. At low temperatures, such a fluid would solidify into what is known as a *Wigner crystal*, as first predicted by Eugene Wigner in his pioneering work in 1934 [1]. The electrons in a Wigner solid form a periodic spatial arrangement which minimizes the mutual Coulomb repulsions and the energy. Lowering the temperature the Coulomb energy increases relative to the kinetic energy and correlations begin to strongly dominate the electronic structure. For a homogeneous 3D electron gas, such crystallization is expected at very low densities.

Although the original Wigner crystallization was related to electrons, nowadays physicists call Wigner crystals many different systems of strongly interacting charged particles. They are normally in the gas or liquid state and under specific conditions of temperature and density undergo a phase transition towards an ordered state, i.e. a periodic crystalline array. Thereby, Wigner crystals can be found both in quantum and in classical systems. Some significant examples of Wigner crystals will be illustrated in the next sections.

A classical system of charged particles will form a crystal if the mean kinetic energy of the particles is sufficiently low compared to the average potential interaction energy. The classical ground state is always a crystal (because the kinetic energy depends only on the temperature). This crystal melts when the temperature T is increased, due to the thermal excitations of the particles. In the quantum regime the situation is different. A quantum system of interacting particles will form a crystal when the average potential energy overwhelm the average kinetic energy, as well. But in a quantum crystal there is a finite zero-point energy: as the density increases the particles are more localized, thus their momenta are larger according to the uncertainty principle, which results in a greater zero-point energy. This means that it is possible to melt the crystal by increasing the density at $T = 0$. This explains why low temperatures and low densities are required to form a quantum crystal.

The importance of the inter-particle interaction (Coulomb or other kind of repulsive interactions) is determined by the coupling parameter $\langle V \rangle / \langle K \rangle$, which is defined as the ratio of the mean potential energy to the mean kinetic energy. It is customary to refer to this coupling parameters as Γ in the classical regime and as r_s in the quantum regime. It is possible to estimate $\langle V \rangle$ as $\langle q^2 / \varepsilon a \rangle$, where q is the charge, ε the dielectric constant and a the average inter-particle distance. From the particle density n , $a = 1 / \sqrt{(\pi n)}$ in a two-dimensional (2D) system. Considering that in the classical regime the average kinetic energy is $k_B T$, with k_B the Boltzmann constant, the classical coupling parameter is:

$$\Gamma = \frac{q^2 \sqrt{(\pi n)}}{\varepsilon k_B T};$$

on the other hand, considering that electrons fill the available energy states up to the Fermi energy $E_F = \hbar^2 \pi n / m^*$, with m^* the electron effective mass, the quantum coupling parameter is:

$$r_s = \frac{m^* q^2}{\varepsilon E_F} = \frac{m^* q^2}{\varepsilon \hbar^2 \sqrt{(\pi n)}}.$$

According to the values of the coupling parameters different regimes can be distinguished. For the classical Wigner crystals when $\Gamma < 1$, which is realized in a dilute system at high temperature, the electrostatic interaction is of minor importance and the system behaves like an ideal gas. For $1 < \Gamma < 100$ the particles are correlated and the system behaves liquid-like. For $\Gamma > 100$, which is the high-density and low-temperature regime, the potential energy dominates over the kinetic energy and there are strong correlations between the particles, which is expected to drive the system through a phase transition to a periodic crystalline array. Actually, from numerical simulations [2–4] and experiments [5] the Wigner crystallization in a 2D system is expected to occur for $\Gamma \approx 130$. In the pure quantum case, for $r_s \ll 1$ the electrons behave as an ideal gas of fermions and for $r_s \gg 1$ they form either a degenerate Fermi liquid or a Wigner solid. By numerical simulations the electrons should undergo a phase transition to the Wigner solid for $r_s \approx 37$ [6].

Although the Wigner crystallization is quite easy to be realized in classical systems, like colloids or complex plasmas, until now electron solids have only been observed in two experimental systems: electrons above the surface of liquid helium and electrons at the interface of semiconductor heterostructures, typically GaAs and $\text{Ga}_{1-x}\text{Al}_x\text{As}$ [7]. The quest for the observation of such a Wigner crystal has been the object of very intense and continuous work. Experimental observations of a 3D Wigner lattice of electrons has not yet been realized. Electrons in ordinary materials, like metals and semiconductors, are affected by the ‘imperfect’ host lattice in which they move. Defects, impurities and similar imperfections destroy such a 3D Wigner lattice. Therefore, it is necessary to search for alternative systems where such Wigner crystallization can be realized.

In 1971, almost forty year after the original Wigner’s work, Crandall and Williams [8] proposed to look for such a Wigner lattice in the 2D system of electrons above a liquid helium surface. Here the conditions for crystallization can be achieved much more easily because of the almost ideal features of the system, e.g. the absence of complicated band structure, the extreme cleanliness, i.e. the absence of impurities and imperfections, and the inherent low temperature. After the theoretical prediction of the possibility of the existence of a Wigner lattice on liquid helium, it took eight years until Wigner crystallization was first observed experimentally and reported in 1979 by Grimes and Adams [9]. The electron solid is lighter, much less dense and is also much less strongly bound than a normal solid, so that different experimental techniques had to be developed in order to detect whether or not the 2D electron system was in the ordered phase.

Since then experimental investigations have made considerable progress and new systems have shown Wigner solid features. Modern processing techniques allowed the artificial creation of such Wigner lattices in the laboratory. Electrons in quantum dots [10], particles in confined plasma [11–14] and in colloidal suspensions [15, 16] can exhibit crystallization. Various similar systems, such as laser-cooled ions in a electric or magnetic traps [5], ions in a radio-frequency trap [17, 18] or in a Penning trap [19–21] show very ordered structures under certain conditions of temperature and density, as well.

Other related systems, which exhibit crystal-like ordering are the following: the vortex clusters in an isotropic superfluid [22], vortices in superfluid He^4 [23, 24], vortices in a Bose-Einstein condensate stirred with a laser beam [25], vortices in type II superconductors [26] and in superconducting grains [27]. Even biological systems [28, 29] can have many common features with those of 2D charged particles in the solid phase.

Electrons and ion crystals are atomic scale crystals, while complex plasmas and colloidal systems are macroscopic crystals, with particle size ranging from μm to fraction of mm . There are several advantages in the use of macroscopic crystals for studying the general properties of Wigner crystals: they are relatively easy to control and, above all, direct imaging and direct measurements are possible. It should be stressed that ordered phases can be realized even in millimeter sized systems; indeed, very recently 2D Wigner islands, consisting of charged metallic balls above a plane conductor were realized and studied experimentally [30].

In this thesis we are mainly interested in the properties of 2D systems of strongly interacting particles, which exhibit Wigner crystallization and which have a linear dimension that is much larger than the other one, the so called *quasi-one-dimensional* (Q1D) systems. There are several way to obtain a Q1D system and all these rely basically on the possibility of a relatively strong confinement in one specific direction of the plane (in the other direction the confinement can be very weak), which in the extreme case is of hard wall type.

In the following sections, some experimental Q1D Wigner crystal systems will be discussed.

1.2 QUASI-ONE-DIMENSIONAL EXPERIMENTAL SYSTEMS

1.2.1 Electrons above liquid helium

Electrons deposited above the surface of liquid helium will float about 100 \AA above the He surface and form 2D ordered systems, which undergo the solid phase transition at sufficient low temperature, i.e. form a Wigner crystal, if a proper external electric or magnetic field is applied in the direction perpendicular to the helium surface [9, 31]. The electrons can be trapped in surface

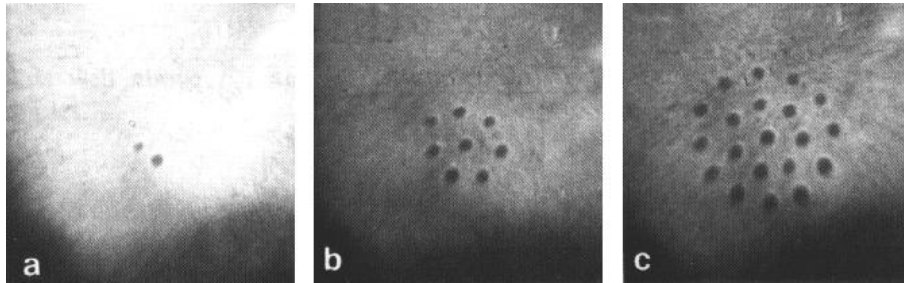


FIG. 1.1: Configuration of (a) 2, (b) 8 and (c) 20 dimples (appearing as dark spots) on a liquid helium surface in an external potential of cylindrical symmetry. From Ref. [31].

states in which they are attracted towards the surface by a weak positive image charge they induce in the liquid and are held by a perpendicular electric field E . They are prevented from penetrating into the liquid because of the high energy barrier at the surface. The electron energy is continuous in the plane of the helium surface and quantized in the perpendicular direction with hydrogen-like energy levels. Below 2 K , electrons are in the lowest energy level for vertical motion, floating above the surface. Wigner crystallization of electrons was observed for the first time in this system in 1979 [9].

By applying a strong electric field perpendicular to the helium surface and lowering down the temperature, the system becomes unstable and the homogeneous electron distribution is destroyed. The electrons become localized in a regular array of pockets, or 'dimples', which can be considered as effective classical charged particles. These many-electron dimples, each of which contains up to 10^7 electrons with a typical diameter of the order of 1 mm [31], can be considered as macroscopic particles and the Coulomb repulsion between them leads to an ordering in a ring configuration as is shown in Fig. 1.1 for 2, 8 and 20 dimples on the surface of liquid helium [31].

It is not only possible to trap electrons above the surface of liquid helium, but also to trap charged particles, or 'ions', below the surface of liquid helium [32]. As is the case with electron pools trapped above the surface of liquid helium, the trapped ions provide us with simple 2D systems of particles with precisely known (Coulomb) interactions. There are two essential differences with the systems of electrons above the He surface: 1) the effective mass is much larger; and 2) the particle motion is strongly damped because of the friction with the liquid. Such systems are model systems which allow one to carry out experiments on the behavior of condensed matter in two dimensions. Because of their large effective mass, the ion system can be treated classically.

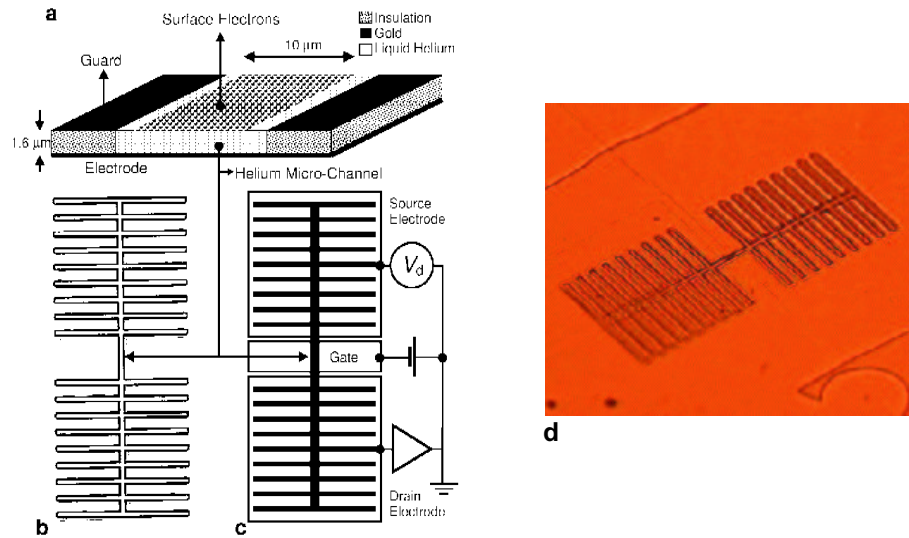


FIG. 1.2: The new microelectronic devices. (a) Schematic of an electronic microchannel; (b) schematic of the device; (c) circuit diagram and (d) a real image of the device. From Ref. [33].

A recent experiment in London by Prof. M. Lea's group has realized for the first time a Q1D Wigner crystal made with electrons above liquid helium. The team fabricated a novel microelectronic devices by using semiconductor etching to scratch micrometer-scale channels on a *GaAs* wafer. They filled each channel with superfluid helium and sprinkled it with free electrons from a filament. A series of electrodes above and below the wafer confined the electrons to the microchannel, where they slid around above the helium surface and formed long, narrow Wigner crystals. The experimental setup is shown in Fig. 1.2.

It was found that the resistance above 1 *K* is Ohmic. The electrons form a classical conductor (i.e., not Fermi degenerate), as originally proposed by Drude, but in two dimensions. A striking change occurs below 1 *K*, as the effective resistance unexpectedly rises and becomes strongly non-Ohmic, increasing with the applied voltage. It reaches a maximum close to the theoretical melting temperature of the Wigner crystal. This nonlinearity was interpreted as the signature of the transition from an isotropic electron fluid at high temperatures to a spatially ordered phase.

Electrons on liquid helium are interesting not only for fundamental research but could also have applications in quantum computing, where organized arrays of electrons might someday be used to store and process information. Each electron could hold a quantum bit, or 'qubit' of information, and the entire

crystal could be used for storing data or performing operations in a future quantum computer, as proposed in the work of Dykman and Platzman [34].

1.2.2 Colloidal systems

The field of colloids has a long history and embraces many diverse scientific disciplines. Colloidal particles are important in a broad range of applications in technology and material processing.

Colloids are small particles dispersed in a fluid: they can be gaseous, liquid, or solid. Here we are interested in solid colloidal particles. Such particles are made from many different materials and can be suspended in a wide variety of solvents. The typical size of colloidal particles ranges from nanometers to micrometers. The formal study of colloids began in the latter part of the 19th century with the work of T. Graham [35]. The first colloids studied were gelatins and glues, and so Graham used the Greek word 'kolla', meaning glue, as the root for his newly coined term. The field of colloids is attracting a growing interest and new experimental techniques are allowing improved measurement and better understanding of the structure, properties, and behavior of colloidal suspensions [36]. The rheological properties have traditionally been of primary concern in their technological applications; because colloids can be produced in a high controlled way, they are now being used as novel building blocks to engineer completely new materials, including high-precision filters, controlled-porosity substrates, and photonic devices. The great scientific interest about colloidal suspensions is also motivated by their potential use as model systems to investigate collective phase behaviors, to explore fundamental questions of packing and geometry, and to fabricate new structures. It has been found that colloidal systems display phenomena as crystallization, melting, structural phase transitions, etc. Thus colloids represent a very interesting classical model system which is conveniently accessible by experiments. An exhaustive and even a very partial introduction to the subject is far beyond the purposes of this PhD work, so huge the matter is. We will limit to some general considerations about solid colloids and, then, we will discuss some experiments for which our theoretical model is suitable.

When dissolved in a polar solvent, mesoscopically sized colloidal particles typically get charged due to the dissociation of ion groups at the particle surfaces into the solution, producing highly charged 'macroions' and micro counterions. Addition of salt ions to the solution tailors the electrostatic interaction between macroions, resulting into a screened Coulomb interaction. The solvent approximatively enters only via its dielectric constant, so the colloidal particles are modeled as charged hard spheres of diameter D with charge Z homogeneously smeared over the spherical surface interacting through an effective pair potential:

$$V(r) = \frac{Z^2 \exp(-\kappa(r-D))}{\varepsilon r (1 + \kappa D/2)^2},$$

where ε is the dielectric constant of the solvent and κ is the inverse screening length, which can be estimated from the concentration of micro counterions and salt ions as:

$$\kappa = \sqrt{\frac{4\pi}{\varepsilon k_B T} \sum_i q_i^2 \rho_i},$$

where the sum runs over the micro and salt ions species of charge q_i and density ρ_i .

The major properties of solutions of mesoscopically sized colloids lie in the facts that: (i) the solvent allows for quick thermalization and equilibration and (ii) the interactions of the macro-particles can be tuned and tailored by using different preparation schemes in solution and, eventually, applying opportune electromagnetic fields. It is remarkable that in some cases counterion correlations produce the spectacular phenomenon of 'charge inversion', where the macroions can exhibit short-range attractions [37]. This feature is of fundamental importance in some biomolecules (see Sec. 1.3.3).

Of course, the screened Coulomb interaction is not the only possible one between colloids, indeed, the so called super-paramagnetic colloidal particles interact as magnetic dipoles when a strong magnetic field is present [31, 38].

Because of their small size and of the interactions with the solvent, thermal energy induces Brownian motion of the colloids, and the resultant dynamics can play an important role in the properties of the suspension. In order to get ordered structure is, therefore, necessary to reduce the thermal agitation. Lowering the temperature would lead to the solidification of the solvent, so other techniques must be employed. The correct strategy is to act only on the colloidal particles, leaving the solvent unaltered. This can be realized introducing into the system an inhomogeneous electromagnetic field. When a 1D or 2D periodic substrate, normally consisting of interference fringes coming from the superposition of different fields, is added to the system unique ordering transitions appear, i.e. the colloidal particles can form a Wigner crystal.

The organization and manipulation of colloidal matter at the microscopic level are nowadays routinely achieved by using laser light, which confines the particles. Interfering laser beams can induce local 'freezing' providing in this way the possibility of formation of crystalline structures. A large amount of theoretical and numerical studies were dedicated to this substrate-induced freezing effect [39].

The gradient of the optical field can induce colloidal spheres, whose refractive index is higher than their surrounding medium, to be trapped in the light field maxima [40]. These kind of systems are usually called 'optical tweezers'. While optical tweezers typically confine few colloidal particles, larger traps, like the

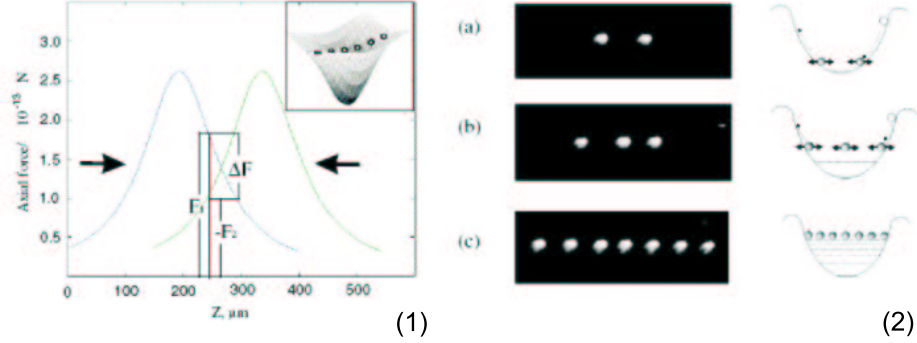


FIG. 1.3: (1) Axial forces for the counterpropagating beam geometry. The peak point for each curve corresponds to the beam waist position. Forces from both beams (F_1 and F_2) are drawn as positive. The resultant axial force F is the difference of two forces drawn. The inset shows how particles reside in the resulting potential well; (2) experimental data for arrays of (a) two, (b) three, and (c) seven spheres (each $3 \mu\text{m}$ in size). The diagrams on the right elucidate how we fill up the approximately harmonic potential well created by the two counterpropagating beams. From Ref. [42]

so-called 'dielectric bottle', have been used to confine a large number of particles [41].

A recent experiment by S.A. Tatarkova [42] successfully created a Q1D chain of microscopic colloidal particles. In this experiment a continuous wave Ti-sapphire laser provides the trapping laser light. The beam was expanded and split into two equal counterpropagating components which were then focused into a rectangular glass cell filled with uniform monodispersed colloidal microspheres in water of diameters 2.3 and $3 \mu\text{m}$. The particles were directly observed by a microscope objective. The two counterpropagating laser beams create a potential well, where colloids can be trapped. For collinear beams a near parabolic optical confining potential results, as shown in Fig. 1.3. This experiment provided the possibility to investigate the properties of chain-like systems, in particular the low energy configurations, the stability and the normal modes. We will compare these experimental findings with our theoretical results in the next chapters.

Another interesting experiment in which the colloids form a chain-like crystal is the one of Ref. [43]. Here, a periodic potential was superimposed to a quasi Q1D colloidal system by interference of two linearly polarized beams of a $Nd:YVO_4$ laser. Owing to optical gradient forces, this interference pattern acts as an external potential on the particles with the potential amplitude V_0

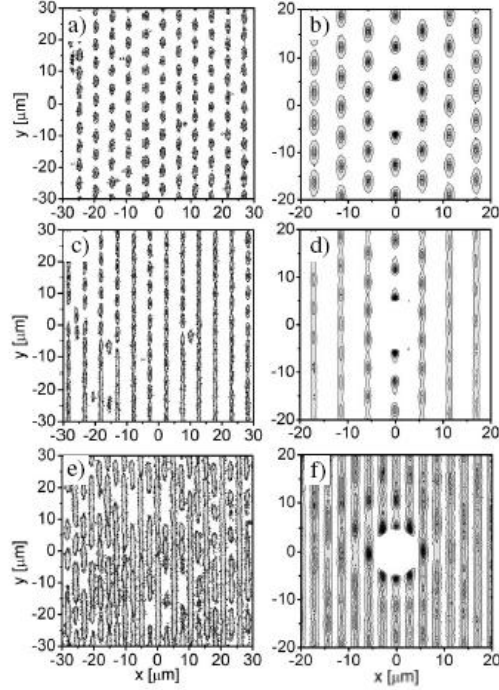


FIG. 1.4: Particle trajectories and pair correlation function: (a,b) for the solid phase, (c,d) for the modulated liquid phase and (e,f) for the liquid phase. From Ref. [43].

scaling linearly with the laser power. With increasing substrate strength V_0 the particles become more and more localized along the interference fringes due to the forces of the light. Because of the repulsive particle interaction, the system responds at sufficiently high V_0 by first forming a modulated liquid [44] and then a crystalline phase, as shown in Fig. 1.4.

Another successful way to create 2D or Q1D arrays with magnetic colloids is depicted in Fig. 1.5: on a substrate of fused silica narrow strips ($\sim 3nm$) of a magnetic material, usually Ni , are deposited. By spin coating the strips are covered by a PMMA (polymeththylacrylate): this film is necessary to prevent the particles from sticking to the surface. A strong external magnetic field in the direction perpendicular to the plane magnetize the colloidal particles, which thus interact each other through a magnetic dipole potential and with the strips, resulting in this way in a chain-like structure.

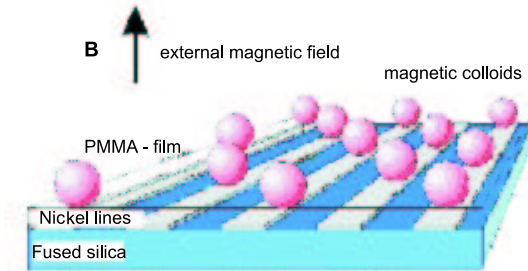


FIG. 1.5: Chain-like structures realized with magnetic colloids.

In microfluidic devices, where narrow channels are scratched on a solid substrate, the colloids are confined by hard walls in one dimension, forming in that way a Q1D system. Numerical simulations and experiments [45, 46] have pointed out the possibility of stable chain structures in the proximity of the walls, if the particles exhibit a strong inter-particle interaction. The walls help to stabilize the solid phase and the properties of the system became liquid-like as the center of the channel is approached.

Finally, colloids driven over a periodic substrate provide a useful model system for studying pinning and depinning phenomena as well as models for friction. A large amount of theoretical and experimental investigations have been dedicated to the melting, i.e. the solid to liquid phase transition, for these kinds of systems. One striking feature is the possibility of 'reentrant melting' when the substrate strength is large enough that the colloids behave quasi-one-dimensionally and that the fluctuations are effectively enhanced. We will return on these points in Chapter 5.

1.2.3 Complex plasmas

Plasma state, an ionized gas consisting of electrons and ions, is usually referred as the fourth state of matter. Besides solid (crystalline), liquid and gaseous, it is also the most disordered state. More than 99% of the visible matter in our universe is in the plasma state. When colloid nano/microscopic particles ('dust') are immersed in a plasma background, they can form ordered structures, i.e. they crystallize in a Wigner lattice, under proper conditions. The formation of Wigner crystals in complex (dusty) plasmas has attracted much interest very recently and it is now a subject of intense research in the context of physics and chemistry of plasmas, ionized gases, space physics and astrophysics, and materials science. Earlier this system was also called a *dusty*

plasma because the particles were treated as 'dust'. Nowadays one refers to it as a *complex plasma* in analogy to the condensed matter field of complex fluids in colloids. This state of matter is ubiquitous in space, e.g. in the interplanetary medium, in interstellar clouds, in comet tails and in the ring systems of the giant planets as well as in mesospheric noctilucent clouds, protoplanetary accretion disks, nova ejecta and planetary magnetospheres, where the plasma coexists with dust grains. In microelectronics manufacturing, avoiding particle contamination during the many production steps, that involve plasmas, is a technological challenge [47]. On the other hand, the growth, transport, and deposition of nanoparticles is the central goal of many plasma deposition techniques, for example in the manufacturing of amorphous solar cells [48]. Thus it is not surprising that physicists, chemists, astronomers and industrial researchers have investigated and are intensively studying many aspects related to complex plasma systems.

A complex plasma is a four component systems, i.e. electrons, ions, neutral atoms and dust particles with high charges which are responsible for unusual properties. Unlike the most ordinary plasmas in space and laboratory which are weakly coupled, i.e. the thermal energy dominates over the interaction energy, a complex plasma is strongly coupled because every dust particle can carry around 10^4 electron charges. The interaction may lead to a strong coupling of the dust particles, resembling a fluid phase, and even to the crystallization of the particles in a so-called *plasma crystal*. In the ordered phase the interparticle spacing is very large compared to the size of the particles, so the plasma solid has a very low density. This system represents a unique bridge connecting plasma physics and (soft) condensed matter physics.

The ordered solid phase of dusty plasmas was first predicted theoretically by H. Ikezi in 1986 [49] and then observed experimentally as plasma crystals in 1994 [12–14]. A few typical topics which were studied are the following: (i) the different structures in the crystal phase, especially under an additional dipole field [12–14]; (ii) the normal modes and wave propagation under external periodic driving forces [50, 51]; (iii) the structure and the order-disorder phase transition [14, 53], which may serve as a macroscopic model system for melting in two or three dimensions; (iv) the features of the liquid phase [54]; (v) the defect properties and dynamics [55]; (vi) the microscopic motion and collective excitations in the melting and liquid states [56]; (vii) the anomalous diffusion in the melting and liquid states [56], etc.

In what follows, we will provide a short overview of the physics behind the formation of a plasma crystal and we will describe some new experiments in which a 1D or Q1D plasma crystal have been realized and their properties have been studied.

In a complex plasma colloidal particles, ions, electrons and neutral atoms coexist. Due to the much lower mobility of the heavier ions, the particles are hit on average by more electrons. They accumulate on the dust particle that becomes negatively charged of several electron charges ($10^3 \div 10^4$). This

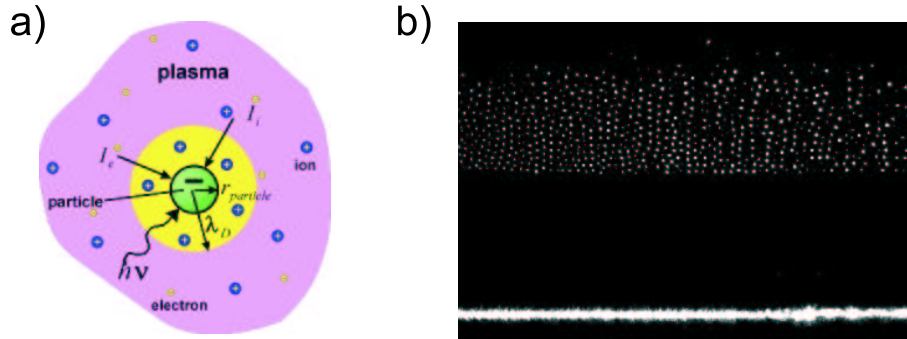


FIG. 1.6: The interactions of a dust particle in a complex plasma (a) and (b) the sideview of a plasma crystal in laboratory experiments: dust particles are suspended in a (argon) plasma above a high-frequency electrode (bottom).

negative charge is, at a certain distance, screened by a positive cloud of ions around the particle (see Fig. 1.6(a)). Hence, in a plasma crystal the interaction between charged dust particles is a Coulomb repulsion, which is screened by the polarization of the surrounding plasma particles, mostly the gas ions which represent the major species. Konopka *et al.* [57] first demonstrated that the inter-particle interaction is accurately modeled by a Yukawa potential, as in the case of a colloidal system. The knowledge of the charge q on the particles and the screening length λ_D is of central interest. Their theoretical determination is extremely difficult, nonetheless they can be measured in the experiments, so they are assumed as empirical parameters in the theoretical models.

In the experimental realizations, particles are trapped in a horizontal layer by a shallow parabolic well, due to two electrodes, and can be suspended in a sheath above the lower electrode, where the gravity force is balanced by the electrostatic force (see Fig. 1.6(b)). They form, thus, a quasi-two-dimensional system. In order to get three-dimensional structures one has to eliminate or reduce gravity effects. This is nowadays achieved in microgravity experiments, like parabolic flights. When the electrostatic energy of neighboring particles exceeds the thermal energy, the particles arrange themselves in regular solid-like structures, i.e. Wigner crystals. The large charges drastically increase the coupling parameter Γ and the suspended dust clouds can undergo a phase transition to an ordered crystal state even at room temperature. Unlike the atomic-scale systems, there is no need of very low temperature or laser cooling to reach ordered phases. Furthermore, the larger mass slows down the time scale to the order of a second, and the inherent spatial scales make direct observations of particle motion feasible: particle trajectories can be observed by optical micro-imaging and the structural and dynamical behavior can be

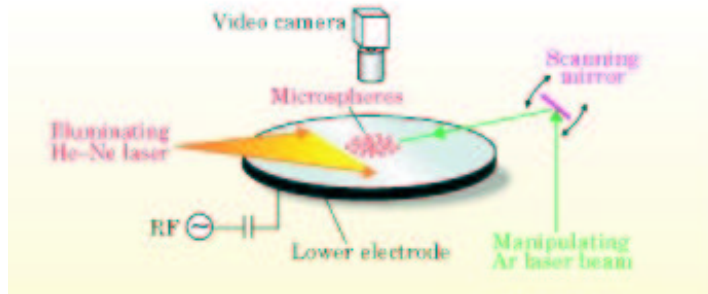


FIG. 1.7: Typical experimental set-up in a complex plasma experiment. From Ref. [14].

measured in real time and space [11]. In addition, dynamical processes are only weakly damped because of the low density of the plasma environment, whereas in colloidal systems the motion of particles is generally overdamped because of the presence of a dense solvent. By the use of a laser beam, it is possible to investigate the response of the plasma crystal to an external driving force. Interestingly, by focusing the laser light on a single particle, it is even possible to excite its motion and investigate how it affects the whole system [51]. The experimental setup of a general plasma experiment is illustrated in Fig. (1.7).

An extensive literature exists about the subject of plasma crystals, which has been growing exponentially in the last ten years. A detailed description of the structure, dynamics and melting of a finite size 2D complex plasma is given in Ref. [58], while the features of a finite 1D chain are described in Ref. [51]; the ground state configuration and the spectral properties in the case of harmonic or hard-wall confinement are studied in Ref. [59, 60]; the wave propagation and the oscillation modes are discussed in Ref. [61, 62]; the melting and defect induced phenomena are analyzed in Ref. [63]; the response to external perturbations or driving forces are illustrated in Ref. [51, 64, 65], just to cite a few.

The possibility to obtain a Q1D arrangement in a plasma crystal is obviously related to the realization of a Q1D confining potential. This is achieved essentially in two ways in the experiments: (i) by putting a narrow rectangular barrier on the lower electrode, which allow the particles to move mostly in one direction [66], (ii) by shaping the lower electrode with a groove depression along one direction on which particles preferably settle [51, 67]. We will give some details about the experiments of Ref. [51, 67], which are well described by the theoretical models discussed in Chapters 3 and 4.

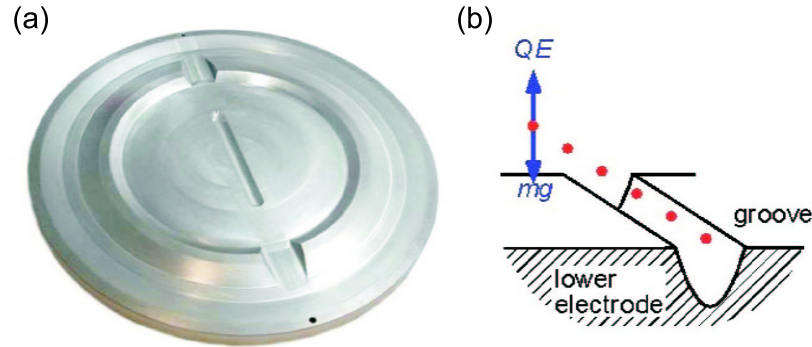


FIG. 1.8: The lower groove-shaped electrode (a) and the formation of the 1D chain in the groove (b). From Ref. [51].

In these experiments, the equilibrium configurations of a linear chain formed by a small number of particles was determined and the normal modes studied. The plasma was produced in a capacitively coupled radio-frequency discharge with Xenon gas at low pressure. A sheath formed immediately above the lower electrode. Then the particles were introduced. Particles were externally confined by electric fields in the sheath above the lower electrode. The sheath conforms to the shape of the electrode, which has a groove-shaped depression excavated in one direction, as illustrated in Fig. 1.8(a). This produced in turn a one dimensional chain-like arrangement of the particles. The groove had a parabolic shape with a length of 80 mm and a depth of 2 mm (see Fig. 1.8(b)). The confinement in the vertical direction was strong enough to prevent any vertical buckling of the chain. The particles were illuminated with a He-Ne laser and viewed with a video camera, which allowed the measurement of particle positions and velocities in real time.

It was found that inserting 10 up to 28 particles the equilibrium configuration is a 1D chain. When this number is increased, the structure undergoes a structural transition with the bifurcation of the chain, producing, therefore, a Q1D system. In Fig. 1.9 some 1D and Q1D configurations of the system are shown. The inter-particle spacing was not uniform: it was 15% smaller in the center than at the chain end, because of intrinsic edge effects. Further increasing the number of particle, one expects that a larger number of chains will be formed. This was not possible in the experiment because it was not possible to stabilize more than two chains in the groove. To overcome these difficulties and to get a multi-chain system, the same authors have proposed to dig more than one groove in the lower electrode.

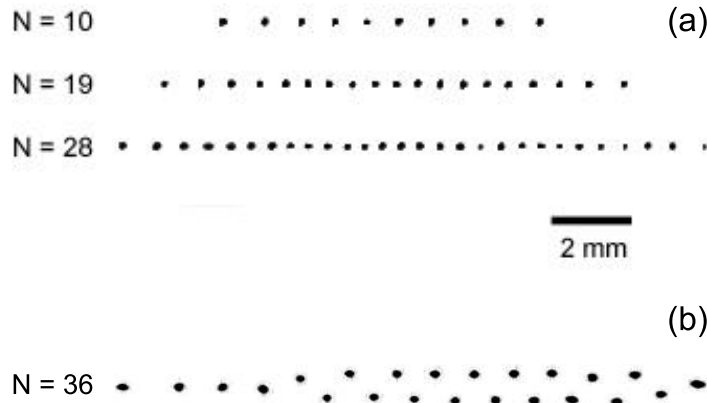


FIG. 1.9: Single chain configurations for different number of particles (a) and bifurcation of the chain (b). From Ref. [65].

With this experimental apparatus the natural normal modes of the system and their dispersion relations were studied using the method of current autocorrelation function [68]. Furthermore, by manipulating a particle near the chain center with two counterpropagating laser beams, forced oscillatory motions were excited. Laser light exerts a radiation pressure with a magnitude proportional to the laser intensity. The intensity of one laser beam was modulated by a scanning mirror that periodically blocked a portion of the beam, yielding a sinusoidal intensity, while the opposite laser was continuous, so that the net force applied to a particle was sinusoidal. Studying how the waves propagated away from the local excitation location, it was possible to measure the dispersion relations for the forced oscillations. An externally confined chain can vibrate with two modes. In the longitudinal mode, particle motions are compressional along the chain. In the other mode, particles move transverse to the chain, and their displacements are restored by the external confining potential; this is different from the transverse mode in a 2D lattice, where the in-plane restoring force is provided by inter-particle interactions. In Chapter 4 the normal modes and the forced oscillations of a chain-like system are studied. Our theoretical findings will be compared with the results of these experiments.

1.2.4 Other systems

Colloidal and plasma crystals are essentially classical objects, because of the microscopic size and large mass of their constituents. Q1D ordered phases can

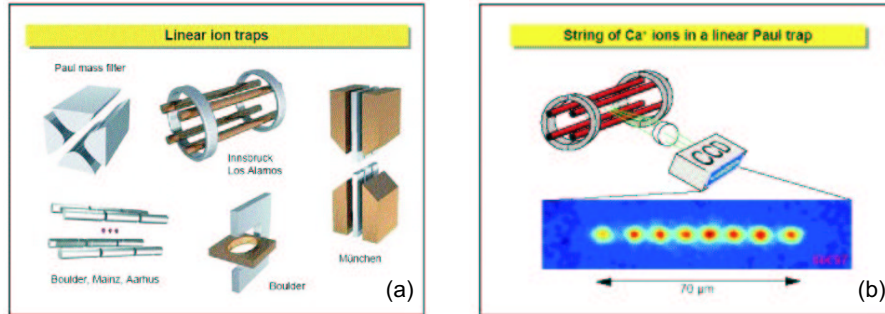


FIG. 1.10: (a) Different realization of a linear ion trap; (b) a chain of Ca^+ ions trapped in a Paul trap. From Ref. [70].

be realized also with ions and certain kinds of molecules, providing them with an appropriate confinement. For the ions this is achieved by electromagnetic confinement and laser cooling, while Ar and Xe molecules can be trapped by adsorption in groove positions in a bundle of carbon nanotubes.

According to Earnshaw theorem [69] static electromagnetic fields alone cannot trap a charge. However, using a combination of static and alternating electromagnetic fields it is possible to confine ions. The two traditional ways to confine ions is by using the Paul and Penning traps. Both consist of a set of electrodes that generate a quadrupolar field (see Fig. 1.10(b)). In the case of the Paul trap, the voltage on the electrodes varies sinusoidally in conjunction with a static electric potential between the end caps. The trap is stable in the axial direction and unstable in the radial plane. The ion is therefore successively attracted to the polar end caps or to the electrodes. On average, it experiences a net force that pushes it towards the center of the trap. In the exact center, the field is zero and any deviation results in a net restoring force. The Penning trap has the same electrodes, but the electric field is static: it is repulsive for the end caps. The ions are prevented from reaching the electrode by a longitudinal magnetic field.

The Paul and Penning traps can also be made into different geometries, as shown in Fig. 1.10(a). In the extended linear configuration, in the case of Paul traps, a radio frequency potential is applied to the four rods to confine the ions in the radial direction and a static potential applied to the end caps prevents them from escaping along the axis. By design, there is strong confinement perpendicular to the axis and weak confinement parallel to the axis. Charged particles, either created in the trap or introduced from the outside, will therefore preferentially locate in a small region along the axis. The size

of that region is clearly related to the ion kinetic energy, the larger the energy the wider the region. If a laser beam is used to cool the ions to very low temperatures, then liquid and crystal-like states are realized.

The crystallization of small numbers ($N < 50$) of laser-cooled ions into Coulomb clusters was first observed in Paul traps [18, 71]. Different stable crystalline phases have been observed in a Penning trap for a system of laser-cooled ${}^9\text{Be}^+$ ions [72], where the energetically favored structure could be sensitively tuned by changing the areal density of the confined ions. Plasmas of Mg^+ ions, containing more than 10^5 ions, have been found to reach well-ordered states by applying laser cooling in Ref. [73]. Those crystals were highly elongated with up to ten concentric cylindrical shells surrounding a central string.

In general, clouds of laser-cooled trapped ions can condense and exhibit quasi-crystalline spatial order in Penning [74–76] and Paul radio-frequency traps [18, 71]: they form body-centered-cubic lattices [73] if the confinement is three-dimensional, or concentric shells with near-hexagonal ordering within the shell [73] if the confinement is quasi-two-dimensional. The capability of tuning the confinement offers the unique possibility to study ordered system of different dimensionality. Then, realizing a nearly one-dimensional confinement, it is possible to observe in an ion trap Q1D crystalline structures. It is, actually, the result of the experiment of Ref. [77], where the observation of Q1D crystals of 19 laser cooled Ca^+ ions in a linear Paul is reported. In that experiment the confining potential was asymmetric in the axial and radial directions. For radial confining potentials stronger than the axial potential, the ions crystallize into linear structures with a continuous transition from the single chain structure to a zig-zag pattern and then to a helix shape with decreasing potential asymmetry. This is the analogous of the results of Chapter 3, where the single chain structure undergoes a zig-zag transition for increasing particle density. Actually, in experiment tuning the potential results into reducing the inter-particle spacing, i.e. increasing the density. The experimental zig-zag transition is illustrated in Fig. 1.11.

Finally, it should be noticed that in Paul traps the radio-frequency field drives micro-motions. The magnitude of the micro-motion increases with the ion distance from the trap central axis, and such motion can couple energy from the radio-frequency drive into the random motion of the ions through their mutual Coulomb interaction. This mechanism limit considerably attainable crystal sizes.

It is worth to point out that the experimental results are in very good agreement with theoretical and simulation predictions [78], where static potentials, often in the form of harmonic potentials, are used.

Another possible way to produce single chain systems is to exploit chemical processes. Heavy noble gases, i.e. Ar , Kr and Xe , can form one-dimensional phases when adsorbed on the outer surfaces of close-ended single-wall carbon

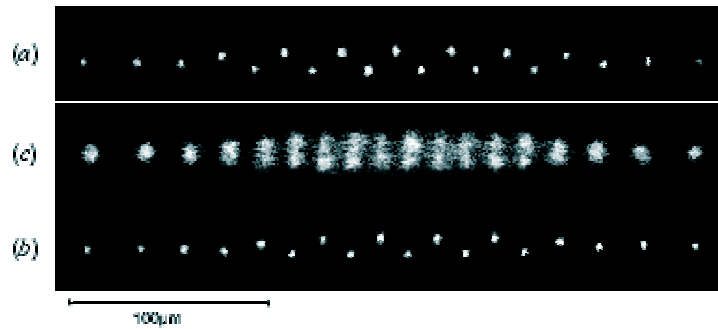


FIG. 1.11: Zig-zag shaped ion crystal consisting of 19 ions: (a) and (b) show the two different orientations observed which are nearly mirror images, (c) shows the same crystal with a longer observation time (10 s). The flipping between the two orientations results in a washed out pattern. From Ref. [77].

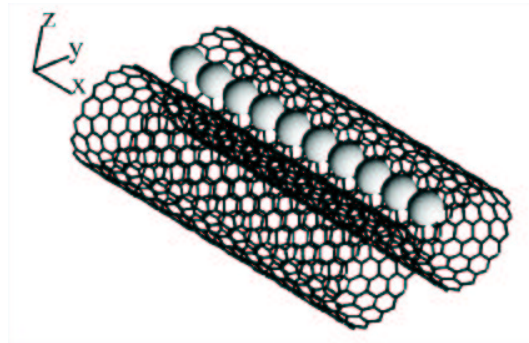


FIG. 1.12: Two carbon nanotubes with a commensurate Xe chain in between them. From Ref. [80].

nanotube bundles (see Fig. 1.12). The existence of such phases has been predicted theoretically and in computer simulations and, subsequently, confirmed in experiments [79].

Three different groups of adsorption sites are possible in bundles of close-ended nanotubes: (i) the external surface of individual tubes on the outer surface of the bundle, (ii) the grooves formed by the space between two adjacent tubes on the outer surface of the bundle, and (iii) the interstitial channels at the interior of a bundle, where three tubes come together. Of particular interest is the case that, for rigid bundles of close-ended tubes, adsorption on the grooves

results in the formation of a quasi-1D chain of atoms [79]. The chain vibrational modes have been studied theoretically in Ref. [80, 81], assuming that the interaction between adsorbate and single wall nanotube can be written as a Lennard-Jones potential, but until now no experiments have been performed to prove the theoretical predictions.

The interest in ion chains and, more in general in chain-like systems, is not only related to fundamental research, but also it could be exploited for atomic clocks and, above all, for quantum computation [82]. Indeed, trapped ions in chains arrangements 'communicate' via their Coulomb interaction. A laser excitation on an single ion can be used for the manipulation of internal (electronic) states and/or for the manipulation of the overall vibrational quantum state of the chain. Each ion in the chain represents a fundamental unit of information, i.e. a quantum bit. The trapped strings then represent a quantum register. Quantum information can be written into and can be read out of the individual ions.

1.3 RELATED SYSTEMS

1.3.1 Charge density waves

When metals are cooled, they often undergo a phase transition to a state exhibiting a new kind of order: this is the case of the ferromagnetic transition, for e.g. iron and nickel, and the superconducting transition, for e.g. lead and aluminium. Since the mid-1970s, a wide range of quasi-one-dimensional metals have been discovered that undergo a different phase transition both above and below room temperature. They become 'charge-density-wave' (CDW) conductors. These materials show strikingly non linear and anisotropic electric properties, unusual elastic properties and rich dynamical behavior. Besides the industrial potential (switches, capacitors, detectors, etc.), the ideas that explain these phenomena, span much of contemporary condensed matter physics. For these and other reasons, CDW conductors rank among the most remarkable electrically conducting materials ever discovered.

A CDW is a modulation of the conduction electron density in a metal associated with a modulation of the lattice atom positions, as shown in Fig. 1.13. The electrons are not localized as in the case of a Wigner crystal. The CDWs are a pure quantum phenomenon, that can merge at the macroscopic level. Here, we discuss briefly the subject of CDWs for two essential reasons: (i) the system has Q1D features and, above all, (ii) it is a model system in the study of pinning and depinning phenomena (which are discussed in Chapter 6) when an external driving field is present.

Almost 40 years ago R. Peierls and H. Fröhlich independently suggested that CDWs are caused by an instability of the Fermi surface involving electron-phonon interaction and that they result in an energy gap at the Fermi surface.

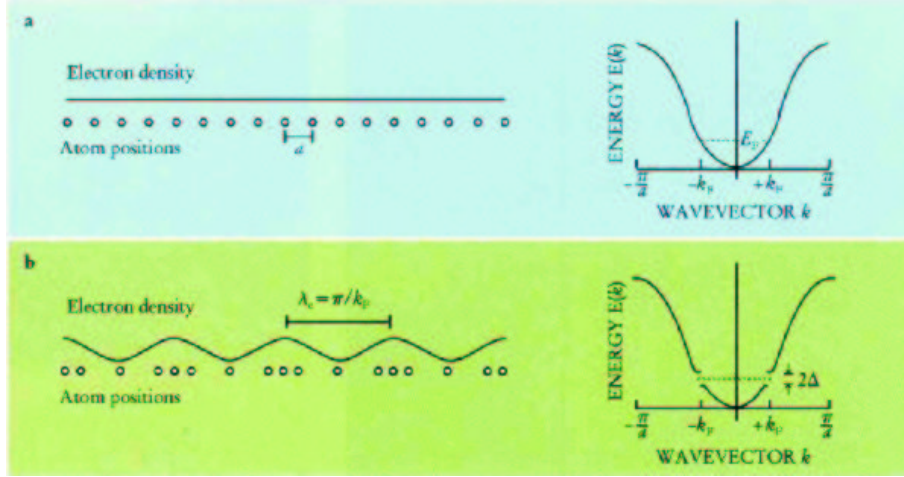


FIG. 1.13: The single particle energy band in the case when the electron and the phonon systems are not coupled (a). In that case the ions are equally spaced and the charge density is uniform. When the electron and phonon systems are allowed to interact, the competition between the elastic and electronic energies leads to a static lattice deformation and periodically modulated charge density and a gap appears in the conduction band (b). This ideal situation refers to the zero temperature case. In real Q1D systems, the transition takes place at a finite temperature T_P called the Peierls temperature. From Ref. [83].

Peierls pointed out that a modulation of the position x_n of the lattice atoms of the form $\delta x_n = \delta x_0 \cos(2k_F x + \phi)$, where k_F is the Fermi wavevector would produce gaps at $\pm k_F$ in the conduction band and, consequently, a reduction of the total electronic energy. The electronic density becomes modulated as $\rho = \rho_0 + \rho_1 \cos(2k_F x + \phi)$, with ρ_0 the unperturbed electron density of the metal. In Q1D metals at low temperatures, the elastic energy cost to modulate the atomic position is less than the gain in conduction electron energy, so the CDW state is the preferred ground state. Indeed, the CDW state has an energy that is lower by a logarithmic factor as compared to the normal state. At high temperatures the electronic energy gain is reduced by the thermal excitation of electrons across the gap, so the metallic state is stable. The second-order phase transition that occurs between the metallic and CDW state is called Peierls transition.

As depicted in Fig. 1.14, when an electric field is applied, the CDW can 'slide' relative to the lattice. The lattice atoms oscillate back and forth, producing a traveling potential and the conduction electrons move with this potential, resulting in a current. This means that CDW conductors have collective

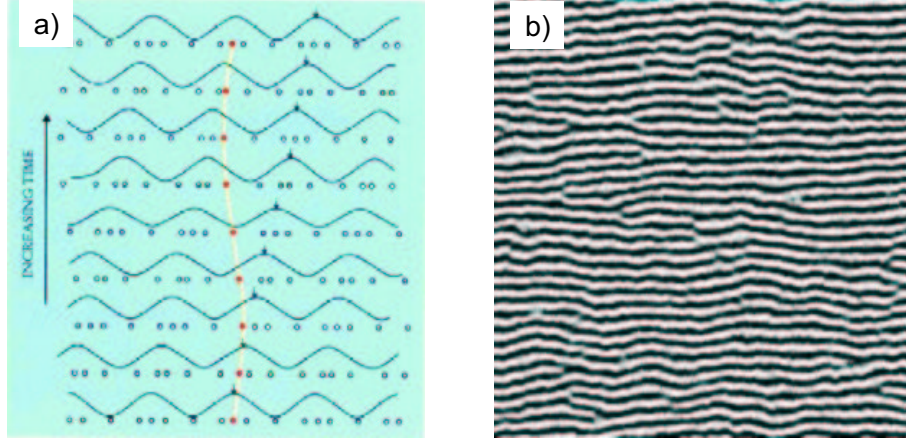


FIG. 1.14: Schematic of the CDW sliding (a) and experimental observation of CDWs in the pinned regime (b). From Ref. [83].

charge transport mode. This is one of the most intriguing features of this kind of systems. However, CDWs are pinned to the underlying lattice. If their wavelength $\lambda_c = \pi/k_F$ is an integer multiple of the lattice constant, then the CDW will have preferred positions relative to the lattice and when translated its energy will oscillate with a period λ_c . On the other hand, if the CDW's wavelength is incommensurate with the lattice period, as it is the case in most Q1D metals, then it will be pinned by impurities and other lattice defects. As in the commensurate case the energy oscillates with a period λ_c . In both cases the CDW remains pinned for small electric fields and it slides only with the application of fields that exceed a threshold field E_c determined by the pinning strength. Remarkably, not only in metals, but also in Q1D organic compounds evidence for the CDWs have been found [84].

1.3.2 Vortices in superfluids and type II superconductors

A magnetic field can penetrate a type-II superconductors as Abrikosov vortices (see Fig. 1.15), which form an ideal triangular lattice in a low-temperature region in the absence of pinning centers [26]. The superconducting properties of an infinite type-II film have been studied for more than half a century. Vortices in mesoscopic superconductors can be viewed as pseudo-particles interacting magnetically and through the encircling superconducting screening currents with each other [85]. When they are confined in one or two dimensions they

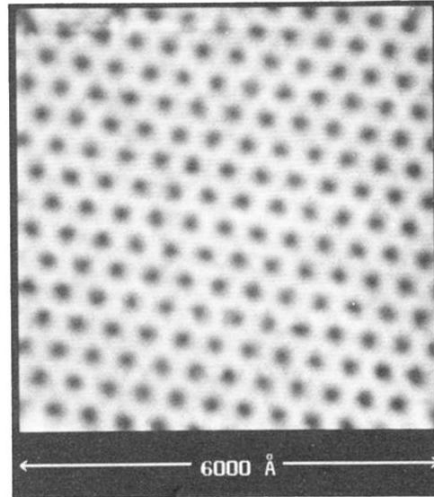


FIG. 1.15: The Abrikosov flux lattice is imaged in NbSe2 by tunneling into the superconducting gap edge with a low-temperature scanning-tunneling microscope. From Ref. [86].

can form chain-like patterns, somehow similar to the systems already discussed, although the vortex-vortex interactions are not barely electrostatic repulsions.

One natural way to realize a Q1D confinement is to consider a superconductor film for which one dimension is much larger than the others. It was shown by Abrikosov that when an infinitely long film is placed in an external magnetic field, parallel to its surfaces, vortices penetrate collectively into the sample and can arrange in the form of linear chains of parallel vortices. After the work of Abrikosov, many theoretical and experimental works have been carried out to study the vortex state in a type-II superconducting film. As the external magnetic field exceeds a critical value H_{c1} , which is a function of the film thickness, the linear chain arrangement of vortices start to penetrate into the sample. If the film is infinite the chains will penetrate one at the time [87]. The transition between two vortex states, differing by one linear chain, occurs at a well-defined critical magnetic field, known as the 'matching field'. Interestingly if the film is finite, the vortices can penetrate individually. As vortices enter the finite film, they align themselves and form a linear chain, parallel to the longer side of the film; as the number N of vortices increase inside the sample, the linear chain saturates and undergoes a transition, splitting into two new chains. This process continues from two to three chains and so on from m to $m + 1$ chains. By that there are two kinds of matching fields, one related to

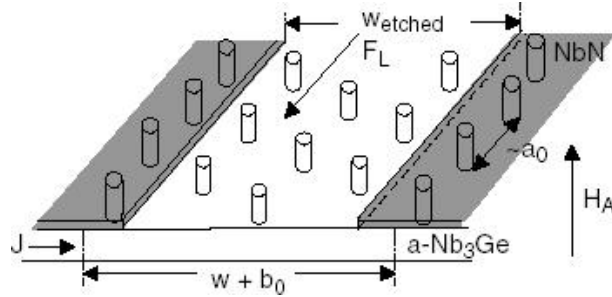


FIG. 1.16: Sketch of the artificial channel geometry. In the grey areas, vortices are pinned by the strong-pinning NbN layer, while inside the channels pinning due to material inhomogeneities is negligible. From Ref. [90].

the transition from a N to a $N + 1$ vortex state and the other one related to the m to $m + 1$ chain arrangements [87–89].

These transitions affect the magnetization, which exhibits a succession of low peaks related to the penetration of each vortex and high peaks for the transition to a state with a higher number of chains. The measurement of these peaks, therefore, can give indirect confirmation of single vortex penetration or chain rearrangements. It is, indeed, what was performed in the experiments of Ref. [89].

Another possibility for Q1D confined vortices is addressed in Ref. [90]. In these experiments a novel artificially structured superconducting device has been realized and discussed. It consists of narrow weak-pinning channels in a strong pinning superconducting film, as illustrated in Fig. 1.16.

The samples were fabricated by etching straight channels of width $w_{etched} \gtrsim 100nm$ through the top layer of an $a - NbGe/NbN$ double layer. With a magnetic field applied perpendicular to the film, vortices penetrate both the strong-pinning NbN in the channel edges and the remaining $NbGe$ weak-pinning channels. The strongly pinned channel edge vortices provide confinement to the vortices inside the channel, as well as the pinning potential which opposes the Lorentz force from a transport current J applied perpendicular to the channel. By changing the applied field H , it is possible to obtain different chain arrangements in the weak-pinning channels. Interesting properties are related to the commensurability or incommensurability between the natural vortex row spacing and the channel width. This experimental realization has demonstrated to be a very useful tool for detailed studies of the dynamical properties of vortices when a driving force is applied. Channel motion and its dependence on the structural properties of vortex matter have been studied systematically in

Ref. [90], where the chain structures are discussed also relatively to disorder strength in the edge channels.

Finally, the melting of the vortex lattice and the formation of a liquid vortex phase with the increase of temperature may take place. This effect was observed for high- T_c superconductors (for a review see Ref. [91] and references therein). In Ref. [92], the changes of the structure with temperature and the melting of clusters of vortices in axial-symmetric systems were studied.

1.3.3 Biological systems

If the 20th century was the 'century of physics', with the discovery and development of two building-blocks of human knowledge, i.e. the quantum and relativity theories, the 21st century is the 'age of biology', as many observers claim. The use of physics in biology research is rapidly growing. Biologists are moving into areas of study where they need tools that are traditionally physics related. Some examples are lasers to probe cell metabolism, statistical mechanics and molecular dynamics to analyze complex organic molecules, such as the DNA. Here, without the pretension of a detailed overview, we will briefly described some biochemical systems, in which Q1D Wigner crystal structures are present and determine interesting phenomena, that could have hopefully practical uses.

Very recently the so called DNA condensation has attracted a lot of attention. Under 'physiological' conditions (a 0.1 molar solution of $NaCl$), a DNA molecule takes on the form of a disordered coil with a radius of gyration of several micrometers; if any segment of the molecule comes within 1 nm of one another, they strongly repel. But under different conditions, that is in a highly dilute aqueous solution, also containing a small concentration of polyvalent cations, and eventually at low temperature, the same DNA molecule condenses into a tightly packed, circumferentially wound torus [93]. The same behavior is observed if, instead of a molecule, only very small DNA pieces are in solution: they can stick together forming agglomerates. DNA molecules belong to the class of polyelectrolytes, i.e. high polymeric substances containing ionic constituents which in solution acquire high charge. In general the formation of agglomerates is a phenomenon regarding different kind of polyelectrolytes, as organic salts, e.g. $(TMTTF)_2AsF_6$ (tetramethyltetrathiofulvalene), and biopolymers, e.g. filamentous actin fibers, microtubules, aggregating viruses and, obviously, DNA. The mutual attraction between polyelectrolytes [94] is a counterintuitive phenomenon, in apparent and dramatic contradiction to the fundamental fact that like-charged objects repel each other.

In general, in the presence of small amounts of polyvalent salts, the electrostatic interaction between polyelectrolytes is either attractive or so weakly repulsive that attractive forces of a different origin (e.g., hydrophobic or hydration interactions) overwhelm electrostatic repulsion. It is nowadays clear that

polyvalent counterions mediate an effective attraction between the negatively like-charged molecules, although no universal consensus exists for the precise mechanism. Electrostatics in aqueous media is commonly understood in terms of screened Coulomb interactions, where like-charged objects, always repel. These intuitive expectations are confirmed by mean field theories, such as the linear Debye-Hückel or the non-linear Poisson-Boltzmann formalisms, where the macroions are surrounded by clouds of micro counterions.

Two physical mechanisms have been suggested as possible reasons for the puzzling attraction [95]. When the distance between two polyelectrolytes is large their attraction is related to the correlation of long-wavelength thermal fluctuations of screening atmospheres of two polyelectrolytes. At smaller distances the strong electrostatic interaction of counterions leads to strong spatial correlations and even to their crystallization into Wigner lattices. In this situation, two crystals with proper phases attract each other. From theoretical models [96], treating the polyelectrolytes such as infinitely thin lines or smooth rods, and numerical simulations [97] it has been demonstrated that counterion Wigner lattices surrounding the macroions surfaces can attract each other. The above two attraction mechanisms are not necessarily in conflict with each other: the long-wavelength fluctuation effect appears for high temperatures, whereas the short-range correlations predominate at low temperatures.

In the experiment of Ref. [98] evidence for the formation of a Q1D Wigner crystal of counterions, which generates attraction between two filamentous actin rods, has been found. By using synchrotron X-ray diffraction it was possible to observe both the actin rods and the counterion arrangement. It was found that by increasing the concentration of counterions, they undergo a phase transition to an ordered Wigner crystal phase and form an electrostatic 'zipper' that 'fastens' the actin rods together, as illustrated in Fig. 1.17. Surprisingly, the counterions do not simply form a lattice which follows actin's helical symmetry; rather, they are modulated into 'frozen' ripples parallel to the actin filaments, resembling 1D charge density waves. Moreover, this 1D counterion charge density wave couples to twist distortions of the oppositely charged actin filaments.

It should be stressed that polyelectrolytes, and in particular DNA, attract themselves under a wide range of solution conditions, many of which are commonly realized in vivo. Furthermore, most of the important biomolecules (for example, nucleic acids and proteins) and large-scale biostructures (for example, cell membranes and extracellular protein networks) are highly-charged objects in aqueous solution. Indeed, they need to be charged to avoid precipitation and phase separation at the high concentrations that characterize them in vivo. Thus, understanding how nature controls the electrostatic interaction between biomolecules and biostructures is a fascinating challenge and hopefully it could have therapeutic applications.

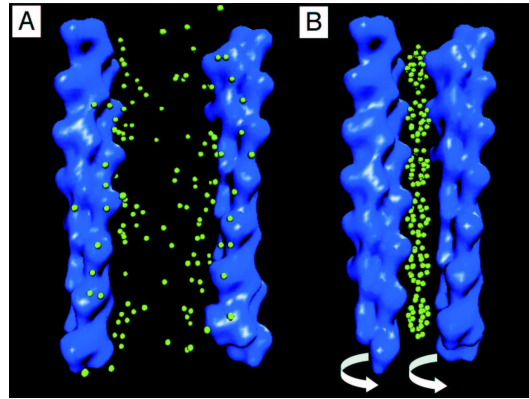


FIG. 1.17: Schematic representations of uncondensed and condensed F-actin. (A) At low multivalent ion concentrations, two F-actin filaments are unbound. (B) At high multivalent ion concentrations, the ions collectively form a Wigner crystal and bundle F-actin filaments. Moreover, the Wigner crystal forms a coupled mode with torsional distortions of the F-actin.

1.4 GENERAL PROPERTIES OF DRIVEN SYSTEMS

A remarkable variety of complex phenomena can show up when interacting systems, which form ordered or periodic arrays, are driven by an external force. These phenomena arise from a complicated interplay between periodicity, elasticity, substrate properties, nonlinearities and driving. Applying an external driving force and studying the transport features is usually a convenient way to probe the physics for such experimental systems and it is sometimes the only possible way to investigate them when more direct methods are not available (this is, for example, the case of electrons on liquid helium). In general, obtaining a quantitative description of driven dynamics is a very important problem across the whole condensed matter field. Wigner crystals, charge density waves and vortex lattices in type-II superconductors are a prominent example of systems forming periodic structures. In what follows, we will provide a description of some general features exhibited by such systems when an external driving force is applied along one direction. The majority of the investigations on driven systems has until now concentrated on 2D or 3D infinite lattices. In Chapter 6 we will address how low dimensionality and confinement affect the driven dynamics in the specific case of a Q1D system.

For a perfect lattice the application of a driving force should result in the sliding of the system. However, it is well known that the perfect lattice is only a

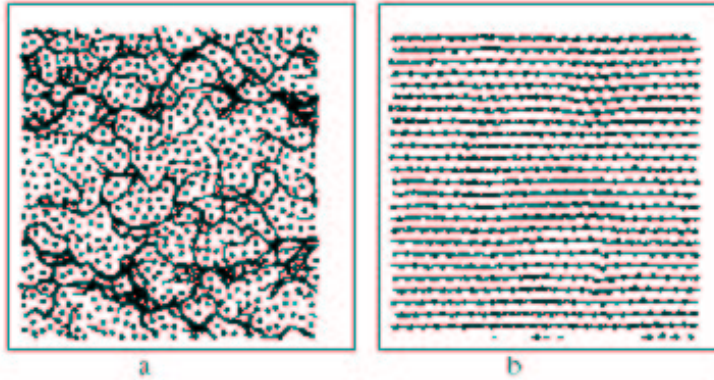


FIG. 1.18: Colloid positions (black dots) and trajectories (lines) for (a) plastic flow regime and (b) elastic flow regime. From Ref. [99].

formal useful model, which has no counterpart in real systems. Indeed, imperfections, defects, constraints, interactions with substrates (we will generically refer to them as disorder) are always present and they can influence dramatically the static and dynamical properties of the system. When disorder is present, one striking property exhibited by driven systems is pinning, i.e. the fact that at low temperature there is no macroscopic motion unless the applied force f is larger than a threshold critical force f_c . Once the force overcomes the critical value f_c , the system starts to flow. If the disorder is weak, the depinning proceeds through the so called *elastic flow*, where the system moves preserving a certain degree of translational order, or in other words the particles (electrons, ions, colloids in the case of Wigner crystals and vortices in the case of type-II superconductors) preserve their nearest neighbors during the motion. On the other hand, in the presence of a strong disorder, the depinning proceeds through *plastic flow* with a radically different behavior, where part of the system is moving and part is still pinned (see Fig. 1.18). Several experimental effects have been attributed to plastic flow, such as the peak effect, unusual broadband noise and fingerprint phenomena in the I-V curve in superconductors, just to give some examples.

While progresses towards a consistent theoretical treatment has been made in the statics in the presence of disorder, determining the various features of driven systems is still a widely open question. Evidence based mostly on experiments, numerical simulations and qualitative arguments indicates that quite generally plastic motion is expected for either strong disorder situations in 3D or near the depinning threshold in low dimensions.

It is generally agreed that disorder leads to loss of translational order, so that it is an important issue to characterize the degree of translational order in driven systems. In a series of recent works, Le Doussal and Giamarchi [100] predicted the existence of a new thermodynamic phase, the Bragg glass, when considering a static periodical structure in the presence of disorder. The Bragg glass is characterized by the fact that translational order decays at most algebraically at large scale and there are divergent Bragg peaks in the structure, which means that quasi-long-range order survives. They also elaborated a moving glass theory of driven lattices with disorder [101]. They investigated the effects of the periodicity of the moving lattice in the direction transverse to the motion. Their main findings were that: (i) some features of the static disorder are not affected by the motion, thus, the moving lattice is not a perfect crystal but a moving Bragg glass, (ii) the degrees of freedom which are transverse to the driving force strongly influence the driven dynamics. A very similar situation is present in the case of Q1D crystals, although with the significant difference that in the direction transverse to motion the degrees of freedom are not represented by periodicity, but rather by the interactions with the external confining potential.

In the context of elastic theory the problem of depinning and elastic flow have been faced theoretically with renormalization group techniques [101] or perturbative approaches in $1/v$ [102] (with v the average velocity of the system) at large driving forces. A complete theoretical description of the plastic flow is still lacking [103]. Most of the theoretical efforts have concentrated on the behavior of the driven system in the vicinity of the depinning threshold, especially for CDWs and vortex lattices [104–106]. In the experiments attention has been mainly posed to transport properties.

In order to understand the response of a system to an external drive, it is important to determine the curve of velocity v versus the applied force f . Through this $v - f$ characteristic, three main regimes can be distinguished and are shown in Fig. 1.19.

Far below the depinning threshold f_c the system is pinned and no motion is observed at $T = 0$ (for $T > 0$ the system moves through thermal activation in the so-called creep regime). The second regime, near the depinning transition $f \sim f_c$, has been intensely investigated in similarity with usual critical phenomena where the velocity plays the role of an order parameter. A particularly important question in that regime is to determine whether plastic rather than elastic motion occurs. Furthermore, it has been demonstrated that the velocity near the threshold scales as $v \sim (f - f_c)^\beta$ [103]. In the language of renormalization group theory, the depinning transition is a so called 'fixed point'. This scaling has been studied extensively and it was predicted theoretically [103] and confirmed in many experiment that in 2D systems $\beta = 2/3$ [99], when the depinning is elastic. In the case of plastic depinning, it is not possible to determine β from the theory; nonetheless, all the experimental results seem to agree with $\beta > 1$ in 2D [99, 107]. The third regime is far above the depinning

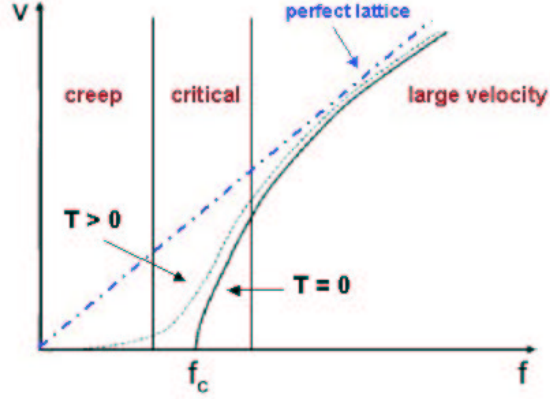


FIG. 1.19: A typical v - f characteristic at $T = 0$ (full line) and at finite temperature (dashed line). The sliding of a perfect lattice (dash-dotted line) is indicated. Three main regimes can be distinguished: the creep regime for forces well below threshold, the critical regime around the threshold, and the large velocity regime well above threshold.

threshold $f > f_c$. An important phenomenon in this regime is that of 'dynamical reordering'. Indeed, it was observed experimentally [108] that at large velocity the driven system is more translationally ordered than at low velocity. Intuitively the idea is that at large velocities the disorder should produce little effects. This tendency to dynamical reordering has also been seen in numerical simulations.

In the case of plastic flow the $v - f$ characteristic show hysteresis, i.e. it depends on the history of the system, as reported, for instance, in Ref. [11].

From Fig. 1.19 it is evident that the response to an external drive is highly non linear and that linear features are attained only for very large driving forces as asymptotic behavior.

The question of elastic versus plastic flow in the critical regime deserves further comments. In recent works by Koshelev and Vinokur [109] the effect of disorder and constraints on the moving structure was found to be equivalent to heating the system to an effective temperature $T' \sim T + T_{sh}$ with T_{sh} , which is termed 'shaking temperature', inversely proportional to the velocity. The idea of a shaking temperature suggest that at large velocity one should observe δ -function or algebraically decaying Bragg peaks characteristic of a crystal or a quasi-crystal at finite temperature. This could be a criterion for discriminating between the plastic and the elastic regime. In fact, if plastic flow occurs, the structure factor should signal some destruction of the lattice and then other

features than Bragg peaks should be observed. However, because a moving system is inherently anisotropic in the presence of (weak) disorder, different effects appear and the decay of the structure factor is not as isotropic as in the static system, even in the elastic flow regime. So this criterion can only be qualitative.

In the large velocity regime, where a theoretical description is possible, two preferential directions have been essentially followed in the literature. In the first approach the features of motion are fully characterized along the direction of the driving force and, subsequently, the motion in the transverse direction is incorporate as an extra complication. The second approach is based on the realization that the physics of periodic structures driven along one of their internal directions is radically different from the above descriptions. In Ref. [101] the periodicity in the transverse direction leads to a static nonlinear pinning force f_{stat} , that persists even in a fast moving system and produce transverse barriers to the motions. This results in a channel-like pattern, where the channels themselves are elastically coupled along the transverse direction through compression modes. The flow in the second approach is described in terms of static channels where the particles follow each other like beads on a string. In the laboratory frame these channels are determined by the static disorder and do not fluctuate in time. The channels are the easiest paths followed by the particles. A crucial difference between what would be observed for a perfect lattice, is that these channels are rough. The existence of channels naturally leads to several a priori possible regimes for the coupling between particles in different channels. The first case is a topologically ordered moving structure corresponding to full elastic coupling between particles in different channels. A second case of a moving structure corresponds to decoupling between the channels, by injections of dislocations beyond a certain length scale. The transition from the first to the second case depends obviously on the disorder strength. Upon increase of disorder the first likely transition corresponds to a decoupling of the channels, while the periodicity along the transverse direction is maintained. Increasing further the disorder should destroy even the channel structure and the elastic flow should turn into a fully plastic flow.

An important question for a driven system is to understand what is the effect of thermal fluctuations. Indeed, in moving systems a generation of temperature by motion occurs. The finite temperature moving structure exhibits generally the same type of rough channel structure as the moving structure at $T = 0$ [101]. Channels are slightly broadened due to bounded thermal displacements around the average channel position. The behavior of the displacements and structure factor for temperature not too close to the melting point still remains similar to that at zero temperature. The main effect of temperature is to modify the $v - f$ characteristics, as illustrated in Fig. 1.19. One finds that the mobility of particles is nonzero even in the pinned regime for low temperatures. However, at low temperatures or at velocities not too large the $v - f$ characteristics

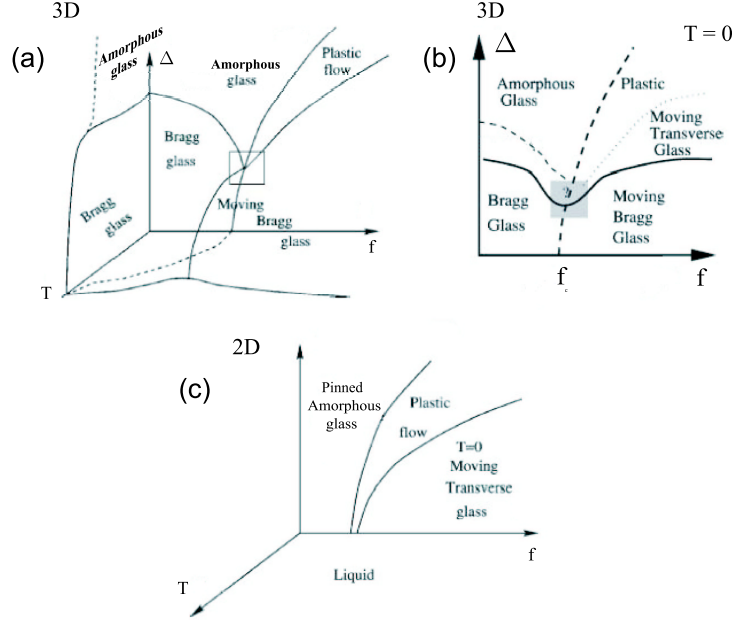


FIG. 1.20: (a) Schematic phase diagram in the temperature T , disorder Δ , applied force f variables for 3D driven systems. The connections between the various phase boundaries inside the square region is schematic; (b) the same as (a), but in the plane $T = 0$; (c) the same as (a), but for 2D driven systems.

remain highly nonlinear. Hence, the properties of the finite-temperature phase are continuously related to the $T = 0$ phase.

A phase diagram as a function of the disorder Δ , the temperature T , and the applied force f for driven lattices in 2D and 3D space has been proposed by Le Doussal and Giamarchi in Ref. [101] for 2D and 3D. This is shown in Fig. 1.20(a).

At zero external force, one recovers the static phase diagram. In 3D there is a transition at finite disorder strength between the Bragg glass to an amorphous glass where no long-range order is retained. Upon applying a force the Bragg glass phase becomes the moving Bragg glass in the creep regime and continuously extend to the moving Bragg glass at higher drives. At weak enough disorder the continuity between the two phases suggests that depinning should be elastic without an intermediate plastic region. Upon raising the temperature the moving Bragg glass melts to a liquid, presumably through a first-order dynamical melting transition. The $T = 0$ (see Fig. 1.20(b)) plane contains a pinned region for $f < f_c$ and it is natural to expect the Bragg glass to still

exist even for a finite force $f < f_c$ until the depinning transition. At higher disorder dislocations appear and the Bragg glass is replaced by an amorphous glass. The nature of this amorphous phase is not very clear, but it is sure to contain topological defects. Thus the depinning of this amorphous glass should be via a highly disordered filamentary plastic flow. Upon increasing the force and thus the velocity, the system should reverse back to the moving Bragg glass, since the dynamical reordering effect. One of the strong features that emerges from these phase diagrams is the fact that the Bragg glass is able to survive motion by turning into the moving Bragg glass. On the other hand, more disordered phases such as the amorphous glass are likely to be immediately destroyed at finite drive (and finite temperature) and to be continuously related to the liquid. In 2D the static phase diagram is still unresolved. A reasonable assumption is that there is no long-range topological order [91, 100] according to the Mermin-Wagner theorem [135], although this is far from being firmly established. At $f = 0$ and finite disorder, dislocations are expected to be present. The resulting phase should thus be continuously connected to the liquid, although it can retain good short distance translational order (see Fig. 1.20(c)). At $T = 0$ there is a pinned phase until f_c , which should depin by either an elastic or a plastic flow. At larger drive disorder effects become smaller and the system is expected to revert to a moving glass state. In Chapter 6 we will compare this general picture with our results for a Q1D driven crystal, stressing the analogies and the differences. In particular we will show that in the Q1D geometry the motion takes place in a channel-like flow and that between the elastic and plastic regimes, another regime, which we term *quasi-elastic regime* is present due to the low dimensionality and to the specific kind of constraints.

Finally, the static channels were clearly observed, for example, in Ref. [110] at $T = 0$ in 2D. In Refs. [110, 111] evidence of the transverse critical force was found. The moving glass picture has also been confronted with several experiments, especially in the case of vortices in type-II superconductors. The lattice is observed to move in the symmetry axis direction and relatively large regions of highly correlated static channels are observed. Another set of experiments in $NBS e_2$, also exhibiting channels, was reported [112]. Other effects of the moving crystal-like structure and transverse critical force can be found in systems other than vortex lattices. Indeed, the transverse barriers may explain the anomalies recently observed in the Hall effect in a Wigner crystal in a constant magnetic field [113].

2

Model System and Numerical Approach

In the present thesis we are mainly interested in quasi-one-dimensional systems consisting of an infinite number of particles, where the inter-particle interaction is described by a screened Coulomb potential (Yukawa type). The quasi-one-dimensional nature is ensured by an external confining potential acting in one direction only, namely the y -direction. The energy for such a system is described by the Hamiltonian:

$$H = \frac{q^2}{\varepsilon} \sum_{i>j} \frac{\exp(-|\mathbf{r}_i - \mathbf{r}_j|/\lambda)}{|\mathbf{r}_i - \mathbf{r}_j|} + \sum_i \frac{1}{2} m \omega_0^2 y_i^2 + \sum_i V(\mathbf{r}_i). \quad (2.1)$$

where m is the effective mass of the particles, ε is the dielectric constant of the medium the particles are moving in, q is the charge, λ is the screening length, $\mathbf{r}_i = (x_i, y_i)$ is the position of the i -th particle and ω_0 is frequency of the confining potential. $V(\mathbf{r}_i)$ is an eventually present single particle potential, related to a constriction. The indices i and j run from 1 to infinity. By introducing appropriate energy and length units, E_0 and r_0 respectively, as illustrated in the next sections, the Hamiltonian assumes the dimensionless form:

$$H' = \sum_{i>j} \frac{\exp(-\kappa|\mathbf{r}'_i - \mathbf{r}'_j|)}{|\mathbf{r}'_i - \mathbf{r}'_j|} + \sum_i y_i'^2 + \sum_i V'(\mathbf{r}'_i). \quad (2.2)$$

where $H' = H/E_0$, $\mathbf{r}'_i = \mathbf{r}/r_0$ and $\kappa = r_0/\lambda$.

We studied the static and dynamical properties of a system of equally charged particles described by such an Hamiltonian. The static or equilibrium configuration is the one that minimizes the energy. For this purpose we performed both analytical calculations and Monte Carlo simulations. When an external driving force is applied to the system, interesting phenomena can appear due to the low dimensionality. In order to study this problem and to follow the dynamics of the particles we performed Molecular Dynamics simulations. In what follows we will provide few general remarks about the Hamiltonian of a strong interacting and confined system and its scaling laws. Also we will give a brief overview of optimization techniques, namely Monte Carlo and simulated annealing, and of Molecular Dynamics simulations.

2.1 GENERAL HAMILTONIAN AND THE CLASSICAL LIMIT

The full quantum mechanical Hamiltonian which describes N identical charged particles moving in two dimensions, interacting through an electrostatic potential U , subject to an external parabolic confinement and in the presence of a general single particle potential V , has the form:

$$H = - \sum_{i=1}^N \frac{\hbar^2}{2m} \nabla_i^2 + \frac{q^2}{\varepsilon} \sum_{i=1}^{N-1} \sum_{j=i+1}^N U(|\mathbf{r}_i - \mathbf{r}_j|) + \sum_{i=1}^N \frac{1}{2} m \omega_0^2 r_i^2 + \sum_{i=1}^N V(\mathbf{r}_i), \quad (2.3)$$

where m is the effective mass of the particles, ε is the dielectric constant of the medium the particles are moving in, $\mathbf{r}_i = (x_i, y_i)$ is the position of the i -th particle with $r_i \equiv |\mathbf{r}_i|$ and ω_0 is frequency of the confining potential. The potential $U(|\mathbf{r}_i - \mathbf{r}_j|)$ can have several forms and can describe a large variety of interaction types.

For sake of simplicity, in what follows we will consider particles interacting through Coulomb interaction, that is:

$$U(|\mathbf{r}_i - \mathbf{r}_j|) = \frac{1}{|\mathbf{r}_i - \mathbf{r}_j|},$$

and will refer to the particles as electrons.

By introducing the oscillator length $a_0 = \sqrt{\hbar/m\omega_0}$ and the energy quantum $\hbar\omega_0$ as units of length and energy, respectively, it is possible to express the Hamiltonian (2.3) in the dimensionless form:

$$H' = -\frac{1}{2} \sum_{i=1}^N \nabla_i'^2 + \sigma^3 \sum_{i=1}^{N-1} \sum_{j=i+1}^N \frac{1}{|\mathbf{r}'_i - \mathbf{r}'_j|} + \frac{1}{2} \sum_{i=1}^N r_i'^2 + \sum_{i=1}^N V'(\mathbf{r}'_i), \quad (2.4)$$

where the dimensionless constant $\sigma^3 = \sqrt{(me^4/\varepsilon^2\hbar^2)/\hbar\omega_0} = a_0/a_B$, with $a_B = \varepsilon\hbar/(me^2)$ the effective Bohr radius of the electrons. The constant σ measures the strength of the electron-electron interaction. For strongly confined systems the value of ω_0 will be very large, thereby the coupling constant σ will be quite small. In the limit of small σ , the Hamiltonian (2.4) reduces to the Hamiltonian of non-interacting particles in a harmonic oscillator potential and the electron-electron interactions can be treated as a perturbation. On the other hand, for strongly interacting systems a large value of σ is expected. It is interesting to look at the Hamiltonian after the rescaling of the length $r' \rightarrow \sigma r''$. It yields:

$$H'' = -\frac{1}{2\sigma^2} \sum_{i=1}^N \nabla_i''^2 + \sigma^2 \left(\sum_{i=1}^{N-1} \sum_{j=i+1}^N \frac{1}{|\mathbf{r}_i'' - \mathbf{r}_j''|} + \frac{1}{2} \sum_i^N r_i''^2 \right) + \sum_{i=1}^N V' \left(\frac{\mathbf{r}_i''}{\sigma} \right). \quad (2.5)$$

This shows that for strongly correlated systems the potential energy increases as σ^2 and the kinetic energy goes to zero. These considerations lead to the *classical limit* in which the electrons, or more in general the interacting particles, can be treated as localized and the ground state configuration, i.e. the equilibrium configuration at zero temperature, can be obtained by minimizing the potential energy:

$$W = \sum_{i=1}^{N-1} \sum_{j=i+1}^N U(|\mathbf{r}_i'' - \mathbf{r}_j''|) + \frac{1}{2} \sum_i^N r_i''^2 + \sum_{i=1}^N V(\mathbf{r}_i''). \quad (2.6)$$

2.2 SCALABILITY AND DIMENSIONLESS UNITS

For classical systems which are described by a Hamiltonian of the form:

$$H = \frac{q^2}{\varepsilon} \sum_{i=1}^{N-1} \sum_{j=i+1}^N U(|\mathbf{r}_i - \mathbf{r}_j|) + \sum_i^N \frac{1}{2} m\omega_0^2 r_i^2 + \sum_{i=1}^N V(\mathbf{r}_i), \quad (2.7)$$

it is always possible to set the energy into a dimensionless form by using appropriate units for the length and the energy.

In what follows we will focus on the most significant cases or, in other words, on different kinds of interactions among particles, which are interesting in 2D mesoscopic systems. We will neglect the single particle potential $V(\mathbf{r}_i)$ in order to avoid complications in the notation. Notice that in the rescaling procedure $V(\mathbf{r}_i)$ is merely divided by the unit of energy, so we can consider $V(\mathbf{r}_i) = 0$ without loss of generality. The fundamental ingredients in the rescaling are the inter-particle interaction type and the parabolic confinement.

- Coulomb and Yukawa (Debye-Hückel) potential.

Coulomb interaction is the typical interaction between charged particles immersed in a polarizable medium, whose effect is contained in the dielectric constant ε , and has the form $1/|\mathbf{r}_i - \mathbf{r}_j|$. Yukawa (Debye-Hückel) interaction or screened Coulomb interaction is normally encountered in systems like complex plasmas or colloidal suspensions. This kind of interaction is, in general, related to the presence of an active background, which weakens the original Coulomb interactions among the particles, and has the form $\exp(-|\mathbf{r}_i - \mathbf{r}_j|/\lambda_D)/|\mathbf{r}_i - \mathbf{r}_j|$, where λ_D is the screening length.

In these cases the Hamiltonian can be rewritten in a dimensionless form, introducing the quantities:

$$r_0 = (2q/m\varepsilon\omega_0^2)^{1/3}, \quad (2.8a)$$

$$E_0 = (m\omega_0^2 q^4 / 2\varepsilon^2)^{1/3}, \quad (2.8b)$$

as units of length and energy, respectively. It yields:

$$H = \sum_{i=1}^{N-1} \sum_{j=i+1}^N \frac{1}{|\mathbf{r}'_i - \mathbf{r}'_j|} + \sum_i^N r_i'^2, \quad (2.9)$$

for the Coulomb interactions, and

$$H = \sum_{i=1}^{N-1} \sum_{j=i+1}^N \frac{\exp(-\kappa|\mathbf{r}'_i - \mathbf{r}'_j|)}{|\mathbf{r}'_i - \mathbf{r}'_j|} + \sum_i^N r_i'^2, \quad (2.10)$$

for the screened Coulomb interactions, with $\mathbf{r}'_i = \mathbf{r}_i/r_0$ and $\kappa = r_0/\lambda_D$.

The rescaling is particularly interesting because it gives the model a high degree of generality. Indeed, the specific features of the system (i.e., the mass of the particles m , the charge q , the dielectric constant ε and the strength of the confining parabolic potential ω_0) are no longer explicitly present. Notice that for Coulomb interaction the energy (2.9) depends only on the number of particles N , while for screened Coulomb interactions the energy (2.10) depends on N and κ , which is an external parameter. In the limit $\kappa \rightarrow 0$ the Yukawa potential reduces to the pure Coulomb potential, while in the opposite limit $\kappa \rightarrow \infty$ it gives a nearly free particle interaction.

- Dipole potential.

Dipole interaction is commonly found in suspensions of colloidal particles, which acquire dipole moments under the application of a magnetic field. They have a pairwise interaction of the form $d^2/|\mathbf{r}'_i - \mathbf{r}'_j|^3$, where d is a parameter that depends on the experiment. The Hamiltonian for such a system is given in dimensionless units as:

$$H = \sum_{i=1}^{N-1} \sum_{j=i+1}^N \frac{1}{|\mathbf{r}'_i - \mathbf{r}'_j|^3} + \sum_i^N r_i'^2, \quad (2.11)$$

with

$$r_0 = d^{2/5} (m\omega_0^2/2)^{-1/5} \quad (2.12a)$$

$$E_0 = m\omega_0^2 r_0^2/2, \quad (2.12b)$$

as units of length and energy, respectively.

- Logarithmic potential.

Vortices in type II superconductors or in superfluid helium exhibit logarithmic inter-particle interactions. If a type II superconducting cylinder of radius R (whose length is much greater than R) is placed in a magnetic field, that is parallel to the axis of the cylinder, vortices will appear in the cylinder. They are parallel to each other as well as to the axis of the cylinder. Each such vortex will carry a current around it in the anticlockwise direction. The current due to two nearby vortices will be opposite to each other and hence lead to a repulsion between the two vortices. In Ref. [114] for such a type II sample it is shown that the interaction potential between vortices, when the magnetic field penetration length $\lambda \gg \xi$ (with ξ the coherence length), is given by $V(r) = \beta K_0(r/\lambda)$, where K_0 is the zero order Hankel function with imaginary argument, $\beta = \Phi_0/(2\pi\lambda^2)$ and $\Phi_0 = hc/2e$ is the flux quantum. In the extreme type II limit of $\lambda \rightarrow \infty$, this potential becomes logarithmic: $V(r) = -\beta \ln(r)$ up to a constant. Thereby, the potential energy of a 2D system of N vortices in a parabolic confinement potential and interacting through a two body logarithmic potential is given by:

$$H = -\beta \sum_{i=1}^{N-1} \sum_{j=i+1}^N \ln |\mathbf{r}_i - \mathbf{r}_j| + \sum_i^N \frac{1}{2} \omega_0^2 r_i^2. \quad (2.13)$$

This Hamiltonian takes the dimensionless form

$$H = - \sum_{i=1}^{N-1} \sum_{j=i+1}^N \ln |\mathbf{r}'_i - \mathbf{r}'_j| + \sum_i^N r_i'^2, \quad (2.14)$$

if one expresses the coordinates and the energy in the following units, respectively:

$$r_0 = \beta^{1/2} (m\omega_0^2/2)^{-1/2}, \quad (2.15a)$$

$$E_0 = \beta. \quad (2.15b)$$

So far, we have discussed the possibility of rescaling the Hamiltonian in the presence of an external parabolic confinement. It is possible to show that in the case of more general confinements and inter-particle potential, it is always possible to express the energy in dimensionless units. The potential energy of a 2D system of N charged particles in an r^n confinement potential and interacting through a two body potential is given by:

$$H = \sum_{i=1}^{N-1} \sum_{j=i+1}^N V(|\mathbf{r}_i - \mathbf{r}_j|) + \sum_i^N \frac{1}{2} m\omega_0^2 R^2 \left(\frac{r_i}{R}\right)^n. \quad (2.16)$$

A hard wall confinement is obtained for $n \rightarrow \infty$ and in this case R equals the radius of the hard wall. We will discuss the scaling for a general repulsive potential $1/r^l$, but similar considerations and scaling laws are also valid for the logarithmic interactions [115]. The Hamiltonian (2.16) assumes, then, the explicit form:

$$H = \frac{q^2}{\varepsilon R} \sum_{i>j}^N \frac{R^l}{|\mathbf{r}_i - \mathbf{r}_j|^l} + \sum_i^N \frac{1}{2} m\omega_0^2 R^2 \left(\frac{r_i}{R}\right)^n. \quad (2.17)$$

The model has now two external parameters, namely R and q^2/ε . Using the following units for length and energy:

$$r_0 = \left(\frac{q^2}{\varepsilon\alpha}\right)^{1/(n+l)} R^{(n+l-3)/(n+l)}, \quad (2.18a)$$

$$E_0 = (q^2/\varepsilon)^{n/(n+l)} \alpha^{(l)/(n+l)} R^{(2l-n)/(n+l)}, \quad (2.18b)$$

with $\alpha = m\omega_0^2/2$, the dimensionless Hamiltonian is:

$$H = \sum_{i>j}^N \frac{1}{|\mathbf{r}'_i - \mathbf{r}'_j|^l} + \sum_i^N r_i'^n, \quad (2.19)$$

with the hard wall potential limit

$$V(R) = \begin{cases} 0 & \text{for } r \leq 1; \\ \infty & \text{for } r \geq 1. \end{cases} \quad (2.20)$$

In the limit of a hard wall confinement, the unit of length becomes $r \rightarrow R$. It is easy to recognize that Eqs. (2.8a) and (2.8b) are special cases of Eqs. (2.18a) and (2.18b), when $n = 2$.

2.3 ENERGY MINIMIZATION

Function optimization is one of the key-points in numerical analysis. Generally, the function to be optimized (minimized) is an energy in order to get the ground

state of a system. The energy landscape of a system with a large number of degrees of freedom has a huge number of minima. The challenging task of the optimization techniques is to find out the global minimum.

The main difficulty in every optimization algorithm is to prevent the calculations to settle in a local minimum. The energy at a local minimum may be much higher than the energy of the global minimum. Then the system is not in a stable state, but in a so called "metastable" state. Here we will describe two powerful methods to achieve function optimization.

2.3.1 Monte Carlo simulations

In order to find the global minimum Monte Carlo (MC) simulations, together with the simulated annealing technique, are very powerful tools. Numerical methods that are known as Monte Carlo methods can be loosely described as statistical simulation methods, where statistical simulation is defined in quite general terms to be any method that utilizes sequences of random numbers to perform the simulation. In the past several decades this approach has gained the status of a full-fledged numerical method capable of addressing the most complex applications. MC is now used routinely in many diverse fields.

Assuming that the evolution of the physical system under investigation can be described according to a probability density functions (PDF), then the MC simulation can proceed by sampling from these PDF. This operation, in general, requires a fast and effective way to generate random numbers uniformly distributed on the interval [0,1]. The essential characteristic of MC is the use of random sampling techniques (and perhaps other algebra to manipulate the outcomes) to arrive to a solution of the physical problem.

Considering an observable A , a function of the point \mathbf{s} in the N -dimensional space, which is characterized by a PDF $p(\mathbf{s})$, MC methods allow to calculate the mean value of A as:

$$\langle A \rangle = \int d\mathbf{s} p(\mathbf{s})A(\mathbf{s}).$$

Without entering into too many technical details, we will briefly describe the MC Metropolis algorithm, which is actually one of the best strategies to sample the phase space of physical systems. Though the original applications of the Metropolis method [2] was to a classical system of hard disks, the algorithm has since then been found indispensable for many different applications.

The Metropolis algorithm is defined as follows: suppose that \mathbf{s} is a state in a phase space and that the goal is to sample the distribution function $p(\mathbf{s})$. In the simplest algorithm, there is a single transition probability: $\Pi(\mathbf{s} \rightarrow \mathbf{s}')$ between two states in the phase space. A move is proposed with probability $\Sigma(\mathbf{s} \rightarrow \mathbf{s}')$ and then it is accepted or rejected, with an acceptance probability $\Omega(\mathbf{s} \rightarrow \mathbf{s}')$. Detailed balance and ergodicity are sufficient to ensure that the random walk,

after enough iterations, will converge to $p(\mathbf{s})$. By detailed balance one means that the relation

$$p(\mathbf{s})\Sigma(\mathbf{s} \rightarrow \mathbf{s}')\Omega(\mathbf{s} \rightarrow \mathbf{s}') = p(\mathbf{s}')\Sigma(\mathbf{s}' \rightarrow \mathbf{s})\Omega(\mathbf{s}' \rightarrow \mathbf{s})$$

is fulfilled and by ergodicity that there is a non-zero probability of making a move from any state to any other state in a finite number of moves. This class of algorithms are also known as Markov Chain Monte Carlo (MCMC). The generalization of Metropolis to non-uniform transitions was suggested by Hastings [116]. Key defining features of MCMCs are the use of detailed balance to drive the distribution to a desired equilibrium state and, in particular, the use of rejections to achieve this purpose.

In the 'classic' Metropolis algorithm, the phase space is the $3N$ vector space of the coordinates of particles and the distribution to be sampled is the classical Boltzmann distribution $\exp(-E(\mathbf{s})/k_B T)$, where E is interpreted as energy and T as temperature. The thermodynamical ensemble associated to this probability distribution is the canonical ensemble, where the system is thought in thermal equilibrium with a reservoir at temperature T . The moves consist of single particle random displacements chosen uniformly in a hypercube centered around the current position and the moves are accepted with probability given by

$$\min[1, \exp(-(E(\mathbf{s}) - E(\mathbf{s}'))/k_B T)],$$

Other choices are possible for the acceptance-rejection criterion of the moves [117].

It is essential that the random displacement should not introduce a bias into the sampling. The efficiency of the algorithm depends on the random number generator and on the choice of the random displacements. When the displacement is very small almost every move will be accepted, but it will take a large number of moves to cover the whole available phase space, on the contrary when the displacement is very large the acceptance ratio will be very small.

A big advantage of Metropolis methods is that only energies need to be calculated, neglecting the real time evolution of the system. The counterpart is that in this way it is possible to get average values of observables depending only on the system configurations, that is on the particle positions. In order to determine quantities, which depend also on the particle velocities, it is still possible to introduce some improvements in the technique, but usually one prefers to use other numerical methods, namely Molecular Dynamics simulations.

2.3.2 The simulated annealing approach

Simulated annealing is a well-known stochastic method for global optimization that is inspired to thermodynamics. It combines the fast convergence speed of the Metropolis algorithm at high temperature with the high probability of

finding the optimal solution at low temperature. The basic idea is to start from a very high temperature and then to slowly lower it. This approach is the computer analogue of the thermal process, called annealing (hence the name), used in condensed matter physics to obtain solids with low energy states, for example in steel production and crystallization processes. By mean of the simulated annealing procedure the system is given the opportunity to surmount energetic barriers around the local minima and to explore larger portions of the phase space in the search for the global minimum.

An annealing schedule describes the rate by which the temperature T is lowered over time. It is possible to prove a general convergence criterion [118]. If T_n denotes the sequence of temperature, the simulated annealing procedure converges if $T_n \rightarrow 0$ for $n \rightarrow \infty$ and $T_n \geq (N\Delta)/\ln(1+n)$, where N is the number of degrees of freedom of the system and $\Delta = E_{max} - E_{min}$. In general, it is possible to give statistical guarantees of finding the optimal solution with the simulated annealing technique. These kinds of algorithms can deal with any energy function, are easy to implement and generally give 'good' solutions, although they are very computer demanding and slow because they perform millions of iterations for each temperature step.

2.4 MOLECULAR DYNAMICS

Molecular Dynamics (MD) is a computer simulation technique where the time evolution of a set of interacting particles is followed by integrating their equations of motion. Classical mechanics law, very often in the form of Newton's law, are used. Time integration is based on finite difference methods, where the time is discretized on a finite grid, with the time step Δt as the distance between consecutive points on the grid. Knowing the positions and their time derivatives at time t' , the integration scheme gives the same quantities at a later time $t' + \Delta t$. By iterating the procedure, the time evolution of the system can be followed for long times. Hence, in contrast with the MC method, Molecular Dynamics is a deterministic technique, in the sense that given an initial set of positions and velocities, the subsequent time evolution is, in principle, completely determined.

In general, MD simulations calculate a trajectory in a $6N$ -dimensional phase space ($3N$ positions \mathbf{r} and $3N$ momenta \mathbf{p}). However, such trajectory is usually not particularly relevant by itself. Like Monte Carlo methods, MD provides a set of configurations distributed according to some statistical distribution function, or statistical ensemble, depending on the specific equations of motions describing the system. Therefore, a measurements of a physical quantity A by MD simulations is simply obtained as an arithmetic average of the various instantaneous values assumed by that quantity during the runs:

$$\langle A(\mathbf{r}, \mathbf{p}) \rangle = \frac{1}{L} \sum_{m=1}^L A[(\mathbf{r}(t_0 + m\Delta t), (\mathbf{p}(t_0 + m\Delta t))],$$

where t_0 is the time at which the simulation starts and L is the total number of runs. In the limit of very long simulation times, for systems at equilibrium, one could expect the phase space to be fully sampled, and in that limit the averaging process would provide the 'correct' results.

MD is a very useful tool and is nowadays indispensable for studying the properties of liquid and gas systems, defects in crystals, surfaces; it provides informations in electronic and transport properties, biomolecules and non-equilibrium processes [119]. It can also be used for the optimization of structures overcoming local energy minima (together with the simulated annealing technique).

On the general plane, a MD simulation integrates the differential equations:

$$m_i \frac{d^2 \mathbf{r}_i}{dt^2} = \mathbf{F}_i(\mathbf{r}_1, \dots, \mathbf{r}_n, \frac{d\mathbf{r}_1}{dt}, \dots, \frac{d\mathbf{r}_n}{dt}),$$

for each particle i of the system, constituted by n particles, with m_i the mass of the i -th particle and \mathbf{F}_i the force acting upon it. When the forces are independent of the velocity, which is the case for a large variety of systems of interest, and when they can be obtained as the gradient of a potential:

$$\mathbf{F}_i = \nabla_{\mathbf{r}_i} V(\mathbf{r}_1, \dots, \mathbf{r}_n),$$

the mechanical energy is conserved or, stated differently, the system of n particles evolves in the microcanonical ensemble. In this case the knowledge of the potential V is the only requirement to start a MD simulation. When the forces acting on the particles cannot be simply deduced from a potential or when the evolution takes place in a different thermodynamical ensemble, either the equation of motions should be modified (we will provide with more details in section 2.4.2) or the time integration algorithm should be slightly changed with the introduction of some intermediate steps which appropriately rescale the observables in order to reproduce the correct dynamics [120]. In these cases, some forces are derived from a potential and other additional effects are included. Hence, the choice of the potential is a key point in every MD simulation. Together with the time integration strategy, they are the heart of MD techniques. The development of accurate potentials represents an important research line.

2.4.1 Different algorithms for the integration of Newton's equations

The time integration algorithms can be divided into three main classes: the Verlet, the leap-frog and the predictor-corrector algorithm. Here, we illustrate their basic features.

- The Verlet algorithm

In Molecular Dynamics, the most commonly used time integration algorithm is probably the so-called Verlet algorithm [121]. The basic idea is to write two third-order Taylor expansions for the positions $\mathbf{r}(t)$, one forward and one backward in time and then to sum them up, in order to cancel the odd power terms:

$$\begin{aligned}\mathbf{r}(t + \Delta t) &= \mathbf{r}(t) + \mathbf{v}(t)\Delta t + (1/2)\mathbf{a}(t)\Delta t^2 + (1/6)\mathbf{b}(t)\Delta t^3 + O(\Delta t^4), \\ \mathbf{r}(t - \Delta t) &= \mathbf{r}(t) - \mathbf{v}(t)\Delta t + (1/2)\mathbf{a}(t)\Delta t^2 - (1/6)\mathbf{b}(t)\Delta t^3 + O(\Delta t^4),\end{aligned}$$

where \mathbf{v} , \mathbf{a} , \mathbf{b} are, respectively, the velocity, the acceleration and the third derivative of the position with respect to the time. Adding the last two expressions, it yields:

$$\mathbf{r}(t + \Delta t) = 2\mathbf{r}(t) - \mathbf{r}(t - \Delta t) + \mathbf{a}(t)\Delta t^2 + O(\Delta t^4),$$

which provides the basic form of the algorithm. From the equations of motion it immediately turns out that:

$$\mathbf{a}(t) = -(1/m)\nabla V(\mathbf{r}(t)).$$

The strategy is, therefore, to calculate the positions, subsequently the forces and, then, to iterate the procedure.

Verlet algorithm is clearly a fourth order algorithm (i.e., it neglects the terms of order Δt^4), furthermore it is easy to implement and quite accurate and stable. In this version of the Verlet algorithm the velocities are not directly calculated, so in this form the algorithm is not suitable for determining observables which depend explicitly on the velocities. To overcome these difficulties the algorithm can be improved. The most common variant of the basic algorithm is the 'velocity Verlet scheme', which has the following form:

$$\begin{aligned}\mathbf{r}(t + \Delta t) &= \mathbf{r}(t) + \mathbf{v}(t)\Delta t + (1/2)\mathbf{a}(t)\Delta t^2, \\ \mathbf{v}(t + \Delta t/2) &= \mathbf{v}(t) + (1/2)\mathbf{a}(t)\Delta t, \\ \mathbf{a}(t + \Delta t) &= -(1/m)\nabla V(\mathbf{r}(t + \Delta t)), \\ \mathbf{v}(t + \Delta t) &= \mathbf{v}(t + \Delta t/2) + (1/2)\mathbf{a}(t + \Delta t)\Delta t.\end{aligned}$$

- Leap-frog algorithm

In the 'Leap-frog' algorithm the velocities are first calculated at time $t + \Delta t/2$, then they are used to calculate the positions at time $t + \Delta t$. This method gets its name from the way in which positions and velocities are calculated in an alternating sequence: the velocities leap over the positions, then the positions leap over the velocities. The algorithm has the form:

$$\begin{aligned}\mathbf{v}(t + \Delta t/2) &= \mathbf{v}(t - \Delta t/2) - (1/m)\nabla V(\mathbf{r}(t)), \\ \mathbf{r}(t + \Delta t) &= \mathbf{r}(t) + \mathbf{v}(t + \Delta t/2)\Delta t.\end{aligned}$$

The leap-frog scheme can be, therefore, seen as another variant of the basic Verlet algorithm. Its advantage is that the velocities are explicitly calculated, however, the disadvantage is that they are not calculated at the same time as the positions. The velocities at time t can be approximated by the relationship:

$$\mathbf{v}(t) = [\mathbf{v}(t + \Delta t/2) + \mathbf{v}(t - \Delta t/2)]/2.$$

- Predictor-corrector algorithm

The predictor-corrector methods form a large class of general methods for numerical integration of ordinary differential equations. Those more often used in Molecular Dynamics are due to Gear [122].

The first step of this algorithm consists in evaluating particle positions and velocities at time $t + \Delta t$ from the positions and the velocities at time $t - i\Delta t$, where $i = 0, \dots, k-2$, with k being the order of the algorithm. The extrapolation is given by

$$\begin{aligned}\mathbf{r}(t + \Delta t) &= \mathbf{r}(t) + \mathbf{v}(t)\Delta t + \Delta t^2 \sum_{i=1}^{k-1} \alpha_i \mathbf{f}(t + [1 - i]\Delta t), \\ \mathbf{v}\Delta t &= \mathbf{r}(t + \Delta t) - \mathbf{r}(t) + \Delta t^2 \sum_{i=1}^{k-1} \beta_i \mathbf{f}(t + [1 - i]\Delta t),\end{aligned}$$

for the particle positions and for the velocities, respectively, where \mathbf{f} is related to the force by $\mathbf{F} = m\mathbf{f}$. The coefficients α_i and β_i satisfy the equations:

$$\begin{aligned}\sum_{i=1}^{k-1} (1 - i)^q \alpha_i &= \frac{1}{(q + 1)(q + 2)}, \\ \sum_{i=1}^{k-1} (1 - i)^q \beta_i &= \frac{1}{q + 2}, \quad q = 0, \dots, k - 2.\end{aligned}$$

These predicted values are then corrected from the value of \mathbf{f} , obtained from the predicted values themselves as the gradient of the potential, at the time $t + \Delta t$, using the expressions:

$$\mathbf{r}(t + \Delta t) = \mathbf{r}(t) + \mathbf{v}(t)\Delta t + \Delta t^2 \sum_{i=1}^{k-1} \gamma_i \mathbf{f}(t + [2 - i]\Delta t),$$

$$\mathbf{v}\Delta t = \mathbf{r}(t + \Delta t) - \mathbf{r}(t) + \Delta t^2 \sum_{i=1}^{k-1} \delta_i \mathbf{f}(t + [2 - i]\Delta t),$$

where the coefficients γ_i and δ_i satisfy similar equations as α_i and β_i .

The predictor-corrector algorithm is computationally more expensive than the Verlet or leap-frog approach and it also requires more storage. This could be an important disadvantage in the case of large scale calculations. However, it gives the possibility to calculate velocities and positions with smaller error than Verlet-like algorithms. A detailed comparison between the Verlet and the Gear scheme can be found in Ref. [123].

2.4.2 Langevin Molecular Dynamics

The equations of motion in the Newton form preserve the mechanical energy. When the system of particles does not exchange energy with the environment, they describe correctly its evolution. When the system can exchange energy with the environment or different degrees of freedom are present, the equations of motion should be modified in order to get the correct dynamics. In the case that the evolution of the system is represented by the canonical distribution of probability, which means that the system is in thermal equilibrium with a heat bath, the motion of the particles is properly described by Langevin equations.

The Langevin equation is a stochastic differential equation in which two force terms are added to Newton's second law in order to approximate the effects of neglected degrees of freedom: one term represents a frictional force, proportional to the velocity, and the other one a random force. The friction removes kinetic energy from the system, while the random force adds kinetic energy to the system. To generate a canonical ensemble, the friction and random force have to obey the fluctuation-dissipation theorem.

In general a Langevin system arises from a classical system by removing degrees of freedom. The degrees of freedom which are removed exert conservative and frictional forces on the rest of the system. All other forces are assumed to add up to a random force. A typical example is a colloidal particle in a solvent. When only the degrees of freedom of the colloidal particle are considered, the system can be represented by Langevin dynamics. The frictional and random forces are caused by collisions of solvent molecules with the colloidal particle. A formal way of deriving Langevin dynamics is the projection operator formalism of Zwanzig [124] and Mori [125]. In this approach the phase space is divided into two parts, namely the 'interesting' and the 'uninteresting' degrees of freedom. For the approach to be useful, the uninteresting degrees of freedom should be rapidly varying with respect to the interesting ones. Mori introduced two projection operators, which project the whole phase space into the sets of interesting and uninteresting degrees of freedom, respectively. These projection operators are used to project the full equations of motion into the set of interesting degrees of freedom. The result is a differential equation with

three force terms: a mean force between the interesting degrees of freedom, a dissipative or frictional force exerted by the uninteresting degrees of freedom onto the interesting coordinates and a rest term which consists of forces which are neither correlated with the positions nor with the velocities. The frictional and uncorrelated force have the same memory function, the shape of which is given by the projection operator formalism. When the uncorrelated force is approximated by a random force the interesting degrees are independent of the uninteresting ones, which can be then neglected. While this method is formally correct, it is of no practical use, since it does not provide any criterion on how to choose the separation into interesting and uninteresting degrees of freedom.

The formal equations of motion for Langevin dynamics for a one-dimensional system is:

$$\begin{aligned} m dv &= -m\gamma v dt + f(r) dt + dW, \\ dr &= v dt, \end{aligned}$$

where γ is the friction constant and W is a stochastic process, known as Wiener process. It has the following properties:

1. $W(t)$ is normally distributed for $t \geq 0$;
2. $\langle W(t) \rangle = 0$ for $t \geq 0$;
3. $W(0) = 0$

By specifying the spread of the distribution of $W(t)$, the required ensemble can be generate, in particular with:

$$\langle W(t)W(t + \tau) \rangle = 2m\gamma k_B T \tau$$

the canonical ensemble is generated for the temperature T . The last expression is simply the formulation of the fluctuation-dissipation theorem in the canonical ensemble.

The differential form for the Langevin equations in Cartesian coordinates is:

$$m_i \frac{d^2 \mathbf{r}_i}{dt^2} = -m_i \sum_j \Gamma_{ij} \frac{d\mathbf{r}_j}{dt} + \mathbf{f}_i(\mathbf{r}_i) + \xi_i, \quad (2.23)$$

where the subscript i denotes the particle number, Γ_{ij} is a 3×3 friction matrix, $\mathbf{f}(\mathbf{r}) = -\nabla V(\mathbf{r})$ and ξ_i is a random force, often called noise. In most cases the friction matrix is diagonal and isotropic, which simplify the form of Eq. (2.23) to:

$$m_i \frac{d^2 \mathbf{r}_i}{dt^2} = -m_i \gamma_i \frac{d\mathbf{r}_i}{dt} + \mathbf{f}_i(\mathbf{r}_i) + \xi_i, \quad (2.24)$$

with γ_i the friction coefficient of the i -th particle.

Without memory of the history of the system, the noise is not correlated in time and gaussian distributed. The correlation is, thereby, given by:

$$\langle \xi_{ik}(t)\xi_{jl}(t+\tau) \rangle = 2m_i\gamma_i k_B T \delta_{ij} \delta_{kl} \delta(\tau), \quad (2.25)$$

where k and l indicate the Cartesian vector components, δ_{ij} is the Kronecker delta and $\delta(\tau)$ is the Dirac delta function.

The probability density $\rho(\mathbf{r}, \mathbf{p}, t)$ of trajectories generated by Eq. (2.24), also called the phase space density, obeys the Fokker-Planck equation:

$$\begin{aligned} \frac{\partial}{\partial t} \rho(\mathbf{r}, \mathbf{p}, t) + \sum_i \left(\frac{\mathbf{p}_i}{m_i} \cdot \nabla_{\mathbf{r}_i} \rho(\mathbf{r}, \mathbf{p}, t) + \mathbf{f}_i \cdot \nabla_{\mathbf{p}_i} \rho(\mathbf{r}, \mathbf{p}, t) \right) = \\ \sum_i \gamma_i \nabla_{\mathbf{p}_i} \cdot (\mathbf{p}_i \rho(\mathbf{r}, \mathbf{p}, t) + m_i k_B T \nabla_{\mathbf{p}_i} \rho(\mathbf{r}, \mathbf{p}, t)), \end{aligned}$$

It is possible to prove the complete equivalence of Langevin and Fokker-Planck equations [126].

To numerically integrate equation (2.24), we used in this work a modified leap-frog type algorithm. Several algorithm are proposed and compared in Ref. [127]. We will provide with more details in Chapter 6 where we studied specifically dynamical and transport properties by Langevin equations.

2.5 PERIODIC BOUNDARY CONDITIONS

A common feature of both Monte Carlo and Molecular Dynamics is the use of periodic boundary conditions. When one wants to simulate a real system, one has to deal with a number of particles which is of the order of the Avogadro number ($N \sim 10^{23}$). This is an impossible task even for the most powerful calculator. This problem arises as well, when the simulated system is by definition infinite.

The solution to this problem is to use periodic boundary conditions (PBC). When using PBC, particles are contained within a basic simulation box. This box is replicated to infinity by rigid translation in all the directions, completely filling the space. When a particle leaves one side of the cube, it is replaced by its 'image' particle coming from the opposite side. Other shapes than the simple cube are possible.

The key point is that in this way each particle is interacting not only with other particles in the simulation box, but also with their images in nearby boxes, i.e. interactions can 'go through' box boundaries. Provided the potential range is not too long, it is possible to adopt the 'minimum image convention', that each particle interacts with the nearest particles or images in the periodic array of replicas. This is shown in Fig. 2.1.

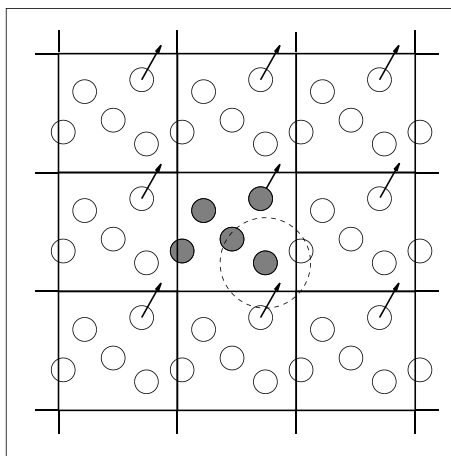


FIG. 2.1: Periodic boundary conditions. As a particle moves out of the simulation box, an image particle moves in to replace it. In calculating particle interactions within the cutoff range, both real and image neighbours are included.

Of course, it is important to bear in mind the imposed artificial periodicity when considering properties which are influenced by long-range correlations. Special attention must be paid to the cases where the potential range is not short: for example, charged and dipolar systems. In these cases the 'minimum image criterion' should be improved with other calculation methods, like, for instance, the Ewald summation technique [128].

When the inter-particle interaction potential is the screened Coulomb one, the number of replicas necessary to get good results is normally 1 or 2.

2.6 SHORT RANGE POTENTIALS: SMART CALCULATION TECHNIQUES

Computing the contributions to the interatomic forces in a Molecular Dynamics simulation or to the energy in a Monte Carlo simulation involves, in principle, a large number of calculations. If the interaction is pairwise, for each particle i , it is necessary to loop over all other particles j to calculate the minimum image separations r_{ij} .

When the interaction potentials are of short range, it is possible to assume that $V(r_{ij}) = 0$ if $r_{ij} > r_0$, with r_0 the potential cutoff. In this way, during the simulation it is no longer necessary to calculate all the interactions, but for every particle i only the interactions with particles contained in a sphere of

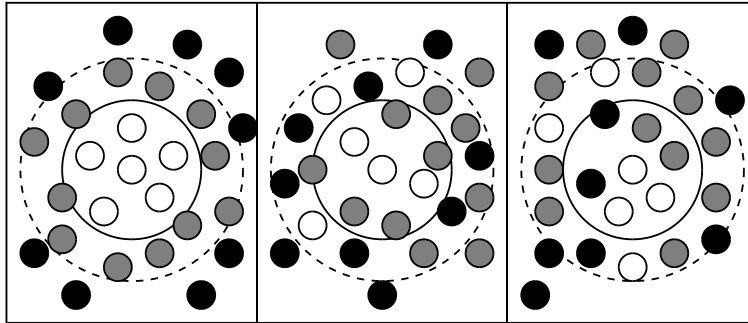


FIG. 2.2: The Verlet list on its construction at three different simulation steps. The potential cutoff range (solid circle), and the list range (dashed circle), are indicated. The list must be reconstructed before particles originally outside the list range (black) have penetrated the potential cutoff sphere

radius r_0 centered in the position of that particle should be taken into account. Nonetheless, the time to examine all pair separations is proportional to the number of distinct pairs, $N(N-1)/2$ in a N particle system, and for every pair one must compute at least r_{ij}^2 , which is still very demanding.

Verlet [121] suggested a technique with the use of lists of nearby pairs of particles for improving the speed of the simulation. The potential cutoff sphere, of radius r_0 , around a particular atom is surrounded by a 'skin', to give a larger sphere of radius r_{list} as shown in Fig. 2.2. At the first step in a simulation, a list is constructed of all the neighbors of each atom, for which the pair separation is within r_{list} . Over the next few simulation steps, only pairs appearing in the list are considered in the calculation of the interactions. From time to time the list is reconstructed: it is essential to do this before any unlisted pairs have crossed the shell between r_{list} and r_0 and come within interaction range. In this sense the skin is a warning system, which serves to signal the necessity to update the list. It is possible to trigger the list reconstruction automatically, if a record is kept of the distance traveled by each particle since the last update. The choice of list cutoff distance r_{list} is the result of a compromise: larger lists will need to be reconstructed less frequently, but will not give as much of a saving computational resources as smaller lists.

For extremely large systems another technique becomes preferable: the so called 'link-cell method'. The cubic simulation box (extension to non-cubic cases is possible) is divided into a regular lattice of cubic cells, as illustrated in Fig. 2.3. These cells are chosen so that the side of the cell is larger than the potential cutoff distance. Once a list of particles in each of those cells is created, it is a fast operation to search through the neighbors: it is simply necessary

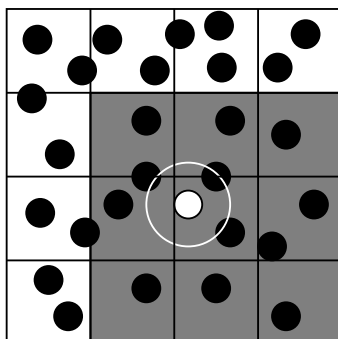


FIG. 2.3: The link-cell method. The potential cutoff r_0 range is indicated. In searching for neighbors of an atom, it is only necessary to examine the atom's own cell, and its nearest-neighbor cells (shaded)

to look at particle in the same cell as the particle of interest, and in nearest neighbor cells. The cell structure may be set up and used by the method of linked lists [129]. The first part of the method involves sorting all the particles into their appropriate cells. This sorting is rapid, and may be performed at every step. Then, within the routine which calculates the interactions, pointers are used to scan through the contents of cells, and calculate pair forces. This approach can be easily implemented for parallel calculations and results very efficient for large systems, like biomolecules.

3

Ground state configuration: the chain-like system

Recently there has been a great deal of interest in mesoscopic systems consisting of interacting particles in low dimensions or confined geometries. A class of quantum anisotropic systems exhibiting 'stripe' behavior appears in the quantum Hall effect [130], in manganite oxides and high- T_c superconductors [131] where electronic strong correlations are responsible for the formation of these inhomogeneous phases. Another class of confined Q1D geometries appears in many diverse fields of research and some typical and important examples from the experimental point of view are: electrons on liquid helium [33, 132], microfluidic devices [133], colloidal suspensions [134] and confined dusty plasma [11], as already discussed in Chapter 1.

A major phenomenon which is expected to occur in charged particles interacting via a Coulomb or screened Coulomb potential is Wigner crystallization (WC) at low enough temperatures and densities, when the potential energy overwhelms the kinetic energy. Indeed, evidence of such a type of transition was found very recently [33] in experiments on electrons on the surface of liquid helium where the electrons were confined by metallic gates and exhibited dynamical ordering in the form of filaments (see Chapter 1, Sec. 1.3.1). This particular experiment posed many interesting questions regarding the nature of the transition to WC, its density dependence and the melting. Furthermore, the considered system has been proposed as a possible step towards the realization of a quantum computer with electrons floating on liquid helium [34].

In this chapter, as a first step towards the understanding of the behavior of these systems, we start with a 2D system consisting of an infinite number of charged particles and we impose a parabolic confining potential in one direction, which makes that system Q1D. The particles interact with a Yukawa-type potential where the screening length is an external parameter. Physically, it is the natural interaction encountered in colloidal suspensions or complex plasmas, as already seen in Chapter 1, or in the case of electrons on liquid helium the Coulomb interaction can be adjusted to result into a Yukawa interaction by using a system of electrodes. The confining parabolic potential is equivalent to a positive neutralizing charge background or it is the result of electromagnetic fields that confine the particles, e.g. the gate voltage for the electrons on liquid helium or the interfering lasers for the colloids.

The combination of the interaction among particles and the external potential leads to a rich structural phase diagram as a function of the screening length λ and the density n of the system. We varied the screening from a very small to a very large value, in order to investigate interactions ranging from the pure Coulomb to the nearly free particle. We will show that the structural units at temperature $T = 0K$ are parallel chains of particles, the number of which depends on the values of λ and n . The transition from one configuration to the other can be obtained via a first or a second order transition.

According to the Mermin-Wagner theorem [135] there is no true long-range crystalline order in two dimensions. However, this theorem is only strictly valid when the potential falls off faster than $1/r$ and in the thermodynamic limit. When the same arguments of the theorem are applied to a large but finite system, no inconsistencies arise from the assumption of crystalline order. Thus any system that can be studied in laboratory or in computer simulations can exhibit crystalline order [3]. On the other hand short-range order is expected to form even in the thermodynamic limit for infinite systems. Therefore we can assume that the system we are investigating is in a well defined ordered phase at zero temperature.

We deal with a classical model of Wigner crystal, which is naturally appropriate for colloids and complex plasma and which is suitable even for electrons on liquid helium at low temperature and low density. In that case, in fact, the De Broglie thermal length for the electrons is small compared to the electron spacing so that the electrons can be considered as localized and, therefore, they can be treated as classical particles, neglecting their intrinsic fermionic nature. The WC in strictly one dimension and in the quantum regime was first studied by Schultz [137]. He found that for arbitrarily weak Coulomb interaction the density correlations at wave vector $4k_F$ decay extremely slowly (the most slowly decay term is $\propto \exp(-c\sqrt{\ln x})$).

The chapter is organized as follows. First, we present the model and the methods used, then we study the zero temperature phase diagram and the properties of the structural transitions. They will be the starting point for

the discussion on normal modes and melting presented in Chapter 4 and 5, respectively.

3.1 MODEL AND METHODS

The system is modeled by an infinite number of classical charged particles with identical charge q , moving in a plane with coordinates $\mathbf{r} = (x, y)$. The particles interact through a Yukawa potential and an additional parabolic potential confines the particle motion in the y -direction. The Hamiltonian of the system is given by:

$$H = \frac{q^2}{\varepsilon} \sum_{i \neq j} \frac{\exp(-|\mathbf{r}_i - \mathbf{r}_j|/\lambda)}{|\mathbf{r}_i - \mathbf{r}_j|} + \sum_i \frac{1}{2} m \omega_0^2 y_i^2 \quad (3.1)$$

where m is the mass of each particle, ε is the dielectric constant of the medium particles are moving in, ω_0 measures the strength of the confining potential. The Hamiltonian can be rewritten in a dimensionless form by rescaling it according to Eqs. (2.8a) and (2.8b). Then it takes the form

$$H' = \sum_{i \neq j} \frac{\exp(-\kappa|\mathbf{r}'_i - \mathbf{r}'_j|)}{|\mathbf{r}'_i - \mathbf{r}'_j|} + \sum_i y_i^2, \quad (3.2)$$

where $H' = H/E_0$, $\kappa = r_0/\lambda$ and $\mathbf{r}' = \mathbf{r}/r_0$. This transformation is particularly interesting because now the Hamiltonian no longer depends on the specifics of the system and becomes only a function of the density and the dimensionless inverse screening length, as already claimed in Chapter 2. It is possible to define a dimensionless temperature as $T' = T/T_0$ with $T_0 = (m\omega_0^2 q^4 / 2\varepsilon^2)^{1/3} k_B^{-1}$.

For the calculations of the ground state energy we used a combination of analytical calculations and Monte Carlo simulations with the standard Metropolis algorithm. We used a slight different rejection criterion than the one indicated in Sec. (2.3.1): if the new configuration has a larger energy the displacements are accepted with probability $\delta < \exp(-\Delta E/T)$, where δ is a random number between 0 and 1 and ΔE is the increment in the energy. It, actually, provides a faster sampling of the configurational space for the system under investigation. We have allowed the system to approach its equilibrium state at some temperature T , after executing $10^5 \div 10^6$ Monte Carlo steps. We have used the technique of simulated annealing to reach the $T = 0$ equilibrium configuration: first the system has been heated up and then cooled down to a very low temperature. In the simulations typically 300 particles were used. The simulation cell length L was variable and it was related to the number of particles N , to the number of row l and to the inter-particle spacing within the same row a by $L/r_0 = (N/l)(a/r_0)$. In order to simulate an infinitely long system periodical boundary conditions (Born-Von Karman) were introduced.

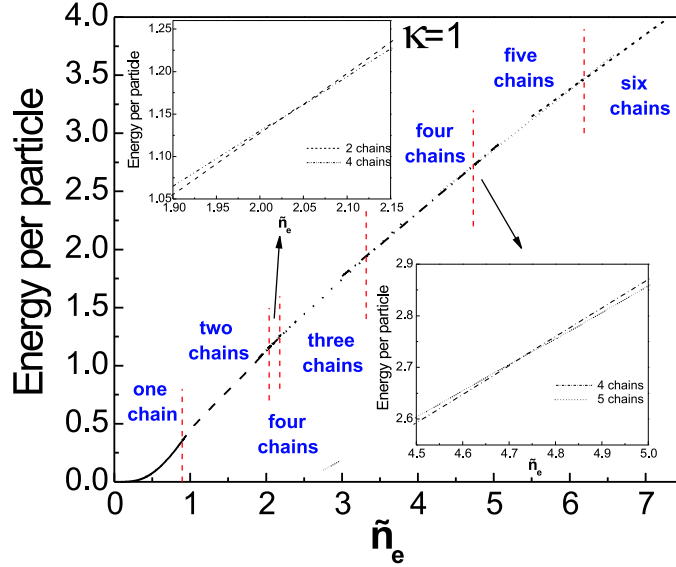


FIG. 3.1: The energy per particle as a function of density for $\kappa=1$.

3.2 GROUND STATE CONFIGURATIONS

The charged particles crystallize in a certain number of chains. Each chain has the same density resulting in a total one-dimensional density \tilde{n}_e . It is then possible to calculate the energy per particle for each configuration and to check the favored one as a function of the parameters of the system. If a is the separation between two adjacent particles in the same chain, we can define the dimensionless linear density $\tilde{n}_e = lr_0/a$, where l is the number of chains.

In the case of multiple chains, in order to have a better packing (or in other words to minimize the interaction energy by maximizing the separation among particles in different chains), the chains are staggered with respect to each other by $a/2$ in the x -direction. In an infinite lattice this will lead to the hexagonal WC [128]. We calculated the energy per particle as a function of the density for the first six possible configurations of the system.

If the particles crystallize in a single chain, the minimum energy is obtained when the particles are placed on the x axis, where the confining potential is zero. In this case the linear density is $\tilde{n}_e = r_0/a$ and the x coordinate of the particles are $x_i = ia$, with $i = 0, \pm 1, \pm 2, \dots, \pm \infty$. The energy per particle is:

$$E_1 = \tilde{n}_e \sum_{j=1}^{\infty} \frac{1}{j} \exp(-\kappa j / \tilde{n}_e). \quad (3.3)$$

The case of Coulomb interaction, $\kappa \rightarrow 0$, is treated using the Ewald summation method so that the summation over long distance can be done effectively. Following the standard procedure [128] we obtain for E_1 :

$$E_1(\kappa = 0) = \frac{\tilde{n}_e^2}{\sqrt{\pi}} \lim_{x \rightarrow 0} \left[\sum_j 2 \exp(-2\pi j x) \Phi_1(j\pi/2\tilde{n}_e) + \sum_{j \neq 0} \Phi_2(\tilde{n}_e^2(x-j)^2) + \frac{1}{\tilde{n}_e} \Phi_2(\tilde{n}_e^2 x^2) - \frac{\sqrt{\pi}}{\tilde{n}_e^2} \frac{1}{x} \right], \quad (3.4)$$

where:

$$\begin{aligned} \Phi_1(x) &= \sqrt{\pi} \int_x^{\infty} dt \frac{\exp(-t^2)}{t}, \\ \Phi_2(x) &= \sqrt{\frac{\pi}{x}} \left(1 - \frac{2}{\sqrt{\pi}} \int_0^{\sqrt{x}} e^{-t^2} dt \right). \end{aligned}$$

The first summation contains a divergent term at $j = 0$ coming from the lower limit of the integration in the function $\Phi_1(x = 0)$. This divergence is remedied if we subtract the interaction energy E_b of the negatively charged particles with the positive background which also diverges logarithmically in one dimension. By that we get:

$$\begin{aligned} \Delta E_1 = E_1(\kappa = 0) - E_b &= \frac{\tilde{n}_e^2}{\sqrt{\pi}} \left[\sum_{j \neq 0} 2 \Phi_1(j\pi/2\tilde{n}_e) + \sum_{j \neq 0} \Phi_2(\tilde{n}_e^2 j^2) \right] - \frac{2}{\sqrt{\pi}} \tilde{n}_e. \end{aligned} \quad (3.5)$$

In the two-chain configuration the particles crystallize in two parallel lines separated by a distance d and displaced by a distance $a/2$ along the x -axis. The energy per particle in this case is:

$$E_2 = \frac{c^2}{\tilde{n}_e^2} + \frac{\tilde{n}_e}{2} \sum_{j=1}^{\infty} \frac{\exp(-2\kappa j / \tilde{n}_e)}{j} + \frac{\tilde{n}_e}{2} \sum_{j=1}^{\infty} \frac{\exp(-2\kappa \sqrt{(j-1/2)^2 + c^2} / \tilde{n}_e)}{\sqrt{(j-1/2)^2 + c^2}}, \quad (3.6)$$

where $\tilde{n}_e = 2r_0/a$ and $c = d/a$. The first term in Eq. (3.6) is the potential energy due to the confining potential, the second term is the energy due to

the intra-chain interaction and the last term represents the inter-chain interactions. Minimizing E_2 with respect to the separation between the chains, c , we obtained the ground state energy for the two-chain configuration. Similar straightforward but tedious calculations were done for the other multi-chain structures. By symmetry there is one intra-chain distance in the three-chain structure, two in the four- and five-chain structures and three in the six-chain structure. The corresponding expressions for the energy are relegated, for completeness, to the Appendix.

Calculating the energy minimum for each configuration for different values of \tilde{n}_e at fixed κ , we obtain the energy per particle E . In Fig. 3.1 we show E as a function of the density \tilde{n}_e for $\kappa = 1$. Notice that for certain density ranges more than one configuration can be stable (this is made more clear in the insets of Fig. 3.1 for \tilde{n}_e around 2 and 4.7). In the low density limit the energy per particle is given by the first term of Eq. (3.3): $E = \tilde{n}_e \exp(-\kappa/\tilde{n}_e)$, while the rest of the curve can be fitted to $E = -0.0194\tilde{n}_e^2 + 0.720\tilde{n}_e - 0.245$ with an error less than 2.3%.

Calculating the energy minima for different \tilde{n}_e and different κ we obtain the zero temperature phase diagram of Fig. 3.2. For $\kappa = 0$ we recover the Coulomb limit. We found that the energy obtained by the analytical method is in excellent agreement with the one obtained by our Monte Carlo simulations, with a difference between them less than 0.3%.

We observe the following sequence of transitions as the density increases: from one to the two-chain structure then to the four-chain configuration, back to the three-chain and again to four and then to five, six, etc. Notice the remarkable fact that between the 2 and 3 chain configuration there is a small intermediate region where a four-chain configuration has a lower energy. For all other transitions the number of chains increases only by one unit, i.e. $n \rightarrow n+1$. The relative lateral position of the different chains are depicted in Fig. 3.3 as a function of the density \tilde{n}_e . In the case of two and three-chain the inter-chain distance increases as the density increases. This is also true for the four-chain configuration, with some differences. In the first four-chain regime of the phase diagram, the distance between the two internal chains is larger than the distance between the internal chains and the external ones, in the second regime the behavior of the system is the opposite with the distance between internal and external chains larger than the one between internal chains. For the other structures the inter-chain distance is always a growing function of the density. It is evident that only the first transition is continuous with a clear bifurcation.

In order to gain some insight on the distribution of the energy in this anisotropic system we investigated (see Fig. 3.4) the energy per particle for each chain. This was computed by considering a particle at a particular chain and taking into account all the interactions with the rest of the particles. The cases of interest are the configurations for which it is possible to distinguish internal from external chains and may be related to the difference in the melting

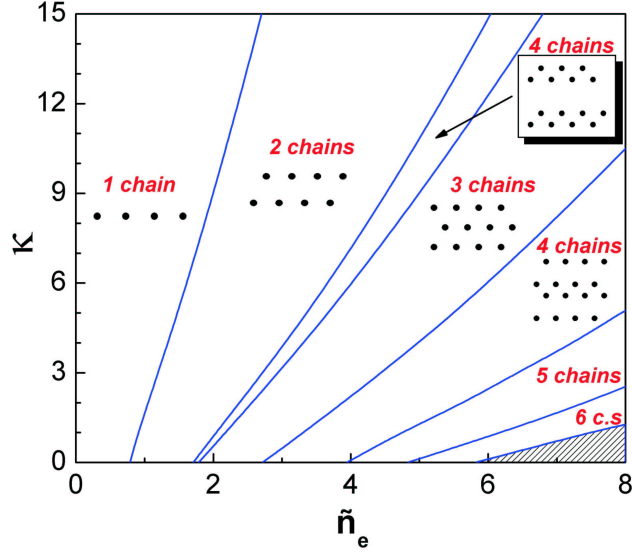


FIG. 3.2: The zero temperature structural phase diagram.

behavior which is discussed in Chapter 5. The interesting observation is that in every case the energy per particle is larger in the external chain than the internal ones. This asymmetry reflects the fact that for each particle residing in an external chain the gain in energy due to the confining potential is higher than the difference in the Coulomb energy due to the lack of symmetric neighboring chains, as compared to a particle residing in an internal chain. E.g. for a three-chain system where the middle chain is the 0th and the external ones are denoted by +1 and -1, we have for the energy of two particles:

$$E_{\pm 1} - E_0 = E_{conf,\pm 1} + E_{Coulomb,+1,-1} - E_{Coulomb,\pm 1,0} > 0, \quad (3.7)$$

where $E_{Coulomb,\alpha,\beta}$ denotes the Coulomb energy of a particle residing in chain α interacting with the particles in chain β and $E_{conf,\alpha}$ denotes its confining energy.

In the case of the first density regimes where the four-chain structure is optimal this difference is not large due to the fact that the internal distance is less than the external. On the contrary, the difference is much larger in the second regime of the four-chain structure. Another interesting observation is that as we approach the limit of Coulomb interactions ($\kappa \ll 1$) the energy difference tends to vanish and the system behaves isotropically.

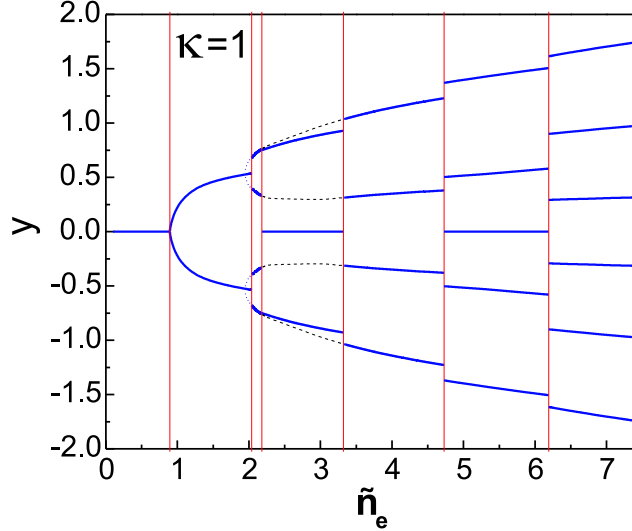


FIG. 3.3: The lateral position of the chains in the Wigner crystal state as a function of the linear density for $\kappa = 1$.

3.3 STRUCTURAL TRANSITIONS

We have seen that by increasing the density, the system changes its configuration, in other words it undergoes a *structural transition*. It is a natural question to study the order of these transitions. For this purpose the derivative of the energy with respect to the density was calculated, which is shown in Fig. 3.5 for the case of $\kappa = 1$. Only the transition between the one and the two-chain configuration is continuous and all the others are discontinuous. This conclusion agrees with the results of Fig. 3.3, where discontinuous changes of the lateral position of the particles correspond to first order transitions. The transition $1 \rightarrow 2$ is a “zig-zag” transition [147] (see Fig. 3.6(a)). The transition $2 \rightarrow 4$ occurs through a “zig-zag” transition of each of the two chains accompanied by a shift of $a/4$ along the chain, which makes it a weakly discontinuous transition (see Fig. 3.6(b)). In principle, these kind of almost zig-zag transitions are possible for three-, four-, five- and six- chains to result into six-, eight-, ten- and twelve-chain structures, respectively. Actually, these were observed during the numerical simulations, especially for very small value of κ , but they represent metastable states and are not the most energetically favored configurations.

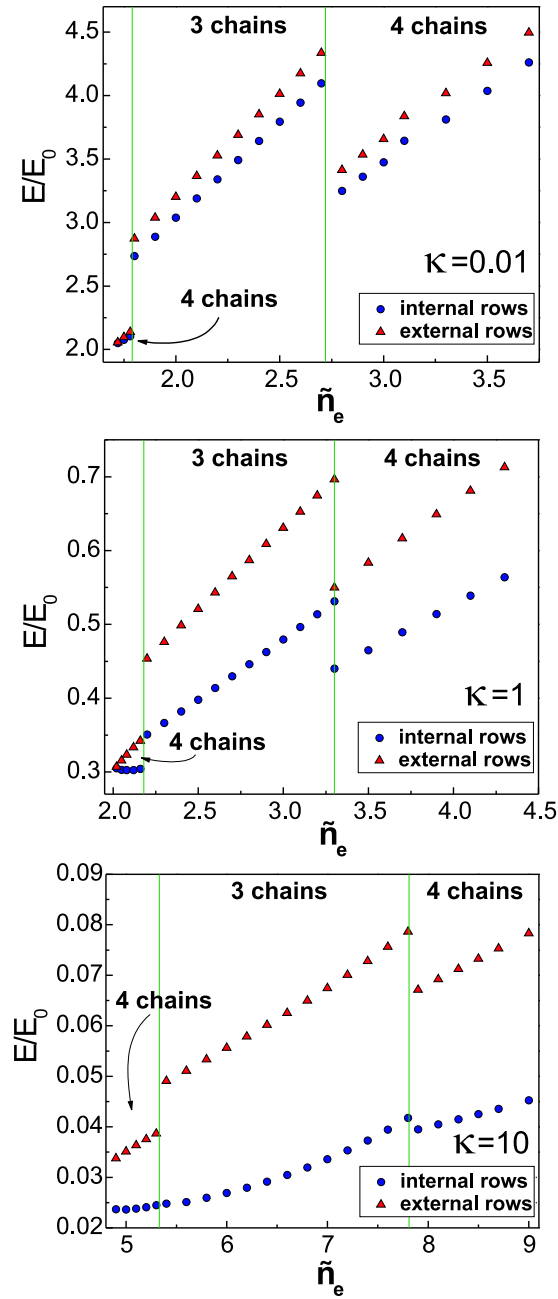


FIG. 3.4: The energy per chain at $T=0$ and (a) $\kappa = 0.01$, (b) $\kappa = 1$ and (c) $\kappa = 10$. The energy is always higher for the external chains but as the Coulomb limit ($\kappa \ll 1$) is approached the difference is diminished and the system behaves isotropically.

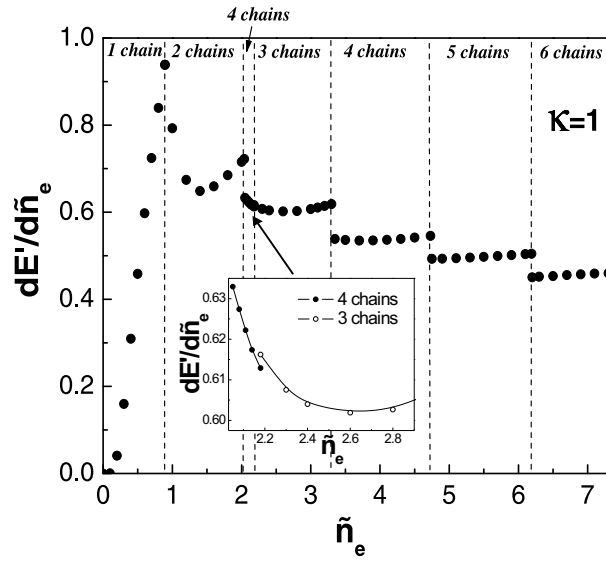
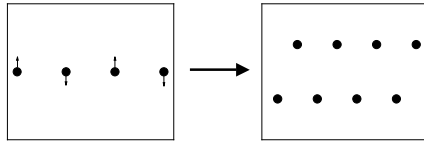


FIG. 3.5: The derivative of the energy with respect to the density for $\kappa = 1$. Only the transition from one to two-wires is continuous (second order) the rest are first order.

Mechanism of some structural transitions

(a) 1→2 *zig-zag*



(b) 2→4 *zig-zag + shift*

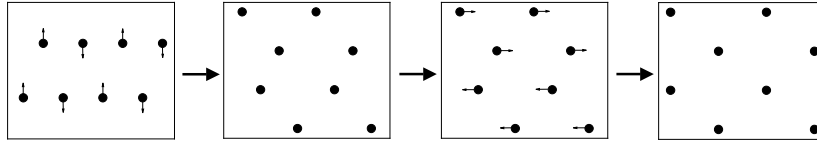


FIG. 3.6: The mechanism of the structural transitions 1 → 2 chains and 2 → 4 chains.

3.4 LIMIT OF SHORT RANGE INTERACTION AND LARGE DENSITY

In order to make the connection with the regime where the hard core potential can be used as a working hypothesis, we investigate the limit $\lambda \ll a$. It can be shown that the variation of the distances between chains can be neglected and in the limit where $m\omega_0^2 W^2 \ll q^2/(a\varepsilon)$ (W is the width of the strip), following the spirit of the hydrodynamic consideration of Koulakov and Shklovskii [148], the difference in the distance between chains at the borders $d(\pm W/2)$ and at the center $d(0)$ follows the relation:

$$\delta d_0 = d_0(W/2) - d_0(0) \approx \lambda \ln l, \quad (3.8)$$

where l is the number of chains and $d_0 = \sqrt{d^2 + a^2/4}$.

This can be estimated by considering the pressure σ_{yy} in the crystal exercised by the external potential. Adopting a method similar to Ref. [148, 149]:

$$\sigma_{yy} = -S(\sigma) \frac{m\omega_0^2}{2} \left(\frac{W^2}{4} - y^2 \right), \quad (3.9)$$

where $3/4 \leq S(\sigma) \leq 1$ and σ is the Poisson ratio. We assume a uniform density n and $S(\sigma) \approx 1$. Then, balancing the force by the pressure and the interaction forces we get (in this estimate we keep the dimensions for clarity):

$$\frac{2dq^2}{\varepsilon(d^2 + a^2/4)} \exp(-\sqrt{d^2 + a^2/4}/\lambda) \sim \frac{ndm\omega_0^2}{2} \left(\frac{W^2}{4} - y^2 \right), \quad (3.10)$$

from this relation:

$$d_0(y) \equiv \sqrt{d(y)^2 + a^2/4} \approx \lambda \ln \left[\frac{4q^2}{\varepsilon m\omega_0^2 n (W^2/4 - y^2) (d(y)^2 + a^2/4)} \right], \quad (3.11)$$

subtracting the values of d_0 at $W - a/2$ and 0 we obtain Eq. (3.6). Therefore in the case of very short-range interaction $\delta d \ll d(0)$. Then one can adopt the hard core potential and essentially the total energy becomes the sum of the energy of each particle due to the confining potential. The average energy per unit length E/L then reads:

$$\frac{E}{L} \approx \frac{1}{24} m\omega_0^2 \frac{W^2}{la}. \quad (3.12)$$

3.5 CONCLUSIONS

The ground state configuration and the structural phase transitions for a chain-like system can be studied experimentally using parabolically confined colloidal particles or dusty plasmas in the case of a screened Coulomb inter-particle interaction. Another important experimental system are electrons floating on

liquid helium, where it is possible to achieve relatively narrow Q1D channels on very stable suspended helium films over structured substrates. We provided a model for these systems and studied the ground-state configurations. The chain-like structures arise from the competing effects between electrostatic repulsion and confinement. For low densities the particles crystallize in a single chain; with increasing density a zig-zag (continuous) transition occurs and the single chain splits into two chains. Further increasing the density we found the remarkable behavior that the four-chain structure is stabilized before the three-chain structure. The $2 \rightarrow 4$ chain transition occurs through a zig-zag transition of each of the chains accompanied by a shift of $a/4$ along x . This first 4 chain configuration has a relatively small stability range after which the system transits to a three chain configuration. For higher values of the density, the four chain configuration attains again the lowest energy. Then a further increase of \tilde{n}_e will lead to more chains, that is 5, 6 and so on. The structural transitions are all discontinuous (i.e. first order), except the $1 \rightarrow 2$ transition. The chain system is intrinsically anisotropic, because of the confinement acting only in one direction. This reflects into the fact that (i) inter-chain and intra-chain distances are different and (ii) the distances between two neighbor chains is not homogeneous along the y -direction in the multi-chain configurations ($n \geq 4$). When the number of chain is extremely large the structures are more isotropic. In the limit of small κ , i.e. in the Coulomb limit, a more homogenous system of chains is also obtained. Evidence for the single chain formation and the zig-zag transition has been found in experiments, as discussed in Chapter 1.

Publications. The result presented in this chapter were published as:

- G. Piacente, I.V. Schweigert, J.J. Betouras, and F.M. Peeters, *Structural properties and melting of a low dimensional classical Wigner crystal*, Physica E **22**, 779 (2004) (4 pages).
- G. Piacente, I.V. Schweigert, J.J. Betouras, and F.M. Peeters, *Generic properties of a quasi-one-dimensional classical Wigner lattice*, Phys. Rev. B **69**, 045324 (2004) (17 pages).
- G. Piacente, I.V. Schweigert, J.J. Betouras, and F.M. Peeters, *Generic properties of a quasi-one-dimensional classical Wigner lattice*, Virtual Journal of Nanoscale Science and Technology, Vol. **9** (February 23, 2004).
- G. Piacente, I. V. Schweigert, J. J. Betouras, and F. M. Peeters, *Structural properties and melting of a quasi-one-dimensional classical Wigner crystal*, Solid State Commun. **128**, 57 (2003) (5 pages).

4

Normal modes

Once the equilibrium configuration for a system of interacting particles is known, the following step is to study the small oscillations of the particles around their equilibrium positions, i.e. the normal modes. In the present chapter we study thoroughly the normal modes of the classical Q1D multi-chain system introduced in Chapter 3. In particular, we compare the theoretical results with experimental findings. A Q1D chain-like system was recently realized experimentally in a complex plasma by giving a proper shape to the electrodes [51, 66, 67], as shown in Chapter 1 (Sec. 1.2.3). Following the standard harmonic approximation [139] and exploiting the translational invariance of the chains along the x -direction, the dispersion curves are calculated. There are optical and acoustical branches and their number is equal to the number of chains. The acoustical modes correspond to motion along the unconfined direction and the optical ones to motion along the confined direction. We also study the collective excitations in the presence of a constant magnetic field perpendicular to the plane of the system. These modes (magnetophonons), can be directly detected experimentally [140, 141]. In order to make quantitative comparison with the experiments we investigate the dispersion curves in the presence of friction (the ion gas drag for the plasma crystal) and external driving forces (laser beams in the case of the experiment of Ref. [51]). Therefore, we consider: (i) the uniformly damped motion of a normal mode, and (ii) the damped propagation of a local forced oscillation of a single particle.

Experimentally the studies focused on a single chain structure. We investigate carefully this configuration and show that the model we propose provides results which are in excellent agreement with the experiment. Furthermore, we make predictions for multi-chain configurations.

4.1 NATURAL MODES

The collective motions of particles can be treated as consisting of modes, or phonons, which in an experiment can arise from two different ways. First, phonons naturally exist in a lattice that has a finite temperature, driven by spontaneous fluctuations. These motions can be decomposed as harmonic-oscillator-like modes, which we term natural phonons. We use the term 'natural' to distinguish phonons that are present naturally from those that are deliberately excited by external manipulation. Natural phonons correspond to random particle motion, i.e. they correspond to thermal motion. Because chain-like systems realized in complex plasmas are not in thermal equilibrium, we avoid calling the phonons 'thermal' and instead use the more general term 'natural'. Second, phonons can be excited in experiments by manipulations using external forces. Several experiments have been reported with *in situ* measurements of externally excited modes in 1D [51] and 2D [50, 62] dusty plasma crystals. In these experiments, phonons were continually stimulated at a specific frequency, making up a wave that propagated away from the excitation location. This wave has the same frequency as the excitation. Due to damping, the wave amplitude decays as it propagates.

In order to investigate the general properties of natural modes we proceed gradually, first studying the ideal situation where no dissipation is present both in the absence and in the presence of an external magnetic field and, then, considering the effect of friction in both cases.

4.1.1 Natural modes in the absence of friction and in the absence of an external magnetic field

Within the standard harmonic approximation [139], which consists in expanding the inter-particle potential function about the equilibrium (minimum energy) configuration up to second order in the displacements, and by mean of the translational invariance of the system along the x -direction, the eigenmodes of a chain-like system modeled by the Hamiltonian (3.2) are found by solving the system of equations:

$$[(\omega^2 - \delta_{\beta,y})\delta_{\alpha\beta,ij} - D_{\alpha\beta,ij}]Q_{\beta,j} = 0, \quad (4.1)$$

where $Q_{\beta,j}$ is the displacement of the particle j from its equilibrium position in the β direction, $(\alpha, \beta) \equiv (x, y)$, $\delta_{\beta,y}$ and $\delta_{\alpha\beta,ij}$ are unit matrices and $D_{\alpha\beta,ij}$ is the dynamical matrix defined by:

$$D_{\alpha\beta,ij} = \frac{1}{m} \sum_{\nu} \phi_{\alpha,\beta}(\nu) e^{-i\nu ka} \quad (4.2)$$

where ν is an integer assigned to each unit cell, k the wavenumber and a the inter-particle spacing along the same chain. The force constants $\phi_{\alpha,\beta}(\nu)$ in the specific case of Yakawa interaction are given by:

$$\phi_{\alpha,\beta}(\nu) = \partial_{\alpha} \partial_{\beta} \frac{\exp(-\kappa \sqrt{(x-x')^2 + (y-y')^2})}{\sqrt{(x-x')^2 + (y-y')^2}}, \quad \nu \neq 0, \quad (4.3)$$

evaluated at $x - x' \in \{a\nu, a(\nu + 1/2)\}$, $y - y' =$ relevant inter-chain distance, and

$$\phi_{\alpha,\beta}(\nu = 0) = - \sum_{\nu \neq 0} \phi_{\alpha,\beta}(\nu). \quad (4.4)$$

The term $\delta_{\beta,y}$ in Eq. (4.1) takes into account the effect of the confining potential. All the frequencies are measured in unit of the frequency ω_0 of the external confining potential.

If one starts from the equations of motion and look for solution in the form of plain waves: $(x'_n, y'_n) \propto \exp[i(kna - \omega t)]$, it gives in turn the system of algebraic homogeneous equations (4.1), whose determinant of coefficients has to be zero in order to obtain non trivial solutions, $Q_{\beta,j} \neq 0$. The eigenfrequencies are obtained from this condition. Studying the eigenvectors of the dynamical matrix it is easy to recognize that the optical modes are identified with the motion in the direction of confinement (y -direction) while the acoustical modes are identified with the motion in the unconfined x direction.

The result for one, two and three chain structure are illustrated in Fig. 4.1: the dispersion curves (I) and the relative oscillatory motions (II) are represented, respectively.

In general, the number of modes is the total number of degrees of freedom of the system minus the number of degrees of freedom that correspond to pure rigid body motion (rotation or translation). Each mode is defined by an eigenvector and its corresponding eigenfrequency. In a crystal the normal modes groups into both acoustical and optical branches, the number of which is related to the atomic species in unit cell. In a Q1D chain-like system, the number of chains determines the number of particles in each unit cell and therefore the number of degrees of freedom per unit cell. So if l is the number of chains there will be $2l$ branches for the normal mode dispersion curves. In our chain-like system, as it is evident from Fig. 4.1, there are l acoustical branches as well as l optical ones. For ordinary 2D crystals there are 2 acoustical

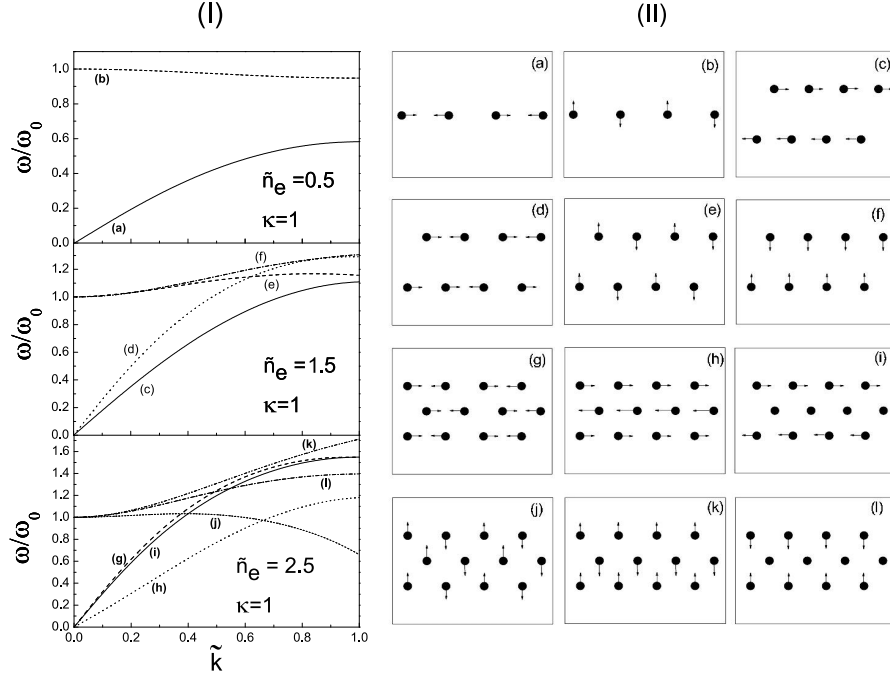


FIG. 4.1: (I) The normal modes of the system in the one (a), two (b) and three (c) chain configuration. The optical and acoustical branches correspond to motion in the confined and unconfined direction respectively. The wavelength is in units of π/a , where a is the length of the unit cell. (II) The motion of the particles for the one-, two- and three- chain structure which corresponds to the different eigenfrequencies.

branches and $2r - 2$ optical branches, if r is the number of atomic species in the unit cell [165]. It is worth to stress that for the one chain structure the unit cell consists of a single particle, i.e. $r = 1$, and therefore one expects only a single acoustical branch and no optical branch. The appearance of the optical branch is a consequence of the fact that the system is not strictly 1D but Q1D and that a confining potential in the y -direction is present.

Solving explicitly Eq. (4.1) for the single chain configuration we obtain that the acoustical and optical eigenfrequencies are given respectively by:

$$\omega_{ac}(k) = \left\{ \tilde{n}_e^3 \sum_{j=1}^{\infty} \frac{\exp(-j\kappa/\tilde{n}_e)}{j^3} \left(2 + \frac{2j\kappa}{\tilde{n}_e} + \frac{j^2\kappa^2}{\tilde{n}_e^2} \right) [1 - \cos(ka_j)] \right\}^{1/2} \quad (4.5a)$$

$$\omega_{opt}(k) = \left\{ 1 - \tilde{n}_e^3 \sum_{j=1}^{\infty} \frac{\exp(-j\kappa/\tilde{n}_e)}{j^3} \left(1 + \frac{j\kappa}{\tilde{n}_e} \right) [1 - \cos(ka_j)] \right\}^{1/2} \quad (4.5b)$$

where k is the wave number. Note that for $k \rightarrow 0$, $\omega_{opt} \approx \omega_0$, which corresponds to the center of mass motion of the system in the confining potential. This is true also for the optical branches in the two and three chain configuration, as it is clearly shown in Fig 4.1(I).

In the limit of small wavenumbers k , the summations in Eqs. (4.5a) and (4.5b) can be done analytically and we obtain:

$$\omega_{ac}(k) = \left[-\ln(1 - e^{-\kappa/\tilde{n}_e}) + \frac{\kappa}{\tilde{n}_e} \frac{e^{-\kappa/\tilde{n}_e}}{1 - e^{-\kappa/\tilde{n}_e}} + \frac{\kappa^2}{2\tilde{n}_e^2} \frac{e^{-\kappa/\tilde{n}_e}}{(1 - e^{-\kappa/\tilde{n}_e})^2} \right]^{1/2} \tilde{n}_e^{3/2} |k| a, \quad (4.6a)$$

$$\omega_{opt}(k) = \left\{ 1 - \left[-\ln(1 - e^{-\kappa/\tilde{n}_e}) + \frac{\kappa}{\tilde{n}_e} \frac{e^{-\kappa/\tilde{n}_e}}{1 - e^{-\kappa/\tilde{n}_e}} \right] \tilde{n}_e^3 k^2 a^2 \right\}^{1/2}, \quad (4.6b)$$

which gives explicitly the dependence of the modes on the density and the screening parameter. In the limit $\kappa/\tilde{n}_e \gg 1$:

$$\omega_{ac}(k) = e^{-\kappa/\tilde{n}_e} \frac{\kappa^2}{2\sqrt{\tilde{n}_e}} |k| a, \quad (4.7a)$$

$$\omega_{opt}(k) = 1 - e^{-\kappa/\tilde{n}_e} \frac{\tilde{n}_e^2}{2\kappa} k^2 a^2, \quad (4.7b)$$

while in the opposite limit $\kappa/\tilde{n}_e \ll 1$:

$$\omega_{ac}(k) = \left[\frac{3}{2} + \ln \left(\frac{\tilde{n}_e}{\kappa} \right) \right]^{1/2} \tilde{n}_e^{3/2} |k| a, \quad (4.8a)$$

$$\omega_{opt}(k) = \left\{ 1 - \left[1 + \ln \left(\frac{\tilde{n}_e}{\kappa} \right) \right] \tilde{n}_e^3 k^2 a^2 \right\}^{1/2}. \quad (4.8b)$$

It is interesting to notice that for the acoustical branches the dispersion is positive, that is phase and group velocity have the same sign. There is a remarkable difference in the optical branch of the spectrum between the single chain and the two and three-chain structures. In the first case the frequency of the optical branch decreases as the wavenumber k increases, i.e. the dispersion is negative (the group velocity is negative), while for the two and three-chain structures the optical frequency increases. Physically the negative dispersion

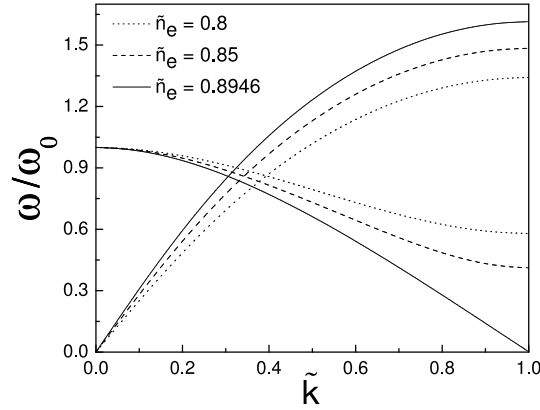


FIG. 4.2: The phonon spectrum at the softening of the optical mode at the structural transition from one to two-chains.

for the single chain optical branch can be understood considering that the electrostatic repulsion acts oppositely to the force of the confining potential (see e.g. Fig. 4.1(II-b)) and this reduces the oscillation frequency with increasing k . Another notable feature is the softening of the optical branch, accompanied by a hardening of the acoustical one at the values of \tilde{n}_e and κ where the $1 \rightarrow 2$ chain structural transition is observed (see Fig. 4.2), which confirms that $1 \rightarrow 2$ chain transition, discussed in the previous chapter, is a continuous one.

4.1.2 Natural modes in the absence of friction and in the presence of an external magnetic field

We now consider the effect of applying a constant magnetic field B in the perpendicular direction to the plane the particles are moving in, i.e. z -direction. For quantum particles, the magnetic field can localize the charged particles into cyclotron orbits, therefore aiding the formation of a Wigner crystal. It is known [150] that in a classical system an external magnetic field does not alter the statistical properties of the system and consequently the structural properties and the melting temperature are insensitive to the magnetic field strength. But on the other hand the character of motion of the particles is altered significantly because the magnetic field couple the x and y motion. When the cyclotron frequency is larger than the eigenfrequencies of the system, the dispersion curves are significantly altered, as well. The magneto-phonon spectrum of an infinite 2D Wigner crystal in a magnetic field was obtained in [128, 152]. In the case of chain-like systems in the presence of B , Eq. (4.1) is modified to:

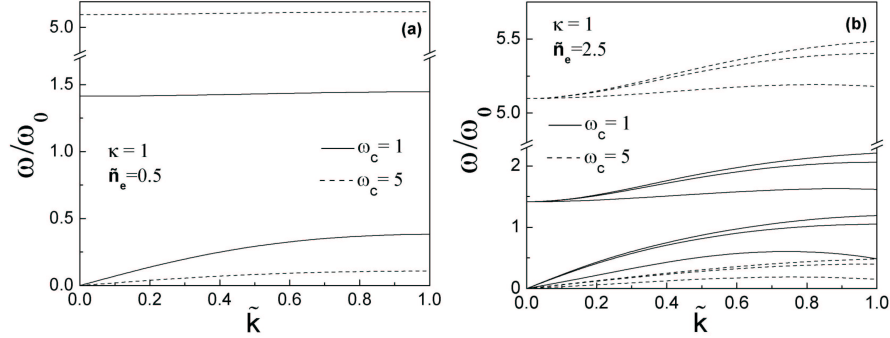


FIG. 4.3: Typical dispersion curves for the one (a) and three (b) chain structures for two different magnetic field values.

$$[(\omega^2 - \delta_{\beta\gamma})\delta_{\alpha\beta,ij} - D_{\alpha\beta,ij} + i\omega\omega_c\xi_{\alpha\beta}\delta_{ij}]Q_{\beta,j} = 0. \quad (4.9)$$

where $\xi_{\alpha\beta}$ is the Levi-Civita tensor and $\omega_c = qB/mc$ is the cyclotron frequency. In Fig. 4.3 some typical dispersion curves for the one and three-chain structures for different values of ω_c are depicted. It is interesting to notice how the optical modes couple with the magnetic field, the optical frequencies follow the cyclotron frequency and for very high field strength there is no significant difference between ω_{opt} and ω_c . The acoustical frequencies on the other hand decrease with the magnetic field strength.

For the single chain the eigenfrequencies are modified to:

$$\omega(k) = \left\{ \frac{1}{2}(1 + B'_1 + B'_2 + \omega_c^2) \pm \frac{1}{2}[(1 + B'_1 + B'_2 + \omega_c^2)^2 - 4B'_1(1 + B'_2)]^{1/2} \right\}^{1/2}, \quad (4.10)$$

where B'_1 and B'_2 are given in Appendix B. For very large field when $\omega_c \gg \{B'_1, B'_2, 1\}$ the gap between the optical branches and the acoustical ones approaches ω_c . The optical frequency reflects the cyclotron motion of the system which suppresses any soft excitation. As in the absence of magnetic field, it is interesting to study the normal modes at the critical density of the transition from the one-chain to the two-chain structure (see Fig. 4.4). We observe that there is always softening at the same density, independently of the strength of the magnetic field, but with a main difference that for zero magnetic field strength the modes which soften is the optical one while when the magnetic

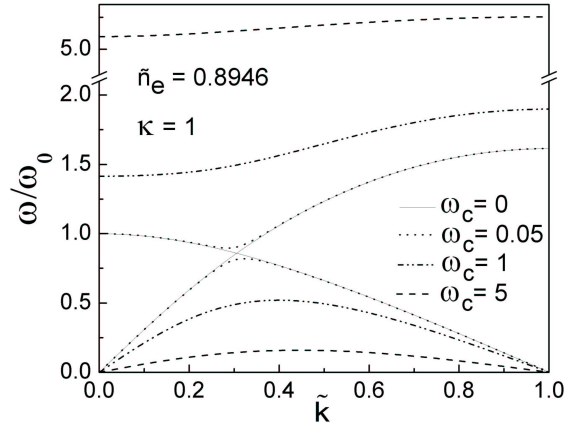


FIG. 4.4: The magnetic field dependence of the softening of the phonon mode at the structural transition from one to two chains.

field strength is nonzero, the acoustic mode is the one that softens. The magnetic field induces a coupling between the acoustical and the optical modes and there is an anti-crossing between the two branches. Although these findings confirm the previous assertion that the presence of B does not alter the structural properties of the system it also reveals the differences (softening of the acoustic mode at the same density, influence on the gap between optical and acoustical branches and on eigenfrequencies within each branch) which are induced by the magnetic field.

4.1.3 Natural modes in the presence of friction and in the absence of an external magnetic field

In laboratory experiments dissipative effects due to interactions with the environment in which the system is embedded are always present. In the case of a dusty plasma the particles experience a frictional drag due mainly to the background neutral gas as well as ions. This drag has a significant effect on the dispersion curves of the normal modes. In order to compare experimental data with theory, it is necessary to develop a theoretical model in which the structure of the crystal as well as damping are included as essential elements. This can be easily done by adding explicitly the friction term $-\gamma\dot{\mathbf{r}}_i$ in the equations of motion. The equations of motion in the harmonic approximation for the 1, 2 and 3 chain structures are reported for completeness in Appendix B.

Proceeding as in Sec. 4.1.1, in this case the eigenfrequencies are determined by:

$$[(\omega^2 - \delta_{\beta y} + i\gamma\omega)\delta_{\alpha\beta,ij} - D_{\alpha\beta,ij}]Q_{\beta,j} = 0. \quad (4.11)$$

For a single chain Eq. (4.11) gives explicitly:

$$\omega_{ac}^2 + i\gamma\omega_{ac} - \tilde{n}_e^3 \sum_{j=1}^{\infty} \frac{\exp(-j\kappa/\tilde{n}_e)}{j^3} \left(2 + \frac{2j\kappa}{\tilde{n}_e} + \frac{j^2\kappa^2}{\tilde{n}_e^2} \right) [1 - \cos(ka_j)] = 0, \quad (4.12a)$$

$$\omega_{opt}^2 + i\gamma\omega_{opt} - 1 + \tilde{n}_e^3 \sum_{j=1}^{\infty} \frac{\exp(-j\kappa/\tilde{n}_e)}{j^3} \left(1 + \frac{j\kappa}{\tilde{n}_e} \right) [1 - \cos(ka_j)] = 0, \quad (4.12b)$$

from which we obtain the solutions:

$$\omega_{ac}(k) = \left\{ \tilde{n}_e^3 \sum_{j=1}^{\infty} \frac{\exp(-j\kappa/\tilde{n}_e)}{j^3} \left(2 + \frac{2j\kappa}{\tilde{n}_e} + \frac{j^2\kappa^2}{\tilde{n}_e^2} \right) \times [1 - \cos(ka_j)] - \frac{\gamma^2}{4} \right\}^{1/2} - i\frac{\gamma}{2}, \quad (4.13a)$$

$$\omega_{opt}(k) = \left\{ 1 - \tilde{n}_e^3 \sum_{j=1}^{\infty} \frac{\exp(-j\kappa/\tilde{n}_e)}{j^3} \left(1 + \frac{j\kappa}{\tilde{n}_e} \right) \times [1 - \cos(ka_j)] - \frac{\gamma^2}{4} \right\}^{1/2} - i\frac{\gamma}{2}. \quad (4.13b)$$

The analytical expression for the 2 and 3 chain eigenfrequencies are reported in Appendix B.

In the limit of small wavenumber k , in the same spirit of Sec. 4.1.1, we find for $\kappa/\tilde{n}_e \gg 1$ that Eqs. (4.13a) and (4.13b) reduce respectively to:

$$\omega_{ac}(k) = \left\{ e^{-\kappa/\tilde{n}_e} \frac{\kappa^2 \tilde{n}_e}{2} \left(1 - \frac{k^2 a^2}{12} \right) k^2 a^2 - \frac{\gamma^2}{4} \right\}^{1/2} - i\frac{\gamma}{2}, \quad (4.14a)$$

$$\omega_{opt}(k) = \left\{ 1 - e^{-\kappa/\tilde{n}_e} \frac{\tilde{n}_e^2 \kappa}{2} \left(1 - \frac{k^2 a^2}{12} \right) k^2 a^2 - \frac{\gamma^2}{4} \right\}^{1/2} - i\frac{\gamma}{2}, \quad (4.14b)$$

while for $\kappa/\tilde{n}_e \ll 1$ we find:

$$\omega_{ac}(k) = \left\{ \left[\frac{3}{2} + \ln \left(\frac{\tilde{n}_e}{\kappa} \right) - \frac{\tilde{n}_e}{12} \left(1 + \frac{5\tilde{n}_e}{12} \right) k^2 a^2 \right] \tilde{n}_e^3 k^2 a^2 - \frac{\gamma^2}{4} \right\}^{1/2} - i\frac{\gamma}{2}, \quad (4.15a)$$

$$\omega_{opt}(k) = \left\{ 1 - \left[1 + \ln \left(\frac{\tilde{n}_e}{\kappa} \right) - \frac{\tilde{n}_e}{\kappa} \left(1 + \frac{2\tilde{n}_e}{\kappa} \right) k^2 a^2 \right] \frac{\tilde{n}_e^3 k^2 a^2}{2} \frac{k^2 a^2}{12} - \frac{\gamma^2}{4} \right\}^{1/2} - i \frac{\gamma}{2}. \quad (4.15b)$$

The real part of the frequency corresponds to the oscillatory motion while the damping in the time domain is given by the imaginary term $i\gamma/2$. Note that friction also effects value of the frequencies of normal modes. In Fig. 4.5 the normal mode spectra are reported for the different configurations of the system for different values of \tilde{n}_e , κ and γ . We used in our calculations values for the parameters inferred from the experiment [51]. The behavior of the dispersion curves reflects rather closely the case without damping. Some new features should, however, be stressed: i) the effect of friction results in general into a reduction of the frequencies of vibration both for the longitudinal motion and for the transversal one; ii) for very small values of the wave number the acoustical vibrations cannot be excited, which implies that they are overdamped. Such waves can only be excited when $k > k^*(\tilde{n}_e, \kappa, \gamma)$; iii) the softening of the optical mode at the critical density \tilde{n}_e^* for the transition $1 \rightarrow 2$ depends on γ' , in particular the presence of friction reduces the value of \tilde{n}_e^* (see Fig. 4.5(b)).

4.1.4 Natural modes in the presence of friction and in the presence of an external magnetic field

When we include a magnetic field the damped normal modes are determined by:

$$[(\omega^2 - \delta_{\beta y} + i\gamma\omega)\delta_{\alpha\beta,ij} - D_{\alpha\beta,ij} + i\omega\omega_c \xi_{\alpha\beta} \delta_{ij}] Q_{\beta,j} = 0. \quad (4.16)$$

The corresponding dispersion curve for the single and multi-chain structures are reported in Fig. 4.6. The behavior of the curves resembles the case without damping but with an additional shift in frequency due to friction. Note that in this case it is no longer possible to obtain the phonon frequencies analytically. The anti-crossing between the two branches in the 1 chain configuration is still present (see Fig. 4.5(b)), as in the case without friction (see Fig. 4.3). It is remarkable that the cyclotron motion and the friction are coupled and the magnetic field introduces a dispersion in the imaginary part of ω as well. Now, $Im(\omega)$ is no longer constant as a function of the wavevector as in the case without a magnetic field. Friction mainly alters the acoustical branches of the magneto-phonon modes for small wavevectors.

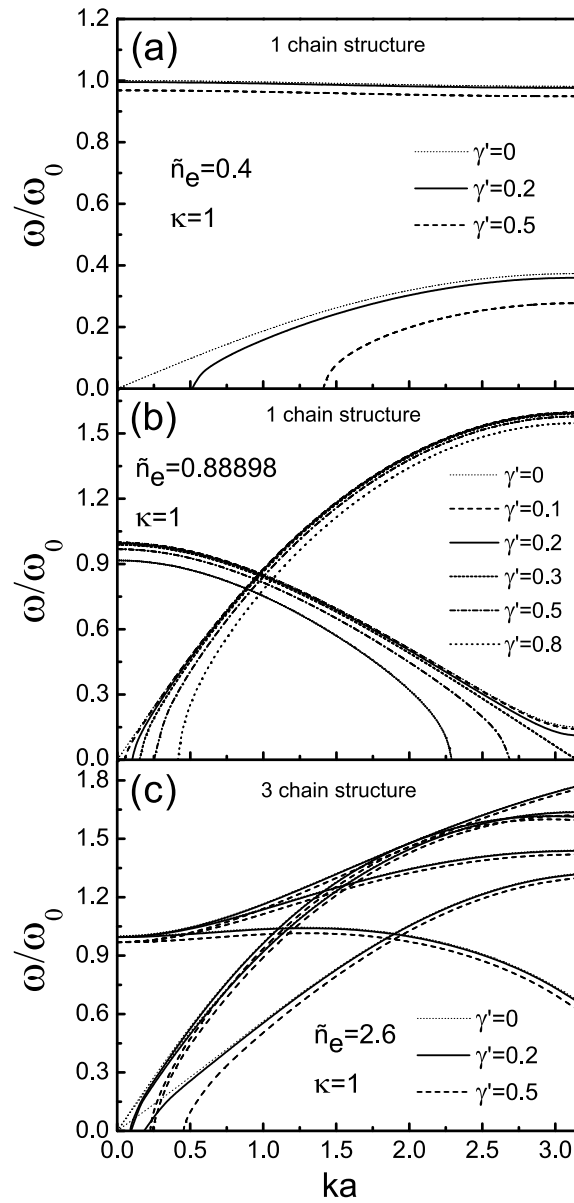


FIG. 4.5: Dispersion curves for the normal modes in the presence of friction for different values of parameters for a one (a), three (c) chain structure. Dependence of the acoustical and optical branches in the one chain case on the friction coefficient at the critical density where the softening of the optical mode is observed is given in (b).

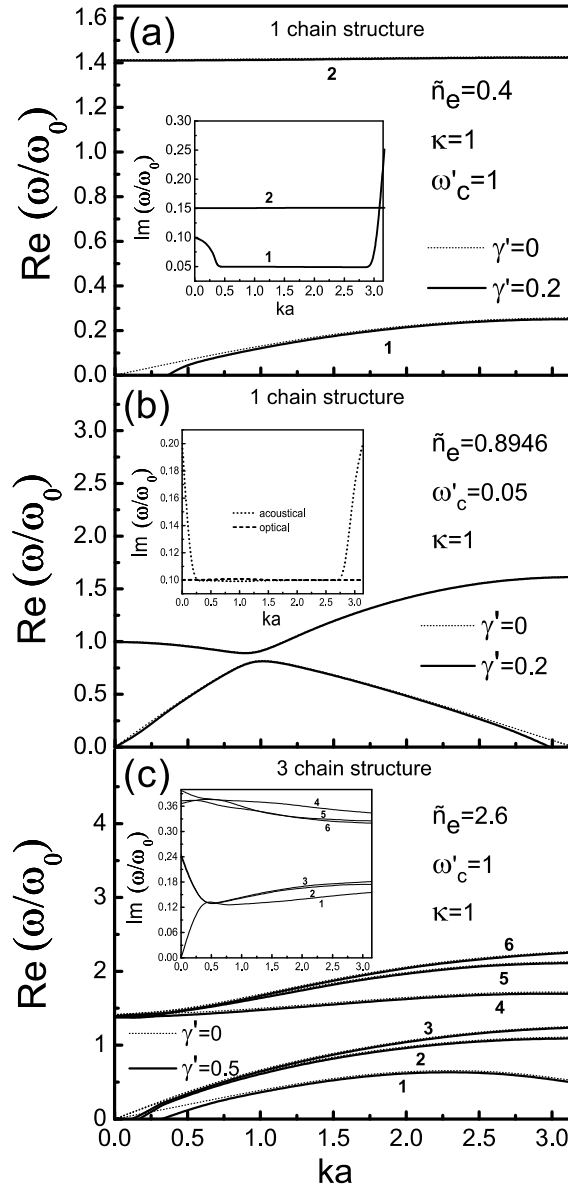


FIG. 4.6: The same as Fig. 4.5 but now a magnetic field of strength $\omega_c/\omega_0 = 1$ is present. The insets depict the damping of magneto-phonon modes.

4.2 FORCED OSCILLATIONS

In the experiments on complex plasma crystals of Refs. [50, 51, 62, 64, 65, 167] the system is set into oscillation by an external driving force which acts on the system continuously. The frequency of such a *forced oscillation* is then determined by the frequency of the driving force and not by the resonant frequencies. This is the effective situation in the experiments where particle motions are excited by laser manipulation, which makes it possible to excite and test the dispersion relations of certain types of lattice wave [62, 64, 166, 167], that are longitudinal waves and, most recently also, transverse waves were observed [50, 51, 168]. Laser light exerts a radiation pressure on the particles with a magnitude proportional to the laser intensity [65]. In these cases the frequency is purely real since the modes are driven. What is observed in the experiments, is that as the wave propagates it is spatially damped, which can be interpreted in term of a complex wave number [166] $k = k_r + ik_i$.

4.2.1 Forced oscillations in a single chain structure

Following this idea and considering that excitations take place when the driving frequency is close to the free frequency of the modes, we may neglect to first approximation for the single chain structure the external force and we looked for particular solutions of the equations of motion, in the form:

$$(x'_n, y'_n) \propto \exp[i(k_r na - \omega t)] \exp(-k_i na) \quad (4.17)$$

as it was done in Ref. [51] for the theoretical calculation of the optical branch. This yields for the acoustical and optical branch, respectively:

$$\begin{aligned} \omega_{ac}^2 + i\gamma\omega_{ac} - \tilde{n}_e^3 \sum_{j=1}^{\infty} \frac{\exp(-j\kappa/\tilde{n}_e)}{j^3} \left(2 + \frac{2j\kappa}{\tilde{n}_e} + \frac{j^2\kappa^2}{\tilde{n}_e^2} \right) \times \\ [1 - \cos(k_r a j) \cosh(k_i a j) + i \sin(k_r a j) \sinh(k_i a j)] = 0, \end{aligned} \quad (4.18a)$$

$$\begin{aligned} \omega_{opt}^2 + i\gamma\omega_{opt} - 1 + \tilde{n}_e^3 \sum_{j=1}^{\infty} \frac{\exp(-j\kappa/\tilde{n}_e)}{j^3} \left(1 + \frac{j\kappa}{\tilde{n}_e} \right) \times \\ [1 - \cos(k_r a j) \cosh(k_i a j) + i \sin(k_r a j) \sinh(k_i a j)] = 0. \end{aligned} \quad (4.18b)$$

Requiring the frequency ω to be real, both equations generate a system of two non linear equations, for k_r and k_i . The results of the calculation are reported in Fig. 4.7. This approach has, however, some limits. First of all, once the laser acts on a specific particle [51], it is no longer possible to consider all the particle as identical, i.e. the presence of an external force breaks the symmetry of the system which is taken into account in Eq. (4.17) by considering

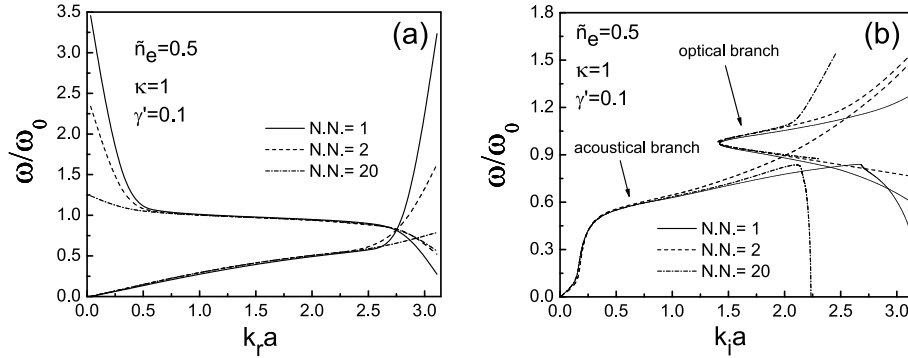


FIG. 4.7: Dispersion relations for a single chain structure as a function of the: (a) real part and (b) imaginary part of the wavevector. The curves show a strong dependence on N.N., the number of nearest neighbors included in the calculations, at the edges of the first Brillouin zone.

the driven particle as being $x_{n=0} = 0$. Second, the convergence of the series in Eq. (4.18a) and Eq. (4.18b) is no longer guaranteed. The condition that must be fulfilled in order to have a convergent sum is $k_i a \leq \kappa/\tilde{n}_e$. As seen from Fig. 4.7(b), this condition is not always satisfied (in the specific case considered in the picture the condition for convergence is $k_i a \leq 2$). Note that the dispersion curves depend strongly on the number of terms considered in the sum at the edges of the first Brillouin zone (Fig. 4.7(a)), while it is practically independent of the number of neighbors considered in the sum in the middle of the first Brillouin zone. The system of equations arising from Eqs. (4.18a) and (4.18b) is not defined when $ka = 0$ and $ka = \pi$, because in this case the equation for the imaginary part is identically zero. This clearly shows the inapplicability of this approach to obtain the phonon spectrum in the presence of friction.

The reason for the divergence of the sums in Eqs. (4.18a) and (4.18b) is a consequence of the fact that the last exponent in Eq. (4.17) blows up for negative values of n . This would suggest that alternatively we should look for solutions of the equation of motion in the form:

$$(x'_n, y'_n) \propto \exp[i(k_r n a - \omega t)] \exp(-k_i |n| a), \quad (4.19)$$

i.e. damped waves propagating from the location of external excitation. But in this case in the imaginary part in Eqs. (4.18a) and (4.18b) the hyperbolic sine term is replaced by $\exp(-k_i |j| a)$ and consequently the sum gives zero. As a result, Eqs. (4.18a) and (4.18b) do not have any real solutions for the phonon frequency and this approach also fails.

In order to explain some recent experimental results on the transversal modes of a finite one dimensional chain [51], excited by striking one particle with two counterpropagating laser beams such that the effective force acting on the particle is $I_0 \sin \omega t$, with I_0 the intensity of the beam, we have followed another approach. We first consider a single finite chain of N particles confined in the y direction. On one of the particles a time varying force is acting. We studied the small displacements from the equilibrium configuration of each particle, limiting ourselves to first neighbor interactions, which is valid for $ka > 1$. The equations of motion for such a system are:

$$\frac{d^2 x'_l}{dt'^2} + \gamma \frac{dx'_l}{dt'} = \tilde{n}_e^3 e^{-\kappa/\tilde{n}_e} \left(2 + \frac{2\kappa}{\tilde{n}_e} + \frac{\kappa^2}{\tilde{n}_e^2} \right) (x'_{l+1} + x'_{l-1} - 2x'_l) + F_0^x e^{-i\omega t} \delta_{l,N}, \quad (4.20a)$$

$$\frac{d^2 y'_l}{dt'^2} + \gamma \frac{dy'_l}{dt'} = -\tilde{n}_e^3 e^{-\kappa/\tilde{n}_e} \left(1 + \frac{j\kappa}{\tilde{n}_e} \right) (y'_{l+1} + y'_{l-1} - 2y'_l) - y'_l + F_0^y e^{-i\omega t} \delta_{l, \frac{N}{2}}, \quad (4.20b)$$

with $l = 1, 2, \dots, N$ and $F_0^{x,y}$ the dimensionless strength of the driving force. In order to excite the longitudinal vibrations we have considered a force directed along x and acting on one of the extremity of the chain, while to excite the transversal modes the force acts on the particle in the middle of the chain and with y component only, as it was done experimentally in Ref [7]. Looking for a particular solution of Eqs. (4.20a) and (4.20b) of the form:

$$(x'_l, y'_l) = (A_l^x, A_l^y) e^{-i\omega t} \quad (4.21)$$

we obtained the following set of inhomogeneous linear equations for the displacements A_l :

$$\beta_1 A_{l-1}^x + (\omega_{ac}^2 + i\gamma\omega_{ac} - 2\beta_1) A_l^x + \beta_1 A_{l+1}^x - F_0^x \delta_{l,N} = 0, \quad (4.22a)$$

$$\beta_2 A_{l-1}^y + (\omega_{opt}^y - 1 + i\gamma\omega_{opt} - 2\beta_2) A_l^y + \beta_2 A_{l+1}^y - F_0^y \delta_{l, \frac{N}{2}} = 0, \quad (4.22b)$$

where $\beta_1 = \tilde{n}_e^3 e^{-\kappa/\tilde{n}_e} (2 + 2\kappa/\tilde{n}_e + \kappa^2/\tilde{n}_e^2)$ and $\beta_2 = \tilde{n}_e^3 e^{-\kappa/\tilde{n}_e} (1 + \kappa/\tilde{n}_e)$. The solution to these equations may easily be obtained from Kramer's rule [169]:

$$A_l = \frac{D_l(\omega)}{D(\omega)} \quad (4.23)$$

where $D(\omega)$ is the determinant of the coefficients of A_l in Eqs. (4.22a) and (4.22b) and $D_l(\omega)$ is the modification in $D(\omega)$ resulting when the l th column is replaced by $(F_0, 0, 0, \dots, 0)$ for the longitudinal motion and $(0, 0, \dots, 0, F_0, 0, \dots, 0, 0)$ for the transverse motion respectively. A_l are complex quantities when $\gamma \neq 0$ and the formalism developed above allows to calculate amplitudes and phases. The analytical expressions for A_l are reported in Appendix B.

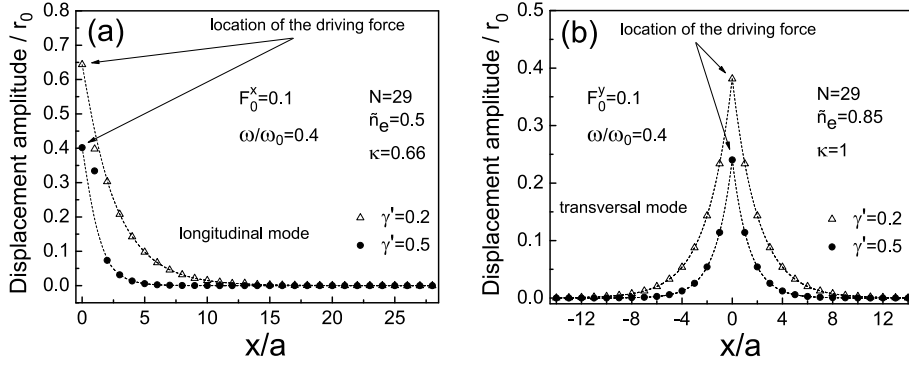


FIG. 4.8: Amplitude of the displacements of particles as a function of the distance from the location of the driving force: (a) displacements along the x -direction when the excited particle is at the extremity of the chain, (b) displacements along y -direction when the excited particle is in the middle of the chain. Exponential fits to the numerical data are shown by the dotted curves.

In Fig. 4.8(a-b) we show the amplitudes of the displacements for the longitudinal and transverse motion as a function of particle position along the chain. The plots clearly show an exponential decay. Regarding the displacements in the longitudinal modes, there are edge effects, which disappear if the particle which is excited is being in the center of the chain. In principle this cannot be realized in the experiments, however except for the first two particles the amplitudes of the displacements have the same damping rate and the same phase angles both if the excited particle is the one at the end of the chain and the one in the middle. This is why for all the calculations we have considered a force $F_0^x e^{-i\omega t} \delta_{l,N/2}$ instead of $F_0^x e^{-i\omega t} \delta_{l,N}$ in Eq. (4.22a).

Fitting the amplitudes to an exponential curve yields k_i . In order to find the dispersion of k_r , we calculated the wave's phase ϕ as a function of the position and fitted it to a straight line. The definition of phase velocity, as being the ratio between the frequency and the wave number, indeed, yields $k_r a = \Delta\phi$. In Fig. 4.9 the phase angle as a function of the distance is plotted. It is interesting to observe that k_r and k_i are independent of the intensity of the driving force F_0 , as expected in a harmonic model, and the results do not change if instead of $F_0 e^{-i\omega t}$, that is a complex force, we consider a real force $I_0 \sin \omega t$, as in the experiment; what actually plays a central role is just the driving frequency. Optical and longitudinal waves both propagate away from the excitation region; they are backward and forward, respectively. It should be noticed that in a 1D chain with finite length one should expect that only

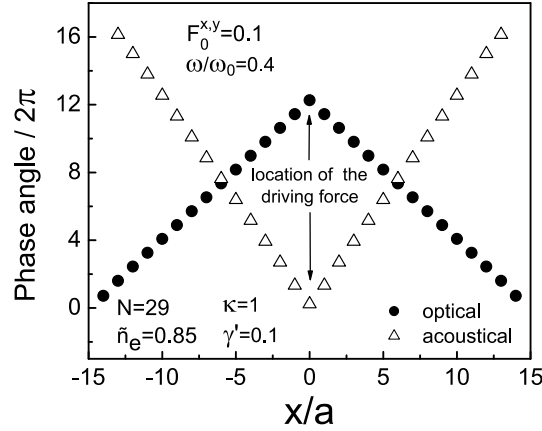


FIG. 4.9: Phase angle as a function of the distance from the location of the driving force. The calculation are done for a system of $N = 29$ particles. Optical and longitudinal waves both propagate away from the excitation region; they are backward and forward, respectively.

standing waves would be allowed, the effect of gas damping is the suppression of the reflected wave from the chain's end.

It is interesting to observe that for low densities the two calculational methods, that is the one in which the driving force is neglected and the one in which it is explicitly taken into account, give the same results for the dispersion curves, when only first neighbor interactions are included. In Fig. 4.10 the results of the two approaches for the optical branch are compared. Note that outside the bond defined by the two dotted horizontal lines the phonon mode is strongly damped.

Another remarkable effect, which reflects the anisotropy of the system, is observed with increasing density: the profile of displacements for the longitudinal mode is no longer a pure damped exponential (see Fig. 4.11(a)), because reflected waves from the chain's end start to appear, while the amplitudes for the transversal mode are still exponentially decaying. We can infer that the effect of damping is not simply due to friction, but also to the external confining potential. This is confirmed by the calculation of the amplitude profile when $\gamma = 0$, which is reported in Fig. 4.11(b): even in the absence of the friction and in the case the driving frequency is low enough, an exponential decay of amplitudes with distance is still found.

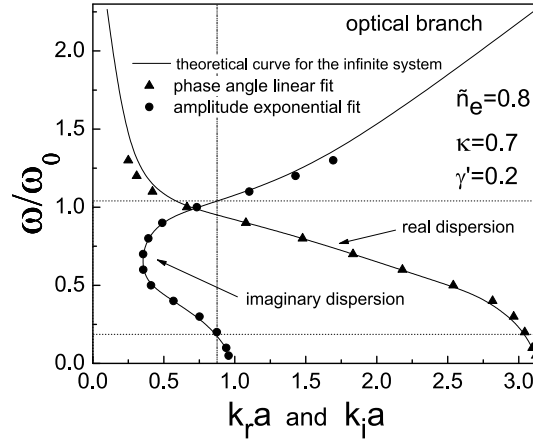


FIG. 4.10: Comparison between the standard calculation, in which the external driving force is neglected, and the "exact" one, in which the external driving force is explicitly considered. The region on the left of the vertical dotted curve is the region in which the condition $k_x a \leq \kappa/\tilde{n}_e$ is fulfilled; the region between the horizontal dotted curves is the region in which the sums are convergent. Note that the two approaches give the same results in the region of convergence.

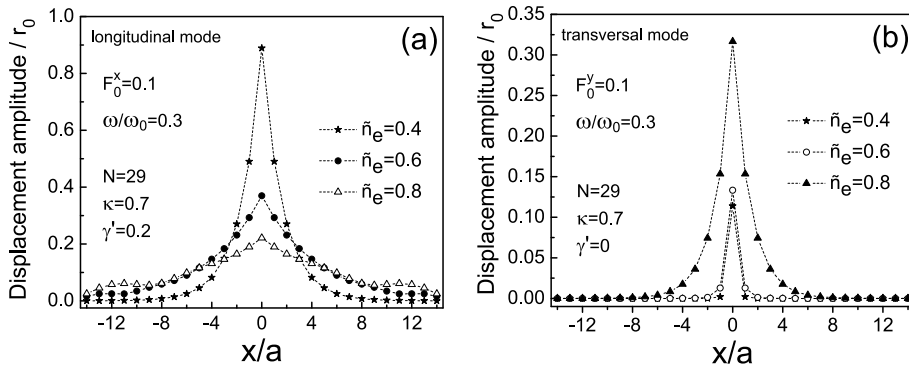


FIG. 4.11: (a) Profile of the amplitudes of displacements in the longitudinal mode as a function of the density. For high densities the profile is no longer a simply decaying exponential; (b) Profile of the amplitudes of displacements in the transversal mode as a function of the density in the case without friction. Even in the absence of friction the profile is still a decaying exponential.

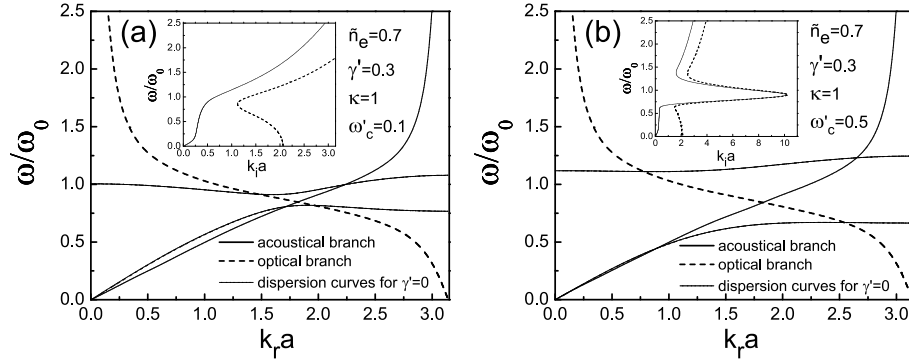


FIG. 4.12: (a) Real part of the dispersion relations for a weak perpendicular magnetic field; (b) Real part of the dispersion relations for a strong perpendicular magnetic field. The insets show the imaginary part of the dispersion relations.

4.2.2 Forced oscillations in the presence of an external magnetic field

When we include a perpendicular magnetic field, a coupling is introduced between motion along x and along y -direction. Apart from increased mathematical complexity, the scheme developed before is still valid. It is possible to infer the real part of the dispersion relations from the phase angles and the imaginary part from the amplitude of displacements. In the absence of friction and driving force, the optical and acoustical branches are confined in different frequency bands (see thin solid curves in Fig. 4.3(a,b)), which do not cross each other and with a prohibited gap. The optical frequencies follow the cyclotron frequency and for very high field strength there is no significant difference between ω_{opt} and ω_c . The acoustical frequencies, on the other hand, decrease with magnetic field strength. The gap between the optical branch and the acoustical one for large magnetic field approaches ω_c .

In the presence of friction and driving force, there are drastic changes in the dispersion relations. The frequencies are no longer confined in different bands, because the frequency of oscillation is the one of the external force, which can be varied continuously. The results of the calculations for different intensities of the magnetic field are shown in Fig. 4.12(a,b). There are no significant differences in the behavior of the real part of the dispersion relations with respect to the case without magnetic field. The imaginary dispersion relations clearly show that the waves are overdamped in the band gap, region where large values for $k_i a$ are found. Notice that friction reduces the slope of the acoustical branch in the small $k_r a$ region. When the curve enters the gap region it becomes strongly damped as is clearly seen from the inset of Figs. 9(a,b). The optical mode is for all frequencies more strongly damped than the

acoustical one. Furthermore, the dispersion of the optical branch is strongly modified by friction, i.e. it attains a negative dispersion for all values of the frequency.

4.2.3 Forced oscillations in a multi-chain structure

In Fig. 4.14 the real and imaginary part of the dispersion relations for the forced oscillations of the 2 and 3 chain configurations are reported respectively. We used the approach given in the first part of Sec. 4.2.1. Therefore, the dispersion relations are in Fig. 4.14 only given in that part of the Brillouin zone, where the sums in Eqs. (4.18a) and (4.18b) are convergent.

From Fig. 4.14 (a) and (c) it is evident that there is a remarkable difference in the optical branches between the single chain and the 2 and 3 chain structures. In the first case the optical mode has negative dispersion as stated before, while for the 2 and 3 chain structures the optical frequencies do not exhibit a monotonic behavior. Such feature can be attributed to the fact that for the single chain configuration in the case of the transversal mode the restoring force is only due to the parabolic confining potential, while in the multi-chain configuration the restoring force depends both on the external confinement and on the particle repulsion.

The dispersion curves in Fig. 4.14 (b) and (d) exhibit some similarities with the single chain case: i) for the acoustical modes the damping is an increasing function of the driving frequency, ii) the optical modes are mostly constrained to a frequency band, and iii) the optical modes are more strongly damped. The approach used for the calculation of the dispersion relations for the multi-chain is the same considered in Sec. 4.2.1 for an infinite number of particles, this is why in Fig. 4.14 the dispersion relations are not presented in the whole first Brillouin zone, but only in that range of the frequency corresponding to convergent sums.

4.3 COMPARISON WITH EXPERIMENT

In Fig. 4.14 the real and imaginary dispersion relations for the acoustical and optical modes for the finite single chain configuration are respectively presented, for different values of the parameters.

The calculated dispersion relations are compared with experimental data of Ref. [51]. The experimental data are in good agreement with the theoretical calculations, although the system realized in laboratory is slightly different from the one investigated in the theory. As a matter of fact, in the experiment the inter-particle spacing was not uniform: it was 15% smaller in the center than in the chain end. Due to the strong damping this density gradient is not very important in the considered forced oscillation. As in the case without

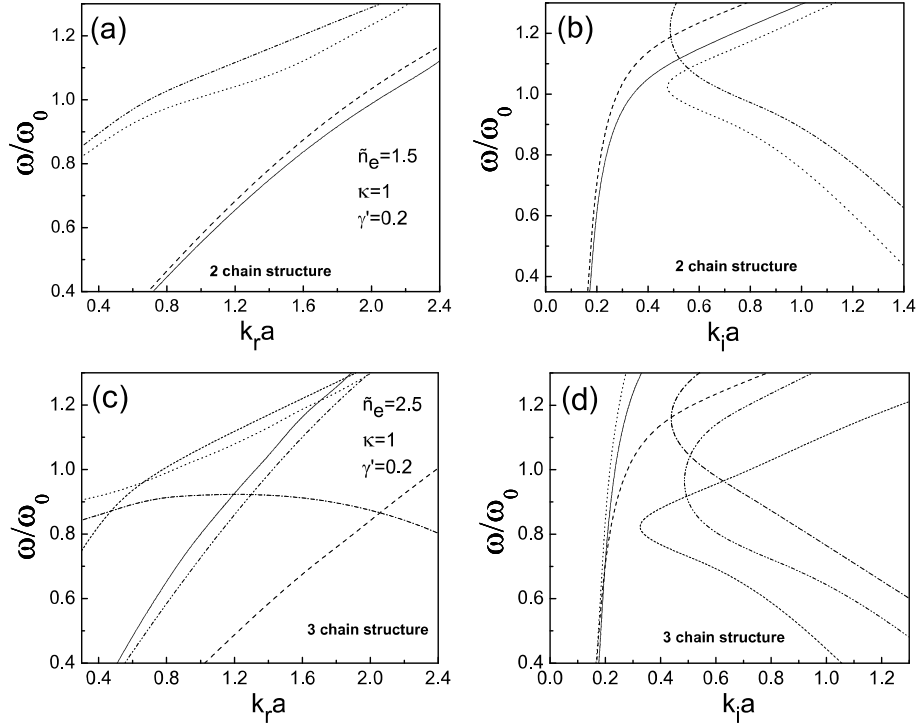


FIG. 4.13: Theoretical dispersion relations for the 2 chain structure: (a) real part, (b) imaginary part; and for the 3 chain structure: (c) real part, (d) imaginary part.

friction, the optical mode has negative dispersion, while the longitudinal one has positive dispersion. The dispersion depends on density, and therefore on inter-particle spacing. For the acoustical mode the frequencies of vibrations increase with decreasing inter-particle distance, while for optical vibration the frequencies decrease with increasing densities. Furthermore, for low \tilde{n}_e the exponential decay is stronger in both cases, which implies a highly damped wave. These findings can be easily explained because for smaller inter-particle distance the interaction forces are larger, or in other words for low densities the interaction between the particles is rather weak and consequently the effect of a local perturbation is less disruptive for the other particles. From Fig. 4.14(d) it is seen that the optical mode is mostly constrained to a central frequency band. Comparing the optical branches in the absence of friction (see Fig. 4.1(I)) with the one in the presence of gas damping, it is observed that with damping the wave propagates beyond the frequency band allowed in the absence of damping. For $k_r a = \pi$, ω_{opt} is always equal to zero when $\gamma \neq 0$

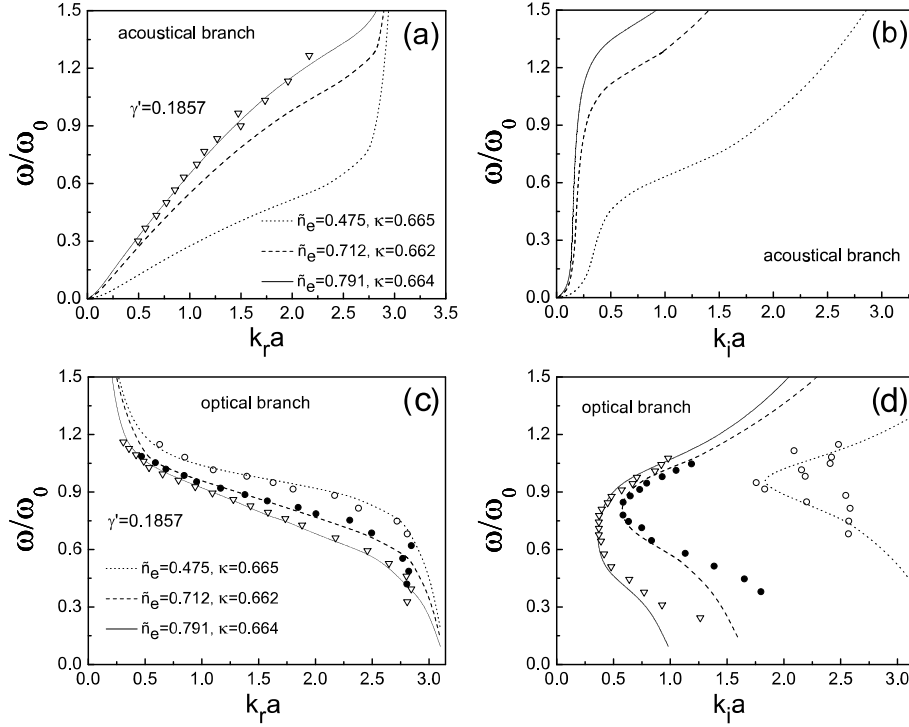


FIG. 4.14: Theoretical (curves) dispersion relations for the acoustical mode and comparison with experimental data (symbols) from Ref. [51] for the one chain structure: (a) real part of the acoustical branch; (b) imaginary part of the acoustical branch; (c) real part of the optical branch; (d) imaginary part of the optical branch.

independent of the experimental parameters. This means that in the presence of damping, the softening of the optical mode does no longer signal a structural phase transition from a single chain structure to a double chain structure.

It is, however, interesting to study the behavior of the dispersion relations when the density approaches the critical value for which the continuous structural transition from the one chain to the two chain structure occurs. The results are shown in Fig. 4.15.

The optical branch softens when approaching the critical density, while the acoustical branch is hardened. Notice that at the phase transition point: i) the real part of the optical dispersion becomes linear for $k_r a > 1.5$, ii) there is a drastic change of slope in the optical imaginary dispersion, and iii) the optical mode becomes less damped. The real and imaginary acoustical dispersions are less strongly influenced near the zig-zag transition. This can be easily explained

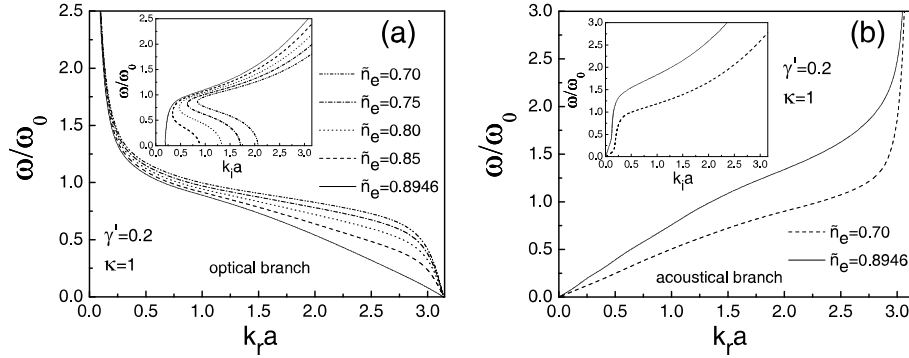


FIG. 4.15: Dispersion relations for different values of the density approaching the critical values for which the zig-zag transition from 1 chain structure to 2 chain structure is observed: (a) optical branches; (b) acoustical branches. In the insets the imaginary parts of the dispersion relations are plotted.

by the fact that the zig-zag transition, which is responsible of the splitting of the chain, acts in the y -direction. Therefore, signature of the zig-zag transition are more easily detected in the optical phonon mode.

4.4 CONCLUSIONS

The normal modes of a Q1D multi-chain system can be studied experimentally in a dusty plasma, where μm sized particles are externally confined by electric fields in the sheath above the lower electrode. The sheath conforms to the shape of the electrode, so building up an electrode with a groove-shaped depression in one direction allows the realization of a parabolic confining potential and, as a consequence, the formation of a chain-like crystal in that direction.

We investigated the normal modes of such a classical Q1D system of particles interacting through a Yukawa-type potential. The normal modes of the system were calculated first neglecting the effects of dissipation induced by gas drag and then considering explicitly the presence of friction. The normal modes consist of longitudinal (acoustical modes) and transversal (optical modes) branches. The number of acoustical branches is equal to the number of optical branches and is equal to number of chains in the system. In the presence of friction, the free oscillations of the system are exponentially damped in time. The effect of a constant magnetic field on the dispersion relations was investigated and we found that the acoustical and optical branches are significantly modified in the presence of a magnetic field.

Particular attention was paid to the case of forced oscillations induced by an external driving force, as investigated in the experiments. Both infinite and finite systems were examined. We found that earlier approaches to calculate the phonon dispersion relations are no longer valid. Our theoretical results are compared with experimental data and a remarkably good agreement between theory and experiment is found.

Finally, we made predictions for the single chain dispersion relations in the presence of a perpendicular magnetic field and for the multi-chain dispersion relations when the modes are excited by an external driving force. We found some substantial differences as well as some similarities in the dispersion relations between the single and multi-chain structures.

Publications. The result presented in this chapter were published as:

- G. Piacente, F.M. Peeters, and J.J. Betouras, *Normal modes of a quasi-one-dimensional multi-chain complex plasma*, Phys. Rev. E **70**, 036406 (2004) (13 pages).
- G. Piacente, I.V. Schweigert, J.J. Betouras, and F.M. Peeters, *Structural properties and melting of a low dimensional classical Wigner crystal*, Physica E **22**, 779 (2004) (4 pages).
- G. Piacente, I.V. Schweigert, J.J. Betouras, and F.M. Peeters, *Generic properties of a quasi-one-dimensional classical Wigner lattice*, Phys. Rev. B **69**, 045324 (2004) (17 pages).
- G. Piacente, I.V. Schweigert, J.J. Betouras, and F.M. Peeters, *Generic properties of a quasi-one-dimensional classical Wigner lattice*, Virtual Journal of Nanoscale Science and Technology, Vol. **9** (February 23, 2004).
- G. Piacente, I. V. Schweigert, J. J. Betouras, and F. M. Peeters, *Structural properties and melting of a quasi-one-dimensional classical Wigner crystal*, Solid State Commun. **128**, 57 (2003) (5 pages).

5

Melting

An important aspect, naturally occurring in the presence of a crystalline or pseudo-crystalline structure, is the melting as the temperature is raised. The mechanisms of melting is of great scientific and technological importance. At low temperature particles exhibits harmonic oscillations around their $T = 0$ equilibrium positions. Increasing the temperature produces larger and larger oscillations, until the behavior becomes liquid-like, with particles moving almost freely. Whether melting in 2D crystals is a first order transition and proceeds discontinuously or is a continuous transition in which the crystal first transits into the so called 'hexatic' phase retaining quasi-long-orientational order and then melts into an isotropic fluid, is still an open question and a controversial issue. In infinite 2D systems theory [142] based on unbinding of defects, predicts a two-stage melting where the two stages are continuous. In this Chapter we study the melting features of infinite chain-like systems, discussed in the previous chapters.

Recent theoretical studies by Frey, Nelson and Radzihovsky [44] about melting of colloidal crystals in the presence of a one-dimensional periodic potential revealed a number of novel phases and the possibility of reentrant melting. These results depend on the commensurability ratio $p = a/d_{ext}$ where a is the spacing between the Bragg planes of the 2D system and d_{ext} the period of the external periodic potential. This kind of system was realized experimentally [143] in 2D colloids in the presence of two interfering laser beams. The results

in this chapter are complimentary to that work, in the sense that a single confining potential is considered here, which is not repeated in space. Therefore it can be viewed as a study of a focused portion of the infinite 2D system, where we pay attention to only one potential trough neglecting the interaction with the rest. Furthermore, in a related work [136] which discussed the temperature equilibration of a one-dimensional Coulomb chain, two different equilibration temperatures were assigned (T_{\perp} and T_{\parallel}), reflecting the different behavior of the modes due to the strong confinement. We will show that in our model two different melting temperatures can be distinguished: one for the confined direction and the other one for the non confined direction.

With respect to the melting of Q1D systems modeled by the Hamiltonian (3.2), the main results are: (i) there is evidence that the system first melts in the non-confined direction and subsequently in the direction where it is confined exhibiting a regime similar to the 'locked floating solid' found in Ref. [44], (ii) the phase diagram exhibits reentrant melting behavior as a function of the density at fixed temperature, and (iii) a regime of frustration exists close to the structural transition points.

5.1 GENERAL DISCUSSION AND RESULTS

We study the melting of the WC by MC simulations. After the ground state configuration was achieved as explained in Chapter 3, the system was heated up by steps of size ΔT , typically $\Delta T = 5 \times 10^{-4}$, and equilibrated to this new temperature during $10^5 \div 10^6$ MC steps. In Fig. 5.1 we show typical trajectories of particles as they arise from our MC simulations. It is evident that there is a different behavior of the system in the x and the y -direction as may be expected from the anisotropy, introduced by the confining potential which acts only in the y -direction. In order to quantify the observations, we studied first the potential energy as a function of temperature (see Fig. 5.2). In the crystalline state the potential energy of the system increases practically linearly with temperature and then exhibits a very fast increase in a small critical temperature range after which it starts to increase linearly again, but now with a slightly larger slope. In the latter region the system is in the disordered, i.e. liquid, phase. The fast increase of the potential energy is indicative of the melting of the WC.

To define the critical temperature (i.e. the temperature for which a phase transition from the solid to liquid phase occurs), semi-empirical criteria are generally used. In particular, the Lindemann criterion [153] has been demonstrated to be valid to predict the melting temperature for 3D or finite 2D solids. In its simplest form this criterion states that a solid melts when the thermal vibration of its atoms becomes so strong that neighboring atoms collide with

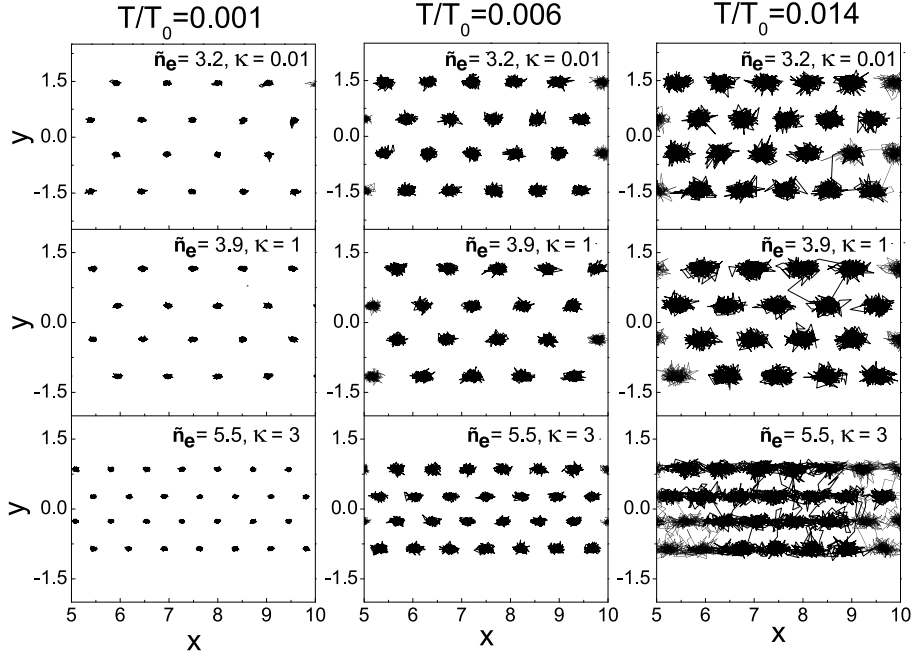


FIG. 5.1: Particle trajectories for 3×10^7 MC steps for three different temperatures and three different values of the density at $\kappa = 1$.

each other. Within this simple model and estimating the amplitude of thermal oscillations by Einstein model of solids, good agreement between theory and experiments was found in a small number of solids. An improved version of the criterion is that melting occurs when the r.m.s. amplitude of thermal vibrations reaches a critical fraction δ of the inter-particle distance a . Within the Debye model of solids and choosing a suitable value of δ (0.06-0.12) the fusion temperature of several metals was correctly predicted [154]. It should be noticed that the phenomenological Lindemann criteria do not allow a theoretical description of phase transitions, but can only give an estimate of the range of temperature in which the transition takes place. For 2D crystals, however, the Lindemann criterion, is not universal, because as showed by Peierls and Landau [149] the r.m.s. of displacements from equilibrium positions diverges logarithmically with the system size.

Therefore, to find the critical temperatures for our infinite Q1D chain-like system we studied, following the spirit of Ref. [155], the modified Lindemann parameter $L_p = \langle u^2 \rangle / d_r^2$, where $\langle u^2 \rangle$ is defined by the difference in the mean square displacements of neighboring particles from their equilibrium sites \mathbf{r}_0

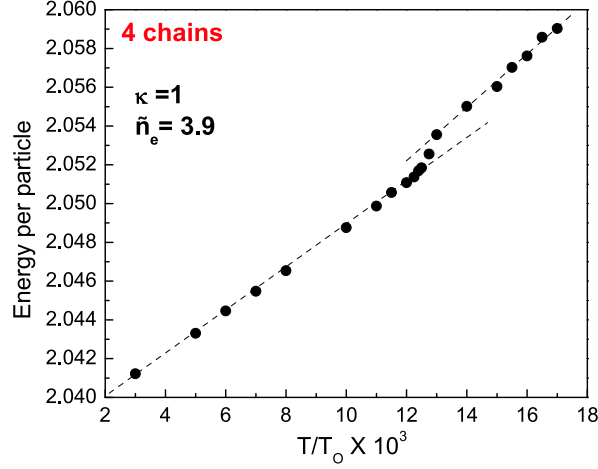


FIG. 5.2: The energy per particle as a function of temperature for the four-chain structure with $\kappa = 1$ and $\tilde{n}_e = 3.9$. There is a fast increase of the energy at the melting temperature.

and d_r is the relevant interparticle distance as we discuss below. The quantity $\langle u^2 \rangle$ can be written as:

$$\langle u^2 \rangle = \frac{1}{N} \left\langle \sum_{i=1}^N \frac{1}{N_{nb}} \sum_{j=1}^{N_{nb}} [(\mathbf{r}_i - \mathbf{r}_{0i}) - (\mathbf{r}_j - \mathbf{r}_{0j})]^2 \right\rangle \quad (5.1)$$

where $\langle \rangle$ means the average over the MC steps, N is the total number of particles in our simulation unit cell and the index j denotes the N_{nb} nearest neighbors of particle i . In Ref. [156] it was shown that an infinite 2D crystal undergoes a phase transition to the fluid state when $L_p \sim 0.1$.

In order to describe more accurately the difference between the the x and y -direction, we studied separately $\langle u_x^2 \rangle$ and $\langle u_y^2 \rangle$ as function of temperature. For the melting along the x -direction, the distance d_r is the inter-particle distance a introduced in Chapter 3 (Sec. 3.2), while for melting along the y -direction d_r is the inter-chain distance which is a function of the density \tilde{n}_e .

At low temperatures, the mean square relative displacements slowly increases linearly with temperature as a consequence of harmonic oscillations of the particles about their equilibrium positions (see Fig. 5.3). From Fig. 5.3 we notice clearly that this linear increase is larger in the unconfined direction than in the confined direction. In some critical temperature region, $\langle u_x^2 \rangle$ and $\langle u_y^2 \rangle$ start to increase very rapidly which is the consequence of the fact that the

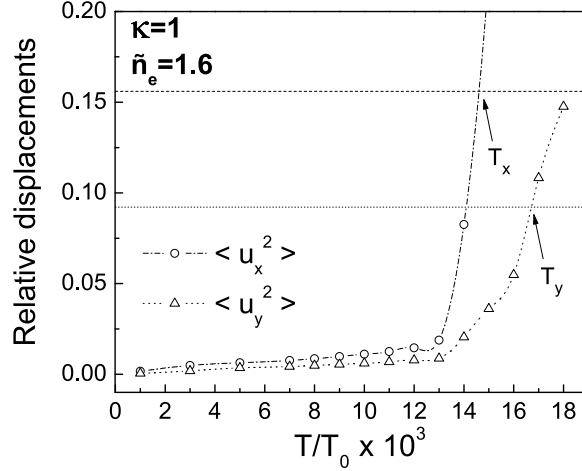


FIG. 5.3: The mean square relative displacements for $\kappa=1$, $\tilde{n}_e=1.6$ in the case of the two-chain configuration. The dashed horizontal line corresponds to the modified Lindemann criterion (MLC) in the unconfined direction, while the dotted line corresponds to the MLC in the confined direction.

particles have attained sufficient thermal energy that they can jump between different crystallographic positions. According to the modified Lindemann criterion (MLC), as claimed before, when L_p reaches the (semi-empirical) critical value 0.1 the system melts. This criterion was used to define the melting temperature T_m .

From the corresponding analysis two different melting temperatures, T_x and T_y , can be assigned. The results are summarized in the phase diagram of Fig. 5.4(a-c) for $\kappa = 0.01, 1$ and 3 , respectively. There are several interesting features in these phase diagrams: (i) the nearly Coulomb system ($\kappa = 0.01$) has a melting temperature which is on average 15-20% higher than for the screened Coulomb inter-particle interaction with $\kappa = 1$, which has on its turn an average melting temperature about 15% higher than the screened Coulomb system with $\kappa = 3$. Therefore, we conclude that the effect of screening is to reduce the melting temperatures; (ii) a *reentrant* behavior is observed as a function of density, the minima of the melting temperatures occur at the values of the density where the structural phase transitions were predicted (see Fig. 3.2); (iii) there is a regime close to each structural transition point where the system is 'frustrated', in the sense that it fluctuates between the two structures. In this regime, which we term as *frustration regime*, the system makes continuous transitions from one metastable state to the other which strongly reduces the

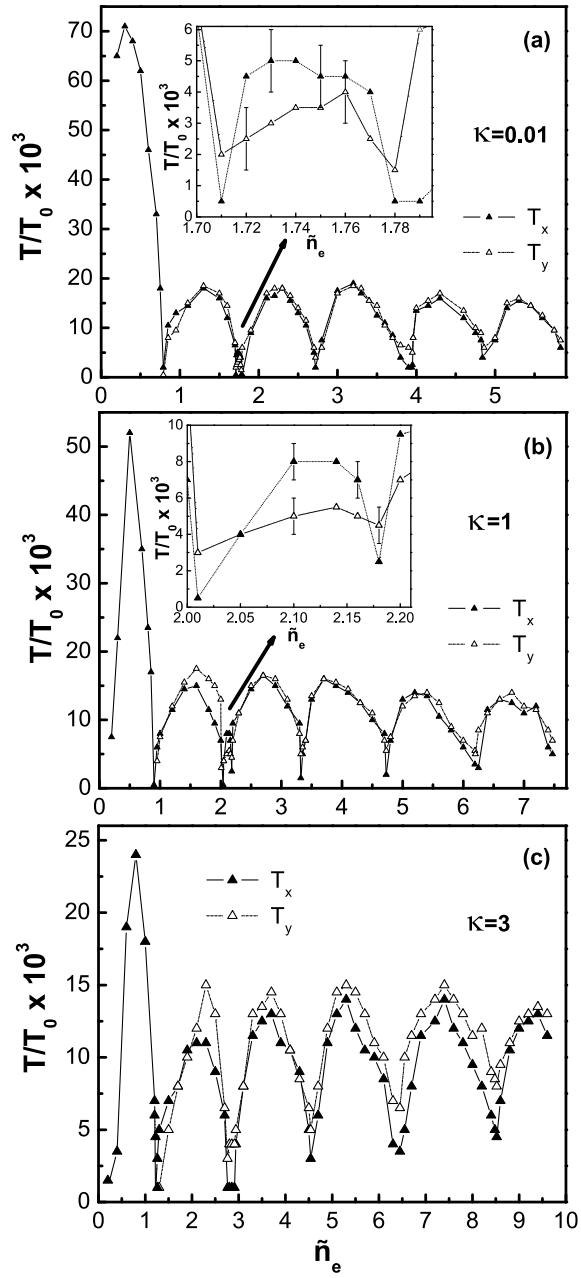


FIG. 5.4: Melting temperature as a function of density for: (a) $\kappa = 0.01$, (b) $\kappa = 1$, and (c) $\kappa = 3$. The insets in (a) and (b) show an enlargement of the four-chain region which is located between the two and three chain phase.

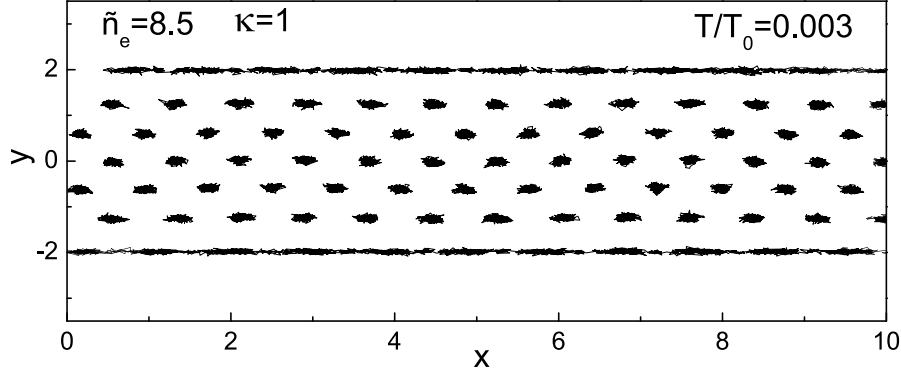


FIG. 5.5: Particle trajectories for 3×10^7 MC steps which qualitatively illustrates the different melting behavior at the boundaries due to the confining potential for $\kappa = 1$.

melting temperature; (iv) for $\kappa = 1$ and $\kappa = 3$, there is a region in density for which the system melts first in the unconfined direction while it is not melted in the confined one. This regime resembles the findings of Ref. [44] in the regime termed as 'locked floating solid'. For the Coulomb limit there is no evidence of anisotropic melting within the error bars of our simulation. The system behaves more isotropic; (v) the first four-chain regime (see insets of Fig. 5.4(a-c)) is unstable with respect to temperature fluctuations as it is reflected in the relative low melting temperature. In this region, melting occurs first in the confined direction as a consequence of the particular structural properties -the distance between the two internal chains is larger than the distance between an internal chain and the adjacent external one- which makes the system unstable in the y -direction. In the rest of the diagram there is evidence that the melting either starts from the unconfined direction (e.g. it is clear in the single chain and in the low density limit of the two-chains) or the system melts simultaneously in both directions. (vi) The single-chain structure shows a relatively large melting temperature as obtained by the MLC and deserves more attention. The study of the single-chain is therefore postponed to the next section.

Furthermore, it should be pointed out that the MLC only takes into account the displacement of the particles relative to the position of their neighbors and consequently is only a measure of the local order of the system.

Another natural question that arises is whether there is anisotropic melting with respect to external and internal chains in the multi-chain structures or in other words if melting starts from the edges as observed in the experiment of Ref. [33] with electrons on liquid helium. The number of filaments that were

observed in the experiment was approximately 20; we have simulated the trajectories of some multi-chain structures and the results are presented in Fig. 5.5. In this picture it is clear that the most external chains are already melted while the internal ones are still ordered. Edge melting has also been demonstrated in the presence of a strong magnetic field in Ref. [160], using Hartree-Fock calculations in a two-dimensional Wigner crystal with edges. With the aid of many numerical simulations of multi-chain systems at different densities we observed that this kind of melting is present in our system when the density is close enough to the critical density of a structural transition. Close to the structural transition many metastable states appear with a different number of particles per chain, that is in the most external chains there are less particles than in the internal ones. Thus the particles at the most external chains have larger displacements from their equilibrium positions in order to attain the stability of the structure. Moreover, we calculated the average root mean square displacements of the particles from their equilibrium position chain by chain and also $\langle u_x^2 \rangle$ chain by chain and we actually noted that these quantities are slightly larger for external chains at temperatures below the critical one. In Fig. 5.6 the temperature dependence of the standard deviation $s_x^2 = \langle (u_x - \langle u_x \rangle)^2 \rangle$ and $s_y^2 = \langle (u_y - \langle u_y \rangle)^2 \rangle$ for the external and internal chains in the four-chain structure are represented. It is evident that the position of the particles at the edges fluctuates substantially more than the particles at the interior. We can conjecture that, according to this physical picture, melting can start from the edges. However, for up to the six-chain configuration for each chain the quantities $\langle u_x^2 \rangle$ reached the critical value, approximately, all at the same temperature. Probably, going to a larger number of filaments one can well appreciate a different melting temperature for external and internal chains. Finally, the chain configuration as well as the melting which starts from the direction of the chains is supported also by molecular dynamics simulations of the flow of electrons in Q1D channels [159].

5.2 MELTING OF THE SINGLE-CHAIN

In Fig. 5.4(a-c) we observe a rather high melting temperature in case of the one-chain structure. The origin of this behavior can be traced back to the fact that the MLC takes into account a larger contribution from jumps of particles between crystallographic positions which for the single chain structure occurs only at extremely high temperature. For the single-chain case the jumps can only occur along the chain which requires a larger energy than jumps of particles between different chains.

To have a better insight we investigated the behavior of L_p for different densities, as illustrated in Fig. 5.7. We notice that in the low density limit, $L_p \approx 0.1$ is reached in a region in which there is only a gradual increase in $\langle u_x^2 \rangle$,

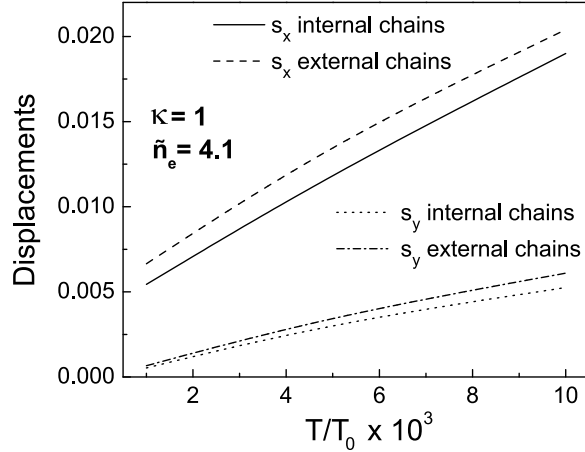


FIG. 5.6: Temperature dependence of the displacements in both the unconfined and confined directions for external and internal chains in the four-chain structure.

which is very different from the multi-chain case (see Fig. 5.3). Moreover, $\langle u_x^2 \rangle$ exhibits a sub-linear temperature increase.

This calls for the use of other possible criteria in order to clarify the situation. On the other hand if the density is relatively high (see Fig. 5.7), a fast increase is observed signaling a clear melting of the system. The transition from a low temperature linear to sub-linear behavior occurs for $\tilde{n}_e \approx 0.4$.

To shine light into the posed questions we studied also the pair correlation function at different densities and temperatures, as defined by:

$$g(x) = \frac{L}{N^2} \sum_{i \neq j} \langle \delta[x - (x_i - x_j)] \rangle, \quad (5.2)$$

where in the summation over N particles in a system of length L , the diagonal terms ($i = j$) are excluded. The results are reported in Fig. 5.8. It is rather evident that the melting temperature is substantially smaller than the one obtained from the MLC. In order to better quantify the melting temperature for the one-chain structure we investigated the height of the first and second peak of the pair correlation function as a function of temperature (see Fig. 5.9) in order to look for a structure or an anomalous jump (as found in Ref. [161]) that could identify the critical temperature. As is apparent from Fig. 5.9 we do not find any abrupt changes. The first and second peak as a function of temperature can be fitted by: $g_i = \alpha(T/T_0)^{-\beta}$, where $i = \{1 \text{ or } 2\}$ denotes the peak (see the curves in Fig. 5.9).

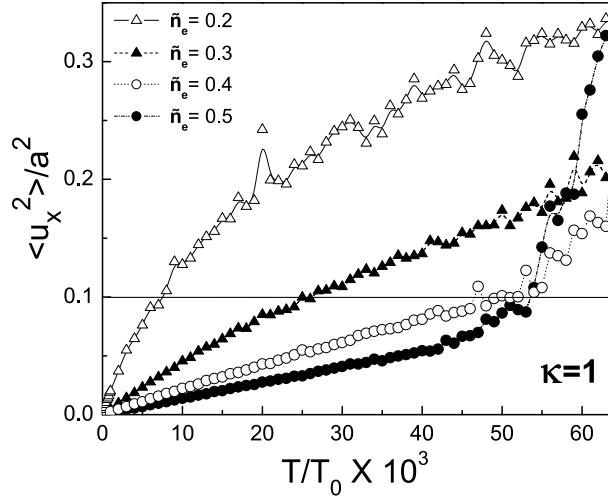


FIG. 5.7: The behavior of the Lindemann parameter, for the single-chain regime at four different densities. It shows how the linear regime at higher densities becomes sublinear at lower densities.

The values of (α, β) are $(2.922, 0.274)$ for $i = 1$ and $(1.895, 0.216)$ for $i = 2$ when $\tilde{n}_e = 0.2$, $(9.320, 0.433)$ for $i = 1$ and $(7.345, 0.466)$ for $i = 2$ when $\tilde{n}_e = 0.5$, $(14.788, 0.473)$ for $i = 1$ and $(11.552, 0.501)$ for $i = 2$ when $\tilde{n}_e = 0.8$ and in each case the error is less than 1%.

From the study of the pair correlation function we conclude that at moderate ($\tilde{n}_e \leq 0.2$ for $\kappa = 1$) densities, the chain is melted at arbitrarily weak temperature. For higher densities the chain retains correlations up to higher values of the temperature but these values are less than those obtained by the MLC.

We noticed from the high density regime ($\tilde{n}_e > 1$), where we reach the multi-chain structure, that another semi-empirical criterion can be formulated using the pair correlation function. We observed that at the melting temperatures evaluated by MLC in the case of multi-chain structures the ratio of the height of the fifth peak in $g(x)$ above 1 ($H_5 - 1$) to the height of the first peak above 1 ($H_1 - 1$) is:

$$\frac{H_5 - 1}{H_1 - 1}(T_m) \approx 0.15 \quad (5.3)$$

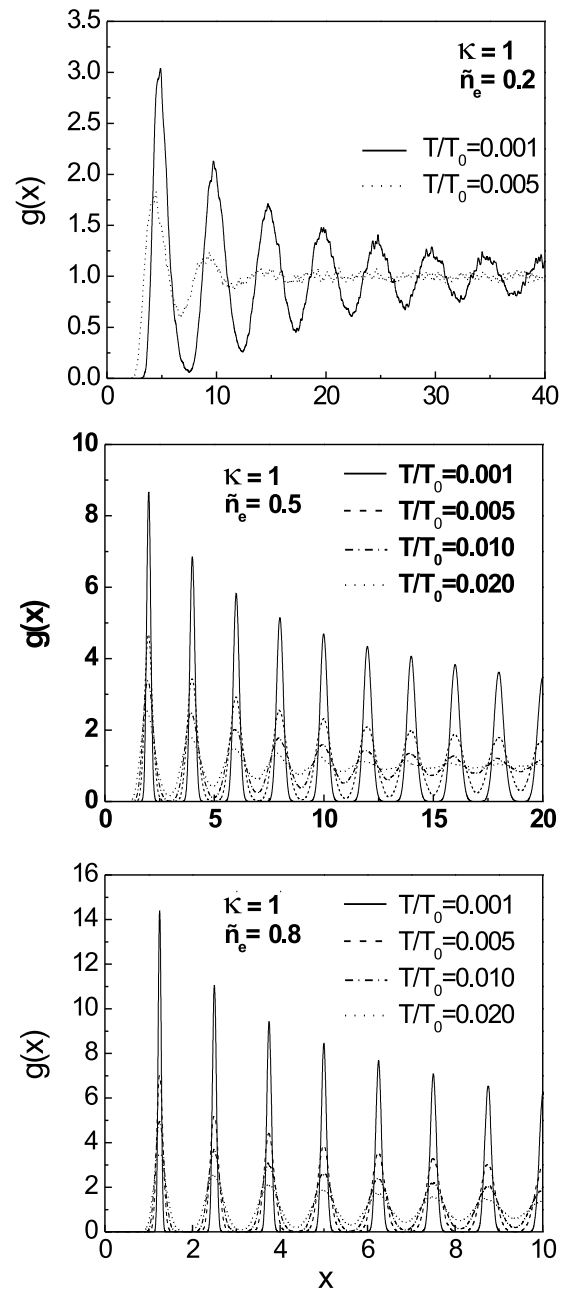


FIG. 5.8: The pair correlation function at different temperatures, for three different densities, for the single chain configuration.

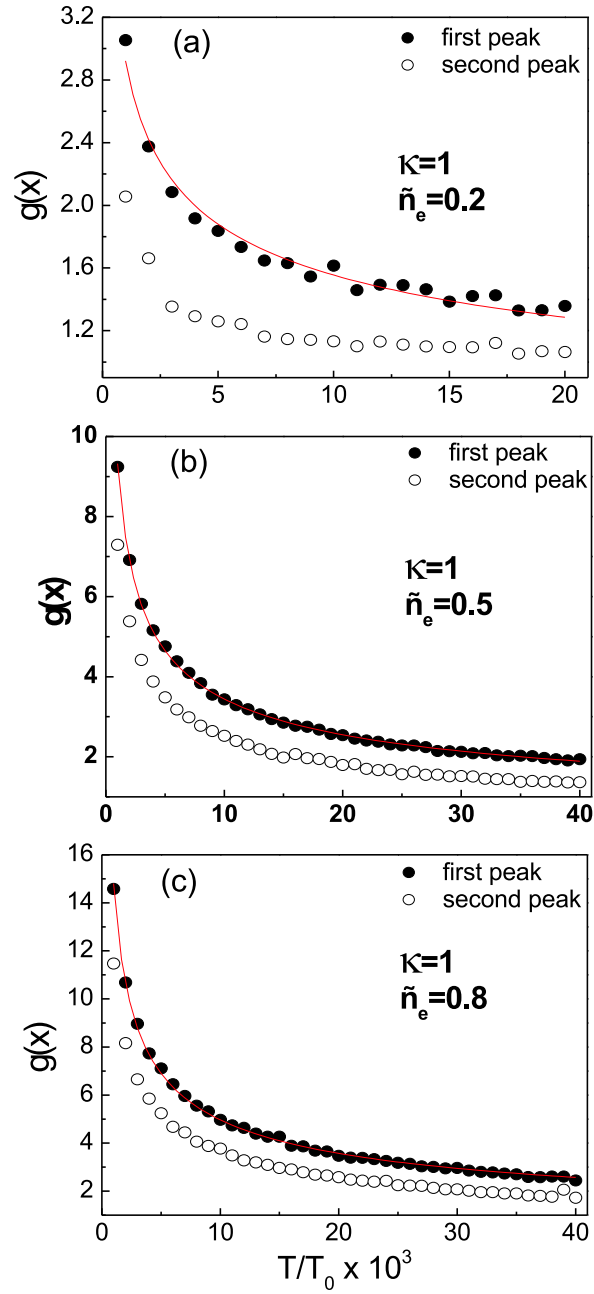


FIG. 5.9: The height of the first and second peaks of the pair correlation function for the single chain as a function of temperature for three different densities. The lines are the best fits with the function $\alpha(T/T_0)^{-\beta}$.

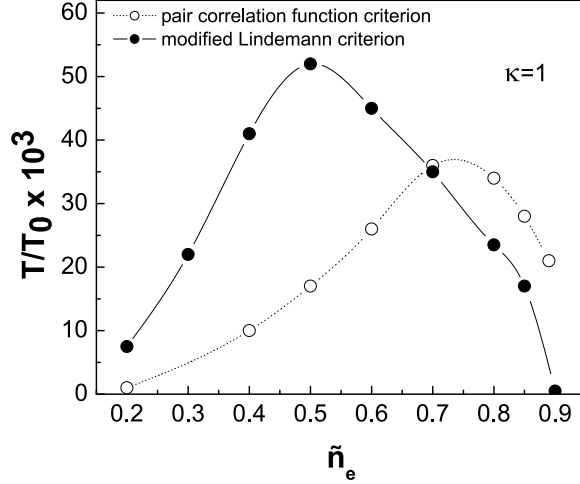


FIG. 5.10: The melting temperature for the single chain as obtained from the two complementary criteria.

Employing this criterion (termed as pair correlation function criterion or PCFC) in the single chain case in analogy to the multi-chain case, we obtain the results of Fig. 5.10, where we present both the relevant temperatures obtained by MLC and PCFC.

It is worth to notice that PCFC criterion does not work well at densities close to the structural transitions from $1 \rightarrow 2$ chains. The reason is that inter-particle spacing is relatively small and then the pair correlation function still measures correlations at certain distances and, most importantly, the height of the first peak is substantially reduced which artificially enhances the ratio (5.3). Thus the value of 15% which works far from the structural transitions is too high for the regime close to the structural transitions. It is therefore evident that the two criteria can work in a complementary manner.

5.3 COMPARISON WITH EXPERIMENT

An important experimental system, for which the melting temperature can be measured to signal indirectly the formation of the WC phase, are electrons floating on liquid helium, as illustrated in Chapter 1 (Sec. 1.2.1). It is possible to achieve relatively narrow Q1D channels on very stable suspended helium films over structured substrates and by that to obtain Q1D system [33, 151].

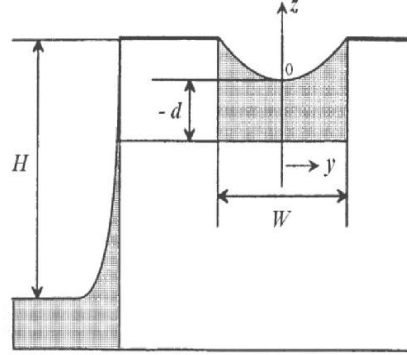


FIG. 5.11: Schematics of the helium profile in a narrow channel filled by liquid helium.

Assuming a semicircular profile of the liquid surface across the channels, then the confining potential is parabolic near the bottom with $\omega_0 = (eE_{\perp}^*/mR)$ [151], where E_{\perp}^* is the effective holding electric field in the case of the substrate and R the radius of the semicircular profile. This is illustrated in Fig. 5.11. Assuming a radius of approximately $5 \mu m$, a typical value for $E_{\perp}^* \approx 10 kV/cm$, then $\omega_0 \approx 10^{11}$ Hz. This in turn produces a $T_0 \approx 60 K$. The melting temperatures which have been obtained in the present work are of order $10^{-2} \times T_0$ which results in a melting temperature $\approx 0.5 - 1 K$, a temperature range which is routinely achieved in such experiments. Assuming an inter-electron distance of approximately $0.1 \div 1 \mu m$ leads to a dimensionless linear density $\tilde{n}_e \approx (0.5 \div 3)l$, where l is the number of chains. The dilute limit gives the same \tilde{n}_e as the one investigated in the present chapter.

5.4 CONCLUSIONS

In conclusion, we investigated melting of a classical Q1D system of particles interacting through a Yukawa-type potential in the range from Coulomb to very short range interaction in the case where the confinement is modeled by an external parabolic potential. In certain regions of the parameter space, there is evidence that melting starts first in the unconfined direction before the system melts along the inter-chain direction. Furthermore, we found that T_m shows a reentrant behavior as a function of the density of the system and a regime of frustration around each point of structural transition can be identified. In the case of the single chain structure, the melting shows different characteristics with respect to the multi-chain configurations. We devise a new criterion in

order to take into account the correlations at different temperatures in the single-chain case.

We focused on the principal features of melting for Q1D systems. There are, obviously, other issues connected with melting, which deserve interest and further investigations. One of those is the appearance of topological defects so that a KTHNY [142] scenario of two-stage melting is possible. In Ref. [63, 148, 155] this question was considered in the case of a circular confining potential with a finite number of particles. In the case of short range interactions the defects are pushed to the surface due to the large price for elastic deformations while in the Coulomb case shear and Young moduli are relatively small [148]. Moreover, because of the incommensurability of the circle with the hexagonal Wigner crystal the defects do not reside exactly at the borders but in a zone few lattice spacings inside the crystal. Therefore three different regimes with different melting temperatures can be detected [63]. In our case there is no such incommensurability and the edges can accommodate the defects easily. This has also been discussed in the case of a quantum Hall bar by Nazarov in Ref. [162].

Publications. The result presented in this chapter were published as:

- G. Piacente, I.V. Schweigert, J.J. Betouras, and F.M. Peeters, *Structural properties and melting of a low dimensional classical Wigner crystal*, Physica E **22**, 779 (2004) (4 pages).
- G. Piacente, I.V. Schweigert, J.J. Betouras, and F.M. Peeters, *Generic properties of a quasi-one-dimensional classical Wigner lattice*, Phys. Rev. B **69**, 045324 (2004) (17 pages).
- G. Piacente, I.V. Schweigert, J.J. Betouras, and F.M. Peeters, *Generic properties of a quasi-one-dimensional classical Wigner lattice*, Virtual Journal of Nanoscale Science and Technology, Vol. **9** (February 23, 2004).
- G. Piacente, I. V. Schweigert, J. J. Betouras, and F. M. Peeters, *Structural properties and melting of a quasi-one-dimensional classical Wigner crystal*, Solid State Commun. **128**, 57 (2003) (5 pages).

6

Driven systems with a constriction

Interacting systems, which tend to form periodic or ordered structures when the density of particles and the temperature are low enough (i.e. Wigner crystallization), can exhibit a remarkable variety of complex phenomena when they are driven by an external force. Understanding these phenomena, which arise from the interplay between periodicity, disorder, nonlinearities and driving, is often a hard task. For numerous such experimental systems, transport experiments [111, 171, 172] are a useful way to probe the physics (and sometimes the only way when direct methods, e.g. imaging, are not available). It is thus an interesting and challenging problem to obtain a quantitative description of their non-linear dynamics. This is why in this chapter we will study the properties of the model systems, introduced in the previous chapters, when an external driving force is applied and a constriction is present.

We address the question of the properties of strongly correlated Q1D systems under the effect of confinement, constriction potential, thermal noise and external driving force acting in the unconfined direction. Our classical model is very ductile because of its scalability and it is suitable for the description of diverse confined systems, as electrons on liquid helium, colloids and complex plasmas. Thus, the results of this chapter are quite general. Most of the theoretical, numerical and experimental works have concentrated the attention on moving 2D or 3D lattices and glasses (see Ref. [101] and references therein), thus for

mesoscopic driven systems the effect of confinement has not yet been deeply investigated and many aspects of the problem need a better understanding.

We focus on the static and, above all, on the dynamical behavior (i.e. the response of the system when an external drive is applied) in the presence of a local constriction. We perform Monte Carlo simulations, as in Chapter 3, in order to investigate static properties and Langevin molecular dynamics simulations, for different values of the driving force and for different temperatures, in order to investigate dynamical properties. Friction together with the constriction pins the particles up to a critical value of the driving force. Pinning, i.e. the fact that at low temperature there is no macroscopic motion unless the driving force f reaches a threshold critical value f_c , is a striking feature of driven system in the presence of disorder, as discussed in Chapter 1. There is a quite extensive literature about the dynamical properties near the depinning threshold [103, 173, 174], mostly in the context of CDW [104–106].

We show that driven Q1D systems can depin both in the elastic regime or in a new regime, that we term *quasi-elastic* regime, depending on the strength of the constriction. The quasi-elastic depinning is a new feature related to the low dimensionality (i.e. the external parabolic confinement acting along one direction) and to the kind of constriction. The dc conductivity is zero in the pinned regime, it has non-ohmic characteristics after the activation of the motion and then it is constant, so that the response of our Q1D system to an external drive is linear only for large values of the driving force. Furthermore, we investigate in detail the dependence of the conductivity with temperature and strength of the constriction. Interesting differences between the single and the multi-chain configurations arise as the temperature is increased.

Our results are valid in the classical regime, when particles can be considered as localized. Remarkable works on the quantum transport and pinning in the presence of weak disorder, where it is shown that quantum fluctuations soften the pinning barrier and charge transfer occurs due to thermally assisted tunneling, are described, for instance, in Ref. [138].

The chapter is organized as follows: we first give an overview of the model and of the numerical methods used. Then we describe the zero temperature phase diagram in the absence of any external driving force, stressing the differences, that come out because of the presence of the constriction, with respect to the results of Chapter 3. Subsequently we discuss the dynamics of the system, in particular we concentrate on the velocity vs applied driving force curves and on the conductivity. We analyze the interplay between driving force, thermal disorder and constriction potential, focusing on the difference between the single chain and multi-chain regime. Finally, we comment on the analogies and differences between our classical Q1D system and the cases of moving lattices and glasses and of other models in which quenched disorder or pinning potentials are present.

6.1 MODEL AND METHODS

We now consider the effect of a constriction on the system described by the Hamiltonian 3.1. As in the previous chapters, the system consists of an infinite number of classical identical particles with charge q and mass m , moving in a plane with coordinates $\mathbf{r} = (x, y)$. The particles interact through a screened Coulomb (Yukawa-type) potential and a parabolic confining potential in the y -direction is present. We impose a constriction potential with Lorentzian shape in the origin of the axes, thus the Hamiltonian of the system is given by:

$$H = \frac{q^2}{\varepsilon} \sum_{i>j} \frac{\exp(-|\mathbf{r}_i - \mathbf{r}_j|/\lambda)}{|\mathbf{r}_i - \mathbf{r}_j|} + \sum_i \frac{1}{2} m \omega_0^2 y_i^2 + \sum_i \frac{V_0}{1 + \alpha^2 x_i^2}, \quad (6.1)$$

where ε is the dielectric constant of the medium the particles are moving in, ω_0 measures the strength of the confining potential, V_0 is the maximum of the potential of the constriction which has a full width at half maximum $2/\alpha$. By the scaling transformations defined by Eq. (2.8a) and Eq. (2.8b), we obtain:

$$H' = \sum_{i>j} \frac{\exp(-\kappa|\mathbf{r}'_i - \mathbf{r}'_j|)}{|\mathbf{r}'_i - \mathbf{r}'_j|} + \sum_i y_i'^2 + \sum_i \frac{V'_0}{1 + \alpha'^2 x_i'^2}, \quad (6.2)$$

where $H' = H/E_0$, $\kappa = r_0/\lambda$, $\vec{r}' = \vec{r}/r_0$, $V'_0 = V_0/E_0$ and $\alpha' = r_0\alpha$.

The dimensionless time and temperature, which are essential quantities in what follows, are respectively $T' = T/[k_B(m\omega_0^2 q^4/2\varepsilon^2)^{1/3}]$ and $\tau = t\omega_0$.

The zero temperature configurations for different densities, namely different number of particles, and different values of the parameters in the Hamiltonian are calculated by the MC technique using the standard Metropolis algorithm as it was done in Chapter 3. We have allowed the system to approach its equilibrium state at some temperature T , after executing $10^5 \div 10^6$ Monte Carlo steps. The simulated annealing technique was used to reach the $T = 0$ equilibrium configuration. We introduced periodic boundary conditions along the x -direction in order to simulate an infinite long wire. We used typically a simulation cell of length $L = 100$ (in dimensionless units) centered around the origin of the axis. This choice was motivated by the fact that for larger L the changes in static and dynamical properties are negligible, especially for $\alpha' \geq 0.5$ and $\kappa \geq 1$.

Because of the presence of the constriction we found many more metastable states, which complicates the numerical approach. We will elaborate on this point in the next section.

After reaching the $T = 0$ equilibrium configuration, we introduced an external electrical field in the x -direction, or in other words we considered the effect of an external driving force f and calculate the transport properties of the system. We also considered the effect of temperature and thermal noise, coupling the system to additional degrees of freedom [120, 175] or to a heat

bath. The Langevin dynamics [176] is the most appropriate one to include such effects, as it has been pointed out in Chapter 2. The Langevin equations for the x and y component of motion in dimensionless units are respectively:

$$\frac{d^2 x'_i}{d\tau^2} = -\gamma \frac{dx'_i}{d\tau} - \frac{1}{2} \sum_j \frac{\partial}{\partial x'_i} \frac{\exp(-\kappa |\mathbf{r}'_i - \mathbf{r}'_j|)}{|\mathbf{r}'_i - \mathbf{r}'_j|} + \frac{V'_0 \alpha'^2 x'_i}{(1 + \alpha'^2 x'^2_i)^2} + \xi_x(T') + f \quad (6.3a)$$

$$\frac{d^2 y'_i}{d\tau^2} = -\gamma \frac{dy'_i}{d\tau} - \frac{1}{2} \sum_j \frac{\partial}{\partial y'_i} \frac{\exp(-\kappa |\mathbf{r}'_i - \mathbf{r}'_j|)}{|\mathbf{r}'_i - \mathbf{r}'_j|} - y'_i + \xi_y(T') \quad (6.3b)$$

where γ is the friction coefficient, which is an external parameter as well as κ , and $\xi(T')$ is a random force, reproducing the thermal noise, with zero average and standard deviation

$$\langle \xi_{ix}(\tau) \xi_{jy}(\sigma) \rangle = \gamma T' \delta_{ij} \delta_{xy} \delta(\tau - \sigma).$$

The driving force f and the random force ξ are measured in units of $m\omega_0^2 r_0$, while the friction coefficient γ is measured in units of ω_0 . We used the same simulation cell and the same boundary conditions as in the case of the MC simulations. It should be noticed that in the case of colloids [99] or vortices in type II superconductors [177] the motion is overdamped and Eqs. (6.3a) and (6.3b) are simplified: the hydrodynamic interactions can be neglected and Eqs. (6.3a) and (6.3b) reduce to a system of coupled first order differential equations.

We consider here the more general problem, including also the hydrodynamic terms. In order to integrate the equations of motion we used a quasi-symplectic algorithms of "leap frog" type [178] (see Chapter 2, Sec. 2.4.1 and 2.4.2) in the form:

$$\begin{aligned} \tilde{r}_i &= r_i(t) + \frac{\Delta t}{2} v_i(t), \\ v_i(t + \Delta t) &= c_2 \left[c_1 v_i(t) + \Delta t \frac{\partial H}{\partial r_i}(\tilde{r}_i) + d_1 \eta_i \right], \\ r_i(t + \Delta t) &= \tilde{r}_i + \frac{\Delta t}{2} v_i(t + \Delta t), \end{aligned}$$

where Δt is the time step, and η_i are Gaussian variables with standard deviation equal to 1 and average equal to 0. In order to generate Gaussian quantities satisfying these requirements we used the Box-Muller transformations, which are defined as follows: if ζ and φ are random numbers with uniform and independent distribution between 0 and 1, then ν and ζ , given by

$$\begin{aligned} \nu &= \sqrt{2 \ln \zeta} \cos(2\pi\varphi); \\ \vartheta &= \sqrt{2 \ln \zeta} \sin(2\pi\varphi), \end{aligned}$$

have a normal distribution with mean value equal to 0 and variance equal to 1.

The constants c_1 , c_2 and d_1 are given respectively by:

$$\begin{aligned} c_1 &= 1 - \frac{\gamma\Delta t}{2}, \\ c_2 &= \frac{1}{1 + \gamma\Delta t/2}, \\ d_1 &= \sqrt{\gamma T' \Delta t}. \end{aligned}$$

It was shown that this integration scheme has a good stability and runs rather fast, furthermore it is well behaved in the limit $\gamma \rightarrow 0$ [127].

The driving force was increased from zero by small increments. A time integration step of $\Delta\tau = 0.001$ was used and averages were evaluated during 2×10^5 steps after 2×10^6 for equilibration.

6.2 GROUND STATE CONFIGURATIONS

The ground state configuration is the result of competitive effects, that is the electrostatic repulsion, the confining potential that tries to keep the particles close to the x axis and the Lorentzian constriction potential that prevents the particles from settling close to the y axis. In Fig. 6.1 the contour plots of the sum of both confining and constriction potentials for two different values of V'_0 are shown. Depending on the values of (increasing) V'_0 and (decreasing) α' the saddle point at $(x, y) = (0, 0)$ becomes more pronounced.

As seen in Chapter 3, in the absence of any constriction the charged particles crystallize in a number of chains. Each chain has the same density resulting in a total one-dimensional density \tilde{n}_e . If a is the separation between two adjacent particles in the same chain, it is possible to define a dimensionless linear density $\tilde{n}_e = lr_0/a$, where l is the number of chains. In the case of multiple chains, in order to have a better packing (or in other words to minimize the interaction energy by maximizing the separation among particles in different chains), the chains are staggered with respect to each other by $a/2$ in the x -direction.

In the presence of the constriction potential the ground state configurations are modified near the constriction (see Fig. 6.2), but the particles are still organized in chains far away from this constriction. Close to the saddle point the particles do not arrange themselves in ordered chains. The particles near the constriction lead to a significant increase of the number of metastable states. Consequently the procedure of simulated annealing has to be more accurate than in the case of the absence of a constriction, which means that several intermediate temperature steps have to be considered. Sometimes the MC simulations do not provide us with the "exact" ground state, as it is seen for instance in Fig. 6.2 (c), (f) and (j), where the final configurations are not

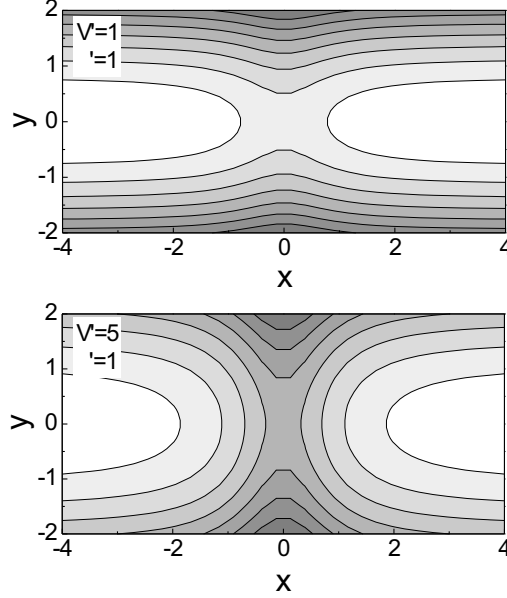


FIG. 6.1: Contour plots of the sum of the confinement and constriction potentials for two different values of the parameters: (a) $V'_0 = 1, \alpha' = 1$, (b) $V'_0 = 5, \alpha' = 1$.

perfectly symmetric with respect to x and y , while this is expected because of the symmetry of the Hamiltonian.

When the full width at half maximum of the constriction potential is short enough ($\alpha' \geq 0.5$), or in other words the effect of the constriction is significant only in a narrow region around $x = 0$, it is still possible to define a local density because the system exhibits a homogeneous spacing among charged particles except in the vicinity of the saddle point. Thus, excluding these regions, it is still meaningful to consider $\tilde{n}_e = lr_0/a$, where l is the number of chains. For smaller values of α , that is for larger interaction ranges of the constriction potential, the system is highly inhomogeneous and even shows coexistence of different chain phases (see Fig. 6.2 (d),(f) and (h)). In a certain sense the constriction introduces a local disorder into the system. In order to make these affirmations clearer, we plot in Fig. 6.3 the inverse interparticle spacing, i.e. the density, in the single chain configuration as a function of the distance from the origin of the coordinates for different values of κ and α' and $V'_0 = 1$. It is evident that the density is an increasing function of the inverse screening

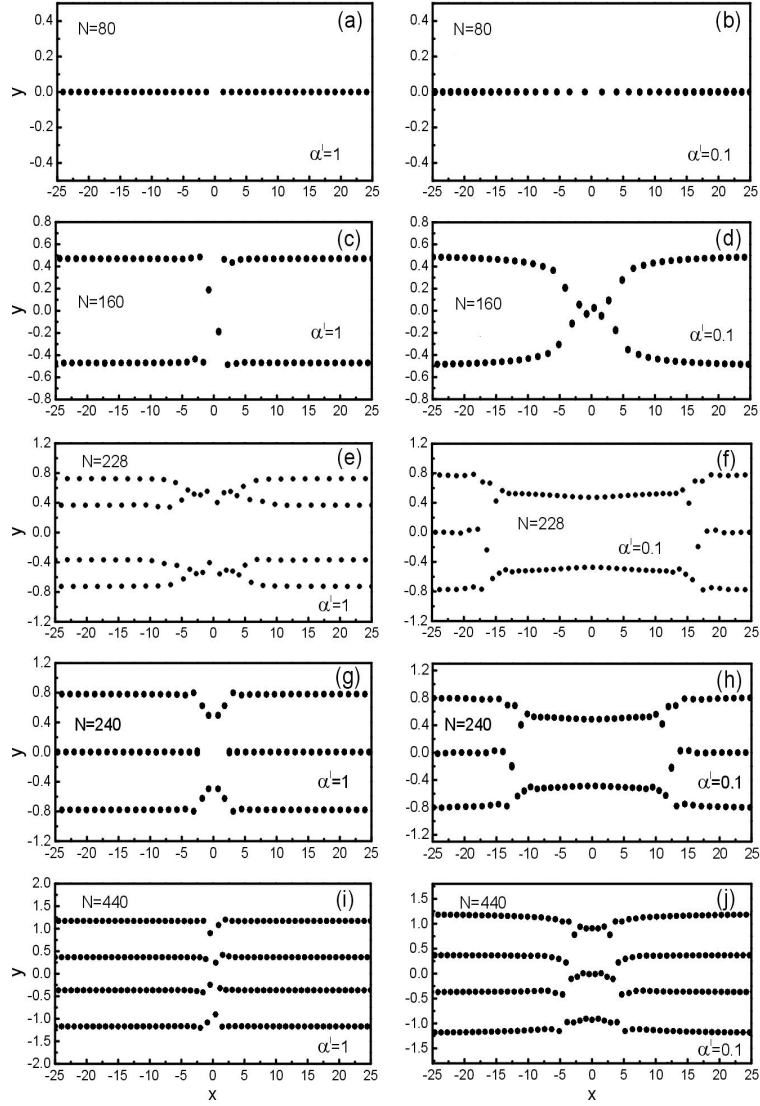


FIG. 6.2: The ground state configuration in the center of the simulation cell for $\kappa = 1$, $V_0' = 1$ and different values of the number of particles N in a simulation cell of length $L = 100$ and two different values of the constriction width. In the case of $\alpha' = 1$ the effect of the constriction potential is significant only around a narrow region around $(x, y) = (0, 0)$, while for $\alpha' = 0.1$ it is appreciable all along the length of the simulation cell. It is interesting to notice that for $\alpha' = 1$ the reentrant behavior of Chapter 3, with the four chain arrangement stabilized before the three chain arrangement, is still present, while it is absent for $\alpha' = 0.1$. For small values of α' the configurations are highly inhomogeneous.

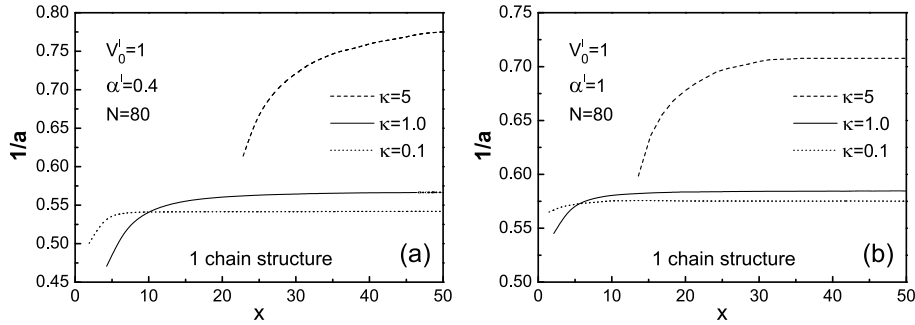


FIG. 6.3: The density as a function of the distance from the origin in the single chain configuration for 80 particles, for a large (a) and short (b) interaction range of the constriction potential. Because of the symmetry of the system around $y = 0$ only the results in the right part of the simulation cell are reported.

length κ , because the particles can stay closer together as the electrostatic repulsion is weaker. For small values of α' the density is an increasing function of the distance over a large range of x -values (Fig. 6.3(a)), while for $\alpha' = 1$ (Fig. 6.3(b)) this range can become very small and the density becomes very quickly x independent. Notice that for $x \rightarrow \infty$ the chain density should become independent of the parameters of the constriction.

6.3 DYNAMICAL PROPERTIES

When a constant electrical field E is applied to the system in the x -direction, it produces a longitudinal driving force f . The charged particles then are pushed along the direction of the driving force. In what follows we consider mainly systems for which $\kappa = 1$ and $\gamma = 0.2$, which are typical values for the inverse screening length and friction respectively, encountered in complex plasmas [51]. We also fixed the value of $\alpha' = 1$, that means that we deal with short range constrictions.

The first obviously important quantity to determine is the velocity v' as a function of the applied force f . In the absence of thermal fluctuations, i.e. $T = 0$, and in the absence of the constriction potential, Eqs. (6.3a) and (6.3b) become:

$$\frac{dv_i^x}{d\tau} = -\gamma v_i^x - \frac{1}{2} \sum_j \frac{\partial}{\partial x_i'} \frac{\exp(-\kappa|\mathbf{r}_i - \mathbf{r}_j|)}{|\mathbf{r}_i - \mathbf{r}_j|} + f; \quad (6.4a)$$

$$\frac{dv_i'^y}{d\tau} = -\gamma v'^y - \frac{1}{2} \sum_j \frac{\partial}{\partial y_i'} \frac{\exp(-\kappa|\mathbf{r}_i - \mathbf{r}_j|)}{|\mathbf{r}_i - \mathbf{r}_j|} - y_i'. \quad (6.4b)$$

Furthermore, because in the equilibrium configuration the net force acting on every particle, due to electrostatic repulsion and confinement, is zero, that is

$$\begin{aligned} \frac{1}{2} \sum_j \frac{\partial}{\partial x_i'} \frac{\exp(-\kappa|\mathbf{r}_i - \mathbf{r}_j|)}{|\mathbf{r}_i - \mathbf{r}_j|} &= 0; \\ \frac{1}{2} \sum_j \frac{\partial}{\partial y_i'} \frac{\exp(-\kappa|\mathbf{r}_i - \mathbf{r}_j|)}{|\mathbf{r}_i - \mathbf{r}_j|} + y_i' &= 0, \end{aligned}$$

Eqs. (6.3a) and (6.3b) can be ulteriorly simplified and one obtains the uncoupled equations:

$$\frac{dv'^x}{d\tau} = -\gamma v'^x + f; \quad (6.5)$$

$$\frac{dv'^y}{d\tau} = -\gamma v'^y, \quad (6.6)$$

whose stationary solutions are respectively:

$$v'^x = \frac{f}{\gamma}; \quad (6.7)$$

$$v'^y = 0. \quad (6.8)$$

This shows that in the absence of thermal noise and constriction the total effect of the external driving force is a sliding of the ordered structure with a drift velocity which is directly proportional to the driving force and inversely proportional to the friction. More in general, when the leading term in the equation of motion is the driving force, one should expect that the drift velocity is $v'^x = f/\gamma$, or in other words that the system behaves like a classical two-dimensional Drude conductor [179]. This feature has been observed in experiments [33] and in numerical simulations [107].

6.3.1 Pinning

The system is pinned until the applied driving force reaches a threshold value f_c . The pinned structures in the presence of the driving force shows substantial differences from the ground state configurations in the absence of a driving force. The particles move in the direction of the driving force and accumulate in front of the constriction, that exerts a force, which is opposite to the driving force. If $f < f_c$, new static configurations are reached, in which the electrostatic

repulsion and the repulsive force due to the constriction balance the driving force. The situation is depicted in Fig. 6.4, where the driving force is in the positive direction of the x axis. In the case of low constriction barrier height, the chain structures are homogeneous, although the inter-chain distances in the case of multi-chain structures are larger at the left than to the right of the constriction, because there are more particles at the left of the constriction barrier due to the driving force and, thus, a strongest electrostatic repulsion among them. In the case of high constriction barrier, the chain structures are no longer homogeneous. As can be seen in Fig. 6.4, different number of chains can coexist in the same configuration. As the energy for the particles to overwhelm the barrier is quite large, they tend to accumulate at $x < 0$, which produces a density gradient and consequently a splitting into a larger number of chains where the density is larger, because obviously in such a case the electrostatic repulsion among particles is larger.

It should be noticed that the nature of pinning for the system under investigation is very different from the usual pinned system found in the literature. Usually the pinning is the result of some kind of disorder (in most cases quenched disorder) or, in other words, the effect of the substrate. It is introduced into the system and modeled as randomly placed point-like pinning centers producing an attractive gaussian potential [107, 109, 180–182] or as randomly placed parabolic traps [99]. Thus, the pinning has usually an attractive nature. In our case, the pinning is the effect of a constraint, the particles have not enough energy to overcome the constriction barrier and consequently there is no net motion. Contrarily to the usual pinning the pinning in our system is of a repulsive nature.

In Fig. 6.4, the trajectories of the particles are reported for a temperature $T' = 0.002$, well below the melting temperature. It is interesting to study for a fixed number of particles and for a fixed temperature how by increasing the driving force the configurations change. The variation of the density along the constriction is shown in Fig. 6.5 for different values of the external driving force for a constriction height of $V'_0 = 5$ and width $\alpha' = 1$. Increasing the driving force more and more particles accumulate to the left of the constriction barrier in the direction of the driving force, corresponding to larger and larger densities. The density \tilde{n}_e has a discontinuity at the constriction. For low values of the driving force, except in the vicinity of the constriction, \tilde{n}_e is almost constant. But for larger values of the driving force it is always an increasing function of the distance along the simulation cell, except close to the constriction.

Increasing T' , we observed larger and larger oscillations of the particles until the system is melted. As already illustrated in Chapter 5, also in this case we observed larger oscillations in the x -direction than in the y -direction, which is evidently a combined effect of the confining potential and the nature of the inter-particle interaction. In the case of high temperature, close to the solid-liquid transition, and mainly in the case of large V'_0 the arrangements of the particles are slightly different from the ones shown in Fig. 6.4. Because, a high

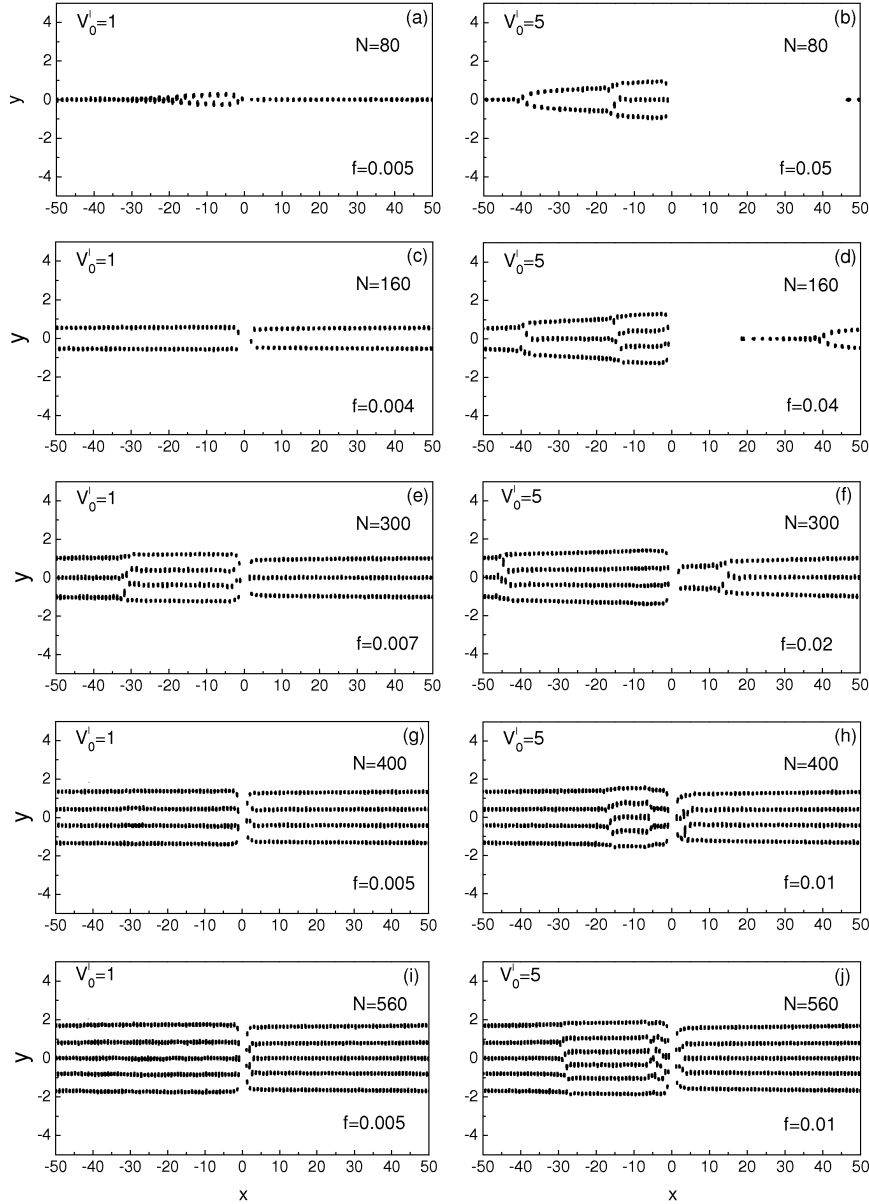


FIG. 6.4: Typical trajectories of the particles when the system is pinned for different number of particles N in a simulation cell of length $L = 100$ and different values of the height of the constriction barrier. The plots are for a temperature $T' = 0.002$, $\kappa = 1$ and $\alpha' = 1$.

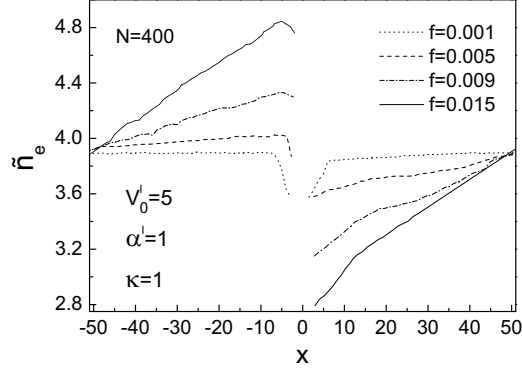


FIG. 6.5: The density as a function of the distance along the simulation cell for different values of the driving force and for a temperature $T' = 0.002$.

V_0' and in combination of the driving force produce a density gradient in the chain-like structures, the melting is not homogeneous, with the coexistence of solid and liquid regions. It is beyond the aim of the present study to discuss how the driving force induces local melting of the system.

The critical force f_c is evidently a function of the temperature T' , it decreases with increasing temperature, that is the thermal motion aids the net motion of the particles. The critical force is also a function of the density, i.e. the number of particles. In our simulations we observed that for larger densities f_c becomes smaller.

6.3.2 Depinning

When the driving force f is larger than the threshold f_c , the system exhibits 1D flow. In Fig. 6.6 some typical trajectories of the depinned particles are reported, for $T' = 0.002$ and different values of f just above f_c .

The first interesting observation is that the driven system does not break up into pinned and flowing regions, as observed in experiments and simulations of superconducting vortices [183–185] or colloids [99], or, in other words, the chain-like system under investigation does not exhibit *plastic depinning*. Once the driving force overwhelms the critical threshold f_c , all the particles move together. The depinning can be either *elastic* or *quasi-elastic* depending on the height of the constriction barrier. In the case of a low barrier ($V_0' = 1$ in Fig. 6.6) the particles move such that they keep the same neighbors, thus the system depins elastically. In contrast in the case of a high barrier ($V_0' = 5$ in

Fig. 6.6) a complex net of conducting channels is activated and the particles move without keeping their neighbors, that is the depinning is quasi-elastic.

The region after the constriction barrier, as is evident from the trajectory patterns, shows features that deserve a deeper investigation in the case of high values of V'_0 . In Fig. 6 for $V'_0 = 5$ at the right of the constriction some noise is present and the particles flow disorderly. In order to explain this behavior we investigated the distributions of the x and y components of the velocity in narrow strips along the simulation cell length. We concentrated our attention on a system of $N = 400$ particles at $T' = 0.002$, with $\kappa = 1$, $V'_0 = 5$ and $\alpha' = 1$. The results are reported in Fig. 6.7.

It is evident that v_y is always normally distributed with average equal to zero, as expected, because it receives contributions mainly from thermal noise, which is gaussian. The distribution of v_x is still gaussian, but centered around a value $\langle v_x \rangle \neq 0$ because of the external driving force, except in the neighborhood of the constriction where the strong interaction with the barrier gives a non-gaussian profile to it. What is interesting is the fact that the velocity above the depinning threshold has a pronounced gradient in the x -direction. From Fig. 6.7, it is clear that approaching the constriction from the left side the particles are slowed down; they receive a sudden acceleration when they pass the constriction barrier, then the velocity has a maximum in the right neighborhood of the constriction and finally it slows down again when approaching the edge of the simulation cell. In order to explain these highly non linear features, it is helpful to look at the profile of the force due to the constriction potential (see Fig. 6.8). This force has a significative magnitude only in a narrow region around $x = 0$. For $x < 0$ it acts oppositely to the driving force, while for $x > 0$ it enhances the driving force. There are two maxima for the intensity of the force located at $x = \pm 1/\sqrt{3}$ and it is zero at the origin of the axis. Therefore, when the particles approach the constriction they start to feel this decelerating force and slow down. Because the system is strongly interacting the deceleration is seen not only in the left neighborhood of the barrier, but in a wider region. At $x = 0$ the force is zero, for $x > 0$ close to the constriction the force quickly increases and adds to the driving force, so the particles experience a sudden acceleration which produces a large velocity. After that the particles are accelerated only by the driving force and start to feel the effect of the particles on the opposite side of the simulation cell because of the periodic boundary conditions, so the velocity decreases again. In the case of low constriction barriers or large driving forces the x components of the velocity are more homogenously distributed along the simulation cell. From the width of the velocity distribution it is possible to define an "effective temperature". According to the equilibrium probability factor

$$P \propto \exp \left[- \left(\frac{mv_x^2}{2k_B T_{eff}^x} + \frac{mv_y^2}{2k_B T_{eff}^y} \right) \right],$$

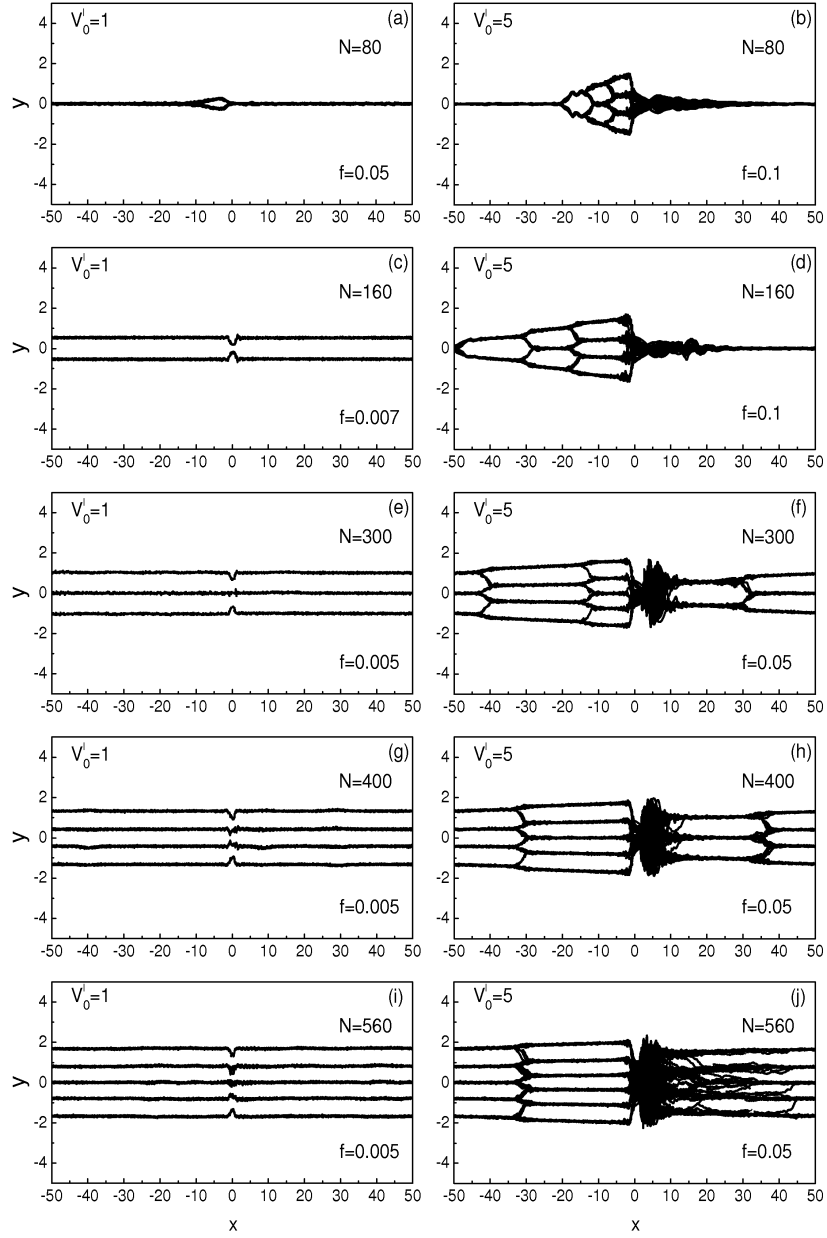


FIG. 6.6: Typical trajectories of the particles when the system is depinned for different densities and different values of the height of the constriction barrier. The plots are for a temperature $T' = 0.002$, $\kappa = 1$ and $\alpha' = 1$.

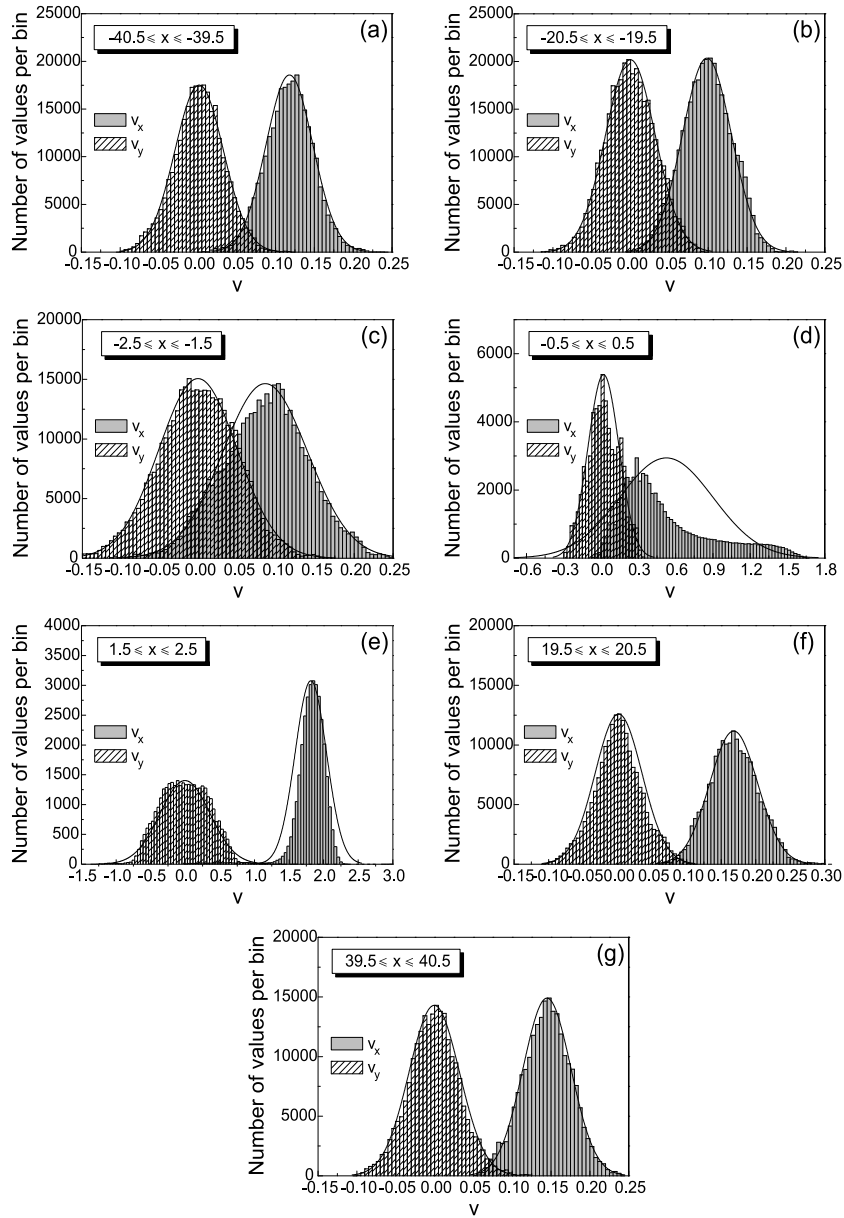


FIG. 6.7: The v_x and v_y distributions along the simulation cell length for a system of $N = 400$ particles, for $\kappa = 1$, $V'_0 = 5$ and $\alpha' = 1$ and for a temperature $T' = 0.002$ and driving force $f = 0.05$. The superimposed curves are the normal distribution curves generated using the mean and standard deviation of the data.

where T_{eff}^x and T_{eff}^y take into account also the contributions due to the potential energy, the fluctuations of the velocity components are related to the effective temperature by:

$$\begin{aligned} T_{eff}^x &= m \langle (v'_x - \langle v'_x \rangle)^2 \rangle / k_B, \\ T_{eff}^y &= m \langle (v'_y - \langle v'_y \rangle)^2 \rangle / k_B. \end{aligned}$$

In our dimensionless units and our specific case this yields:

$$\begin{aligned} T_{eff}^x &= 2 \langle (v'_x - \langle v'_x \rangle)^2 \rangle, \\ T_{eff}^y &= 2 \langle v_y'^2 \rangle, \end{aligned}$$

respectively. The calculated effective temperatures are reported in Table 6.1.

It is worth to notice that the effective temperatures are the same as the simulation temperature in the regions far away from the constriction barrier where the velocity fluctuations are nicely described by a normal distribution (see Fig.6.7). The effective temperatures T_{eff}^x and T_{eff}^y are increased when approaching the constriction. In the strips $-0.5 \leq x \leq 0.5$ and $1.5 \leq x \leq 2.5$ both T_{eff}^x and $T_{eff}^y \gg T'$. This is evidently a result of the strong interaction with the barrier which increases significantly the fluctuations in the velocity. Actually, the spreading of the distribution of the velocities is one to two orders of magnitude larger in the constriction region with respect to the regions where the constriction potential is almost zero.

In the elastic regime the velocity fluctuations could be fitted to a Gaussian distribution both for v_x and v_y , even in the vicinity of the constriction. Around the barrier, the strong interaction effect is felt as an increase of the effective temperature, which is much less pronounced than in the quasi-elastic regime.

Regarding to the noise observed in the trajectory plots, it is essentially due to the fact that the particles merge from the constriction with a relatively large y component of the velocity. As is seen from Fig. 6.7(d), the distribution of the v_y spreads over a quite large range of values while passing the constriction. Indeed, the standard deviation of the v_y distribution around $x = 0$ is one order of magnitude larger than in the other regions, as already mentioned. This feature is a consequence of the fact that very close to the barrier the constriction force is very small (it is zero at $x = 0$), the particles proceed slowly and, thereby, they strongly undergo the effect of the confining potential which accelerates them in the y direction, producing a significant y component of the velocity. This is also confirmed by the fact that passing the constriction barrier a narrowing of the chain structures is always present (see Fig. 6.6). Notice from Fig. 6.6(d,e) that the velocity fluctuation are no longer described by normal thermodynamic equilibrium distribution and that in particular for v_x there are large deviations.

<i>region</i>	T_{eff}^x	T_{eff}^y
$-40.5 \leq x \leq -39.5$	0.0018	0.0020
$-20.5 \leq x \leq -19.5$	0.0020	0.0021
$-2.5 \leq x \leq -1.5$	0.0060	0.0051
$-0.5 \leq x \leq 0.5$	0.28	0.031
$1.5 \leq x \leq 2.5$	0.14	0.26
$19.5 \leq x \leq 20.5$	0.0024	0.0023
$39.5 \leq x \leq 40.5$	0.0019	0.0021

Table 6.1: Effective electron temperatures corresponding to the situation of Fig. 6.6(h) in the different regions studied in Fig. 6.7.

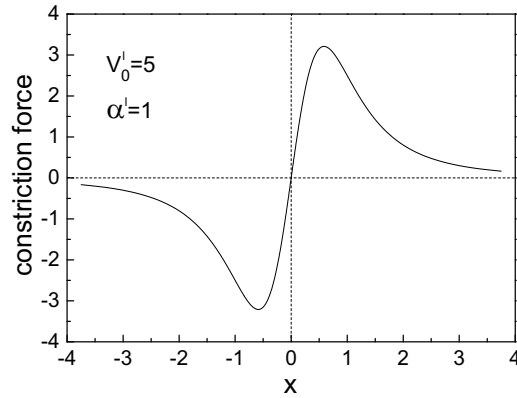


FIG. 6.8: The constriction force profile as a function of x for $V'_0 = 5$ and $\alpha' = 1$

The quasi-elastic depinning is a feature closely related to the repulsive nature of the constriction appearing when the strength of that potential is increased. In other systems of driven particles, where an attractive pinning potential is introduced, a crossover from elastic to plastic depinning with increasing strength of the pinning potential occurs [99].

As first predicted by Fisher the elastic depinning exhibits criticality [145] and the velocity vs force curves scale as $v = (f - f_c)^\beta$. This scaling has

been extensively studied in 2D CDW systems where $\beta = 2/3$ [186, 187]. It is, however, still an open issue whether this exponent is the signature of an universality class and whether it depends on the particle-particle interaction. Actually, in other investigations on elastic depinning of driven colloidal lattices the findings were $\beta \sim 0.5$ [188] and $\beta = 0.92 \pm 0.01$ [107]. Other studies on plastic depinning with filamentary or river-like flow have shown a velocity-force curve scaling with $\beta = 2.2$ [188], $\beta = 1.94 \pm 0.03$ [99] for colloids, $\beta = 2.0$ for electron flow simulations in metallic dots [189] and $\beta = 2.22$ for vortex flow in superconductors [180].

As pointed out by Le Doussal and Giamarchi, for an infinite size system true elastic depinning is not expected since dislocations and defects, acting as pinning centers, should appear at large scales [100]. Both the simulations and the experiments are, however, always for finite size systems and consequently the elastic depinning can be observed and the distance between dislocations may be larger than the system size.

In Fig. 6.9, we report the $v - f$ curve in the case of elastic and quasi-elastic depinning for different number of particles, i.e. for different chain arrangements. It should be noticed that the critical exponent does not depend on the number of chains in the system. For all the investigated chain configurations we obtained on average that $\beta \simeq 0.66$ in the case of homogeneous channel flow, that is elastic depinning, and $\beta \simeq 0.94$ in the case of inhomogeneous channel flow, that is quasi-elastic depinning. The value of the critical exponent could, therefore, be considered as a clear signature of the kind of depinning. Our results are consistent with the findings on CDW systems and colloids, mentioned before. With increasing temperature but below the melting temperature, we observed a broadening of the conducting channel or some changes in the structure with some chains collapsing (we will provide more details about this point in the next subsection), but no significant dependence of the critical exponent on temperature was found (within our fitting errors).

The question of whether in confined systems there is an universal exponent for elastic and quasi-elastic depinning cannot be answered conclusively. We found that the critical exponent are not affected by the value of κ , as it can be seen in Table 6.2: going from $\kappa = 0.2$ (nearly Coulomb interaction) up to $\kappa = 5$ (short range interaction), the value for the critical exponent stays the same. Although we found that the critical behavior is independent of the particle-particle interaction, further investigations with other kind of pinning potentials are required in order to affirm that the elastic, quasi-elastic and plastic depinning belong to different universality classes.

It is interesting to investigate the values of β , or in other word the kind of flow, as a function of V_0' . For colloidal systems a sharp crossover from elastic to plastic depinning was found with increasing strength of the substrate disorder, accompanied by a sharp increase in the depinning critical force [99]. Carpentier and Le Doussal studied theoretically the effect of quenched disorder on the order and melting of 2D lattices and found a sharp crossover from the ordered

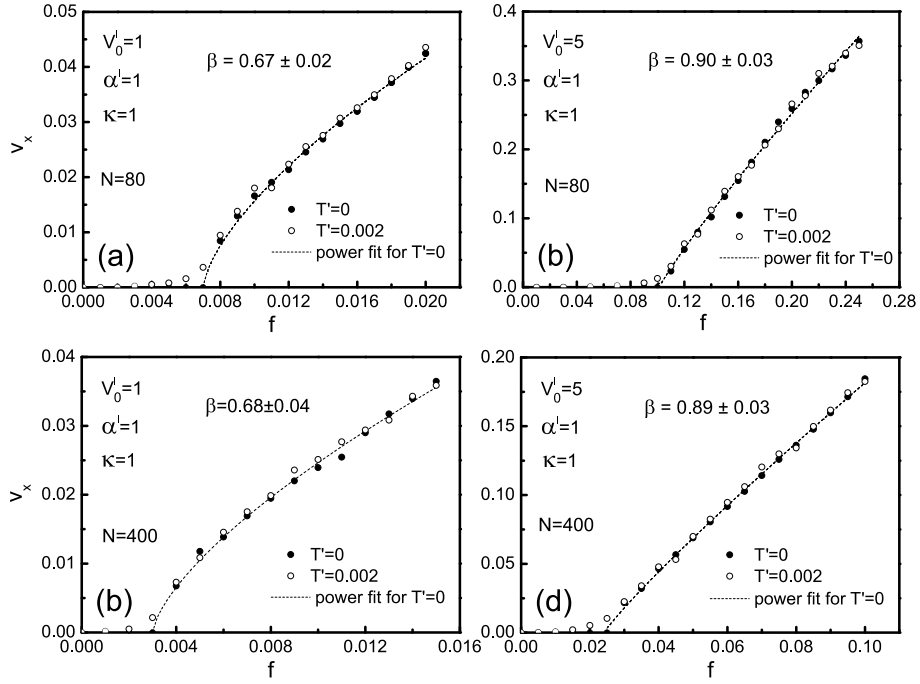


FIG. 6.9: Velocity v_x vs applied drive f for the elastic depinning ((a) and (b)), for the quasi-elastic depinning ((c) and (d)) for $\kappa = 1$ and $\alpha' = 1$. The dashed curves are the best fitted power law behavior for $T' = 0$. At zero temperature the curves exhibit a sudden jump at the depinning threshold, while at finite temperature they are smoother. The critical exponents are independent of the density, i.e. the number of chains.

Bragg glass (where there are no defects) to a disordered state [190]. They also predicted that the depinning threshold increases at the order to disorder transition due to the softening of the lattice, which allows the particles to better adjust to the substrate. A similar mechanism could account for the peak effect observed in vortex matter in superconductors [191], in which the depinning threshold rises abruptly with increasing applied magnetic field.

We found a crossover from elastic to quasi-elastic depinning as the barrier height of the constriction is increased. This is analogous to the crossover from the elastic to plastic flow encountered in other systems. As can be seen in Fig. 6.10, the behavior of β as a function of V'_0 is almost step-like, and the crossover takes place in a narrow range of V'_0 values. We also observed increasing values of the critical threshold f_c . It is beyond our scope to determine whether the elastic to quasi-elastic crossover is a first or second order transition and how

κ	V'_0	β	Depinning
0.2	0.25	0.68 ± 0.04	elastic
0.2	1	0.70 ± 0.06	elastic
0.2	5	0.95 ± 0.04	quasi-elastic
1	0.25	0.64 ± 0.03	elastic
1	1	0.67 ± 0.02	elastic
1	5	0.92 ± 0.05	quasi-elastic
2	0.25	0.65 ± 0.04	elastic
2	1	0.66 ± 0.03	elastic
2	5	0.96 ± 0.03	quasi-elastic
3	0.25	0.65 ± 0.03	elastic
3	1	0.95 ± 0.06	quasi-elastic
3	5	0.97 ± 0.05	quasi-elastic
5	0.25	0.67 ± 0.04	elastic
5	1	0.98 ± 0.06	quasi-elastic
5	5	1.02 ± 0.08	quasi-elastic

Table 6.2: The critical exponent β for different values of the inverse screening length κ and the constriction barrier height V'_0

temperature influences this transition. However, the relative smoothness of the curves in Fig. 10 suggests a possible second order transition. Furthermore, the effect of increasing temperature should reasonably result in a shift to lower values of f_c or V'_0 for the transition from elastic to quasi-elastic flow.

It is evident from Fig. 6.10 that the crossover shifts towards lower values of the potential barrier as the inverse screening length is increased, which means that the particles with stronger interparticle interactions can flow in a more ordered way.

We should stress that the physics behind the crossover from elastic to quasi-elastic depinning is different from the case of quenched disorder, where with increasing disorder strength the ordered structure is softened and particles can better adjust to the substrate. In our case the accumulation of particles in the vicinity of the constriction barrier and their mutual repulsion gives rise for

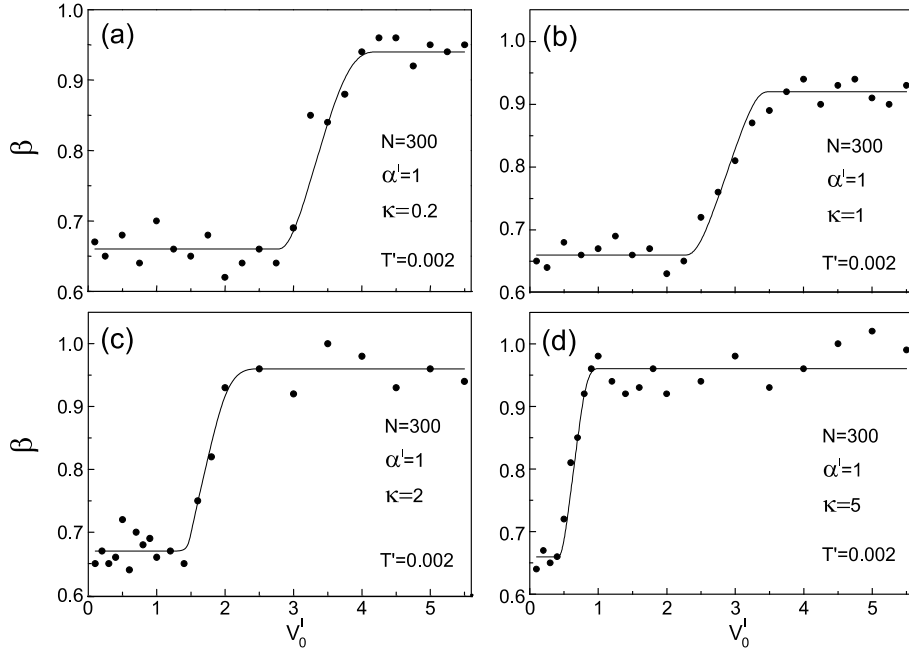


FIG. 6.10: The critical exponent β as a function of the constriction barrier height V_0' for different values of the inverse screening length: (a) $\kappa = 0.2$, (b) $\kappa = 1$ and (c) $\kappa = 5$. With increasing values of κ the crossover region shifts to lower values of V_0' . The solid lines are guides to the eye.

high values of V_0' to a complex arrangement of conducting channels, in which the nearest neighbors of each particle change, i.e to the impossibility of elastic flow.

In our simulation either in case of elastic and quasi-elastic depinning no history dependence was found. The velocity vs applied drive are not hysteretic, and we obtained the same result for increasing and decreasing values of f .

Finally, in the case of very small α , that is for a wide constriction interaction, because of the density gradient producing the coexistence of different chain structures, we always observed quasi-elastic depinning.

6.3.3 Conductivity

According to Ohm's law the current density of a classical system of charged particles is proportional to the applied electric field:

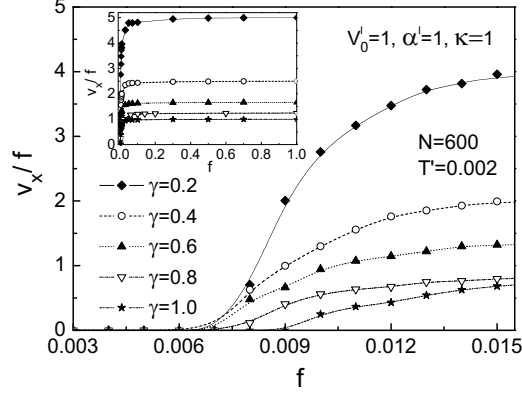


FIG. 6.11: The ratio between velocity and driving force as a function of the drive strength for different values of the friction coefficient. The conductivity is non-Ohmic in a narrow region above the depinning threshold. The inset shows that for larger values of f Ohm's law is fulfilled with the conductivity as a constant.

$$\mathbf{j} = \sigma \cdot \mathbf{E}, \quad (6.9)$$

where σ is the specific conductivity. The conductivity can be in general expressed as a second rank tensor. Because of the geometry of the investigated system and because the driving is in the x -direction, we are interested only in σ_{xx} , which we will refer in what follows as simply σ .

From the definition of j and from Eq. (6.7) it follows, in dimensionless units:

$$\sigma' = \tilde{n}_e \frac{v'_x}{f} = \frac{\tilde{n}_e}{\gamma}, \quad (6.10)$$

where $\sigma' = \sigma/(q^2/m\omega_0 r_0)$. As the definition of total density is not always an accurate one for our system, as mentioned above, we investigated the ratio v'_x/f , which is directly proportional to σ' through \tilde{n}_e and which is a constant equal to $1/\gamma$, according to Eq. (6.10). In Fig. 6.11 the results of our calculations are reported for different values of the friction.

When the particles are pinned the conductivity is obviously zero. It is interesting to notice that after the depinning threshold, there is a narrow region where the conductivity shows non-Ohmic features, going from zero to the saturation value $1/\gamma$. Afterwards when the drive is the leading effect in the equations of motion, the particles behave as a classical Ohmic conductor. This

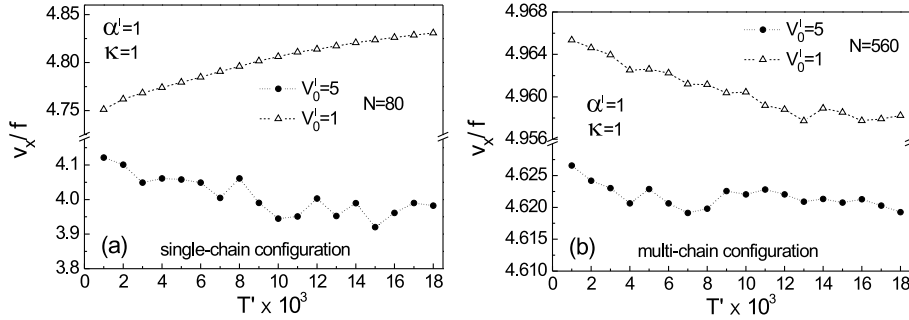


FIG. 6.12: Dependence of the conductivity on the temperature, for (a) a single-chain structure and (b) a multi-chain structure. For weak values of the potential barrier the conductivity of the single-chain structure is an increasing function of temperature, in all the other cases it shows a decreasing trend.

behavior is independent of the number of particles and of the height of the constriction barrier. For higher values of V_0' the non-Ohmic conductivity region is enlarged.

Studying the conductivity as a function of temperature some interesting features were observed. We investigated a rather wide range of temperatures from 0.001 to 0.018. From Chapter 5 we know that for the single chain configuration in the absence of driving and constriction potential, the melting temperature is arbitrarily low, while in the multi-chain configuration it is $T_m' \sim 0.015$. The results of our calculations, for a driving force $f = 0.05$ and for different values of V_0' , are sketched in Fig. 6.12.

The behavior in the single chain configuration shows substantial differences from the multi-chain one. First of all, for weak values of V_0' , the conductivity is an increasing function of T' in the single chain case, while it is decreasing in the multi-chain case. This means that when the number of particle is small, that is the electrostatic interaction is not too strong, the thermal motion aids the particle to overcome the potential barrier and does not act as a disturbance, while in the case of a large number of particles, the possibility of overcoming the barrier is sustained by the electrostatic repulsion and the thermal agitation is a dissipative factor. This is an ulterior confirmation that the dynamics of the system under investigation is a very complex interplay of driving, electrostatic interaction, repulsion from the constriction, thermal fluctuations and confinement.

In general, in a classical model of conduction the conductivity is expected to be a decreasing function of temperature. For large values of the constriction barrier height either in the case of single chain and multi-chain structures, we found that the conductivity is not a monotonic function of temperature,

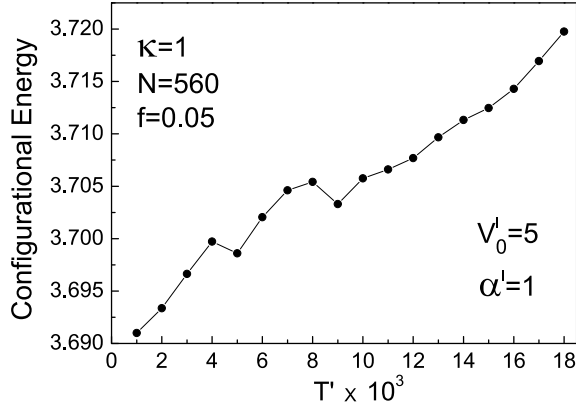


FIG. 6.13: The average configurational energy per particle as a function of the temperature for a multi-chain configuration.

although it shows a decreasing trend. The presence of structures in the v_x/f curve vs T' can be explained by the fact that with increasing temperature some of the channels formed for high V_0' can collapse together to form new channels, as mentioned in previous subsection. This is confirmed by the analysis of the configurational energy per particle as a function of temperature, which is plotted in Fig. 6.13.

The average potential energy exhibits the same temperature dependence as the conductivity, while in the case of a weak constriction barrier height the configurational energy per particle increases linearly with temperature. Another factor, which is also responsible for that non monotonicity, is the fact that, in the case of high barrier values, a density gradient is present and the melting is not homogenous, thus some parts of the system can be in the liquid state while others are still in the solid state, giving rise to complex phenomena in the transport properties.

6.4 OTHER DYNAMICAL PROPERTIES

For high values of the driving force the system shows the phenomenon of *dynamical reordering*. When the driving force is large the system, even in case of a high constriction barrier, can flow in an ordered channel structure. This is shown in Fig. 6.14. It is interesting to compare the trajectories of Fig. 6.14 with the one of Fig. 6.6(j). Above the depinning threshold (Fig. 6.6(j)) the channel structures are not homogenous, with increasing the drive (Fig. 6.14) an ordered moving structure is reached again.

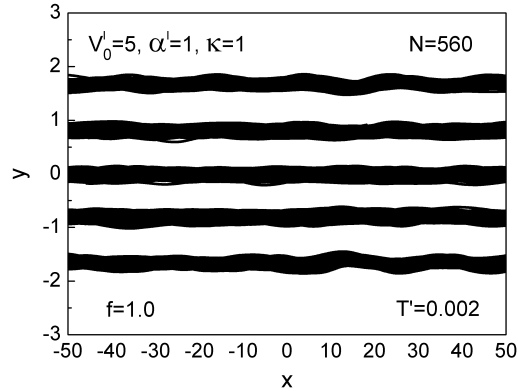


FIG. 6.14: Trajectories of a system of $N=560$ particles for a high value of the driving force. The five channel structure is attained over the whole wire (cfr. Fig. 6.7(j)).

This is a well known phenomenon. Indeed, it was observed experimentally for vortex lattices in type II superconductors [108] and for colloids [192]. The interplay between dynamical reordering and melting in mesoscopic channels was recently studied experimentally in the case of vortices, providing the first conclusive evidence for a velocity dependent melting transition [193]. The dynamical reordering was also investigated theoretically for CDW systems [145]. The dynamical reordering for such systems is originated by the fact that the applied driving force tilts the pinning potential thereby reducing the pinning strength. When a large enough force is applied, the particles depin and then flow quite orderly. The same mechanism is responsible for the dynamical reordering of the studied system, with the difference that the tilted potential is in this case the constriction potential.

It is worth to study the ratio between kinetic and potential energy, averaged at every simulation step, as a function of the temperature. From Fig. 6.15 it is evident that the kinetic energy increases faster than the configurational energy with temperature, which is an expected result. What is interesting is the fact that the fitting curve is of the type $y = a/(1 + bx)$. The fit is excellent with very small errors in the fitting parameters a and b .

Finally, we also investigated the distribution of the velocity v_x as a function of the distance from the x axis, or in other words we studied the velocity for each conducting channel when the system flows orderly. Motivated by the experimental findings of Ref. [33], that for a chain system of electrons on

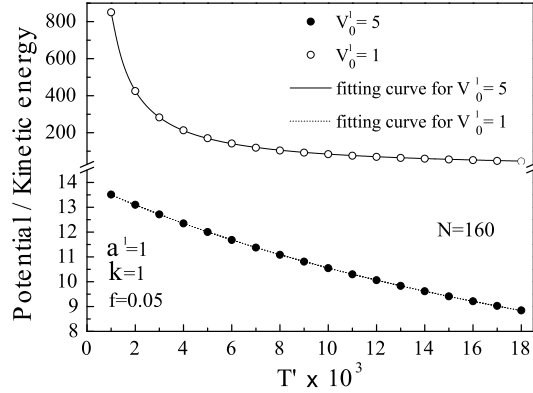


FIG. 6.15: The ratio between potential and kinetic energy per particle as a function of temperature.

liquid helium, the particles in the external chains have higher velocity than the particles in the internal chains, we tried to clarify whether in our system a similar behavior occurs. Our findings are in contrast with the one of Ref. [33], actually we found that the internal chains have on average a velocity which is 5% higher than the external chains. However, this discrepancy can be explained by the circumstance that the pinning mechanism are different for the two systems: the coupling between electrons and ripplons in case of Ref. [33] and the constriction potential in our case, and by the fact that the confinement potentials are not exactly the same in the two systems.

6.5 COMPARISON WITH OTHER DRIVEN SYSTEMS

A rather general theory of periodic structures in a random pinning potential under the action of an external driving force was developed by Le Doussal and Giamarchi [101]. Their findings were that the periodicity in the direction transverse to the motion leads to a different class of driven system: the moving glasses, with the decay of the translational long-range order as a power law. Similar considerations can be made for our system as well, but with the important difference that because of the confining potential and the constriction potential the periodicity is broken both in the x and y -direction. For weak constriction barrier height long-range translational order is present in the x -direction, but it is softened when the system is moving and the temperature is increased. For infinite systems one of the consequences of periodicity in the transverse direction to the motion is that particles flow along static channels

for uncorrelated and weak disorder and that there are barriers to transverse motion. In our confined system the barriers to transverse motion are an effect resulting from confinement instead of periodicity. Most of the studies on driven lattices or glasses show that, at finite but low temperature, the channels broaden and strong non-linear effects exist in the response to the applied drive, though the asymptotic behavior is found to be linear, which is, indeed, what we found as well.

In infinite moving systems with random pinning centers, depending on the strength of that disorder, two kinds of flow are possible: (i) the *elastic* one, where all the particles move keeping their neighbors, and (ii) the *plastic* one, where part of the particles are moving in river-like or filamentary structures and part is pinned. There is a sharp crossover from the elastic to the plastic flow, related to an order-disorder transition. In our system we found that two kinds of flow are possible: (i) the *elastic* flow, where all the particles move orderly and the nearest neighbors are preserved, and (ii) the *quasi-elastic* flow, where all the particles move together, but creating a complex net of conducting channels, for which the neighbors are not kept. We also found a cross over from the elastic to quasi-elastic flow, but the sharpness is not very pronounced. It is important to stress that this difference is closely related to the different pinning potentials considered. Generally the pinning potentials are attractive, in our case they are repulsive. To be more precise, in the case we investigated the pinning is due to a constraint rather than an actual pinning potential. That is the reason why we did not observe plastic flow, because particles cannot be strongly attracted and pinned by any pinning center.

What we consider really notable is the circumstance that the velocity vs driving force curve even in our confined system in the case of elastic depinning scales as $v \propto (f - f_c)^\beta$, with $\beta \sim 0.66$, which is in agreement with most of the theoretical and numerical works for infinite systems exhibiting elastic flow, where $\beta = 2/3$. Thus, the value of the critical exponent $\beta = 2/3$ seems actually the signature of elastic depinning independently of the confinement and the pinning potential. Naturally, in order to affirm this definitely more investigations are required with different topologies and potentials. Furthermore, in the case of quasi-elastic depinning we found a critical exponent $\beta \sim 0.94$, which is an intermediate value between the case of elastic and plastic flow, where the experimental findings give $\beta \sim 2$. This leads us to the conclusion that the quasi-elastic depinning is an intermediate regime between the elastic and plastic depinning.

Finally, for the elastic regime the previous theoretical investigations followed essential two approaches: (i) the elastic theory with renormalization group techniques [101, 190] and (ii) the perturbation theory in $1/v$ [102, 194, 195]. The first one explains the flowing channel structures and their mutual interactions, while the second one elucidates the $v - f$ characteristics and the criticality in

the depinning. Despite the number of experimental and numerical data a detailed theoretical understanding of the plastic motion remains still a challenge [196].

6.6 CONCLUSIONS

We studied the ground state and the dynamical properties of a classical Q1D infinite system of particles interacting through a Yukawa-type potential and with a Lorentzian shaped constriction potential. The system is confined in one direction by a parabolic potential. By MC simulations we found that at $T = 0$ the particles arrange themselves in a chain-like system, where the number of chains are a function of the number of particles, i.e. the density. Depending on the height and on the interaction range of the constriction barrier, a density gradient in the chain configuration is present near the constriction.

We studied the response of the system when an external driving force is applied in the not confined direction. We performed Langevin molecular dynamics simulations with periodic boundary conditions in the not confined direction and open conditions in the confined direction for different values of the driving force and for different temperatures. We found that the constriction barrier and the friction pin the particles up to a critical value of the driving force. The pinned phase is a new static phase, with particles accumulating in the neighborhood of the constriction barrier and arranging themselves in such a way to balance the external drive. For values of the driving force which are higher than the critical threshold, the particles can overcome the potential barrier and the system depins. We analyzed in detail the depinning phenomenon and we found that the system can depin elastically or quasi-elastically depending on the strength of the constriction potential. The quasi-elastic flow is a new regime, where particles move together without keeping their neighbors.

In the case of elastic flow the chain-like structure, formed at $T = 0$ in the absence of external drive, is preserved, while in the case of quasi-elastic flow it is destroyed and a complex net of conducting channels is created. The elastic depinning is characterized by a critical exponent, which is on average $\beta \sim 0.66$ and does not depend on the number of chains. This is in excellent agreement with the theoretical and numerical findings on 2D systems exhibiting elastic depinning. The quasi-elastic depinning state has a critical exponent $\beta \sim 0.94$. We demonstrated that the values of the critical exponent are independent of the range (i.e. screening length) of the inter-particle interaction. But the crossover between elastic and quasi-elastic flow depends on the kind of inter-particle interaction.

Furthermore, we showed that the dc conductivity is zero in the pinned regime, it has non-Ohmic characteristics after the activation of the motion and then it is constant, in other words the system has a non linear response

to the applied drive. The linear regime is attained as the asymptotic behavior. The dependence of the conductivity with temperature and strength of the constriction was also investigated. We found that in the single chain configuration for low height of the constriction, the conductivity is an increasing function of temperature, while in the multi-chain configuration it is a decreasing function, as expected. For high constriction barrier height, the conductivity has no longer a monotonic behavior, although it has a decreasing trend. In these cases some structures are present in the conductivity vs temperature curve, signaling the circumstance that some channels collapse or some parts of the system have already undergone the transition from the solid to the liquid state. Finally, for large values of the external driving force even in the case of high constriction barrier, the particles can flow orderly in a well defined channel structure, because the drive tilts the constriction potential, thus reducing the pinning strength, that is the system exhibits the phenomenon of dynamical reordering.

Publications. The result presented in this chapter were published as:

- G. Piacente and F. M. Peeters, *Pinning and depinning of a quasi-one-dimensional electron gas in the presence of a constriction*, submitted to Phys. Rev. B (20 pages).
- G. Piacente and F. M. Peeters, *Driven quasi-one-dimensional classical electron gas in the presence of a constriction*, submitted to Physica E (4 pages).

γ

Summary

The aim of this thesis was to study in detail the static, dynamical and melting properties of a classical Q1D Wigner crystal. The possibility of realizing and investigating such a Q1D system is inextricably related to possibility of confining the system in one dimension, which is nowadays routinely achieved in experiments by different techniques for several different systems. We investigated in detail both infinite and finite systems. The influence of inter-particle interaction and confining potential, the effect of temperature and external driving forces, the presence of constrictions were critically examined and the results were compared with experimental findings.

In what follows we summarize the contents of this work in the order they are presented in the previous chapters.

In **Chapter 1**, a general overview of the present PhD thesis was given. The concept of Wigner crystallization was introduced and examples of systems realized in laboratory, which exhibit such an ordered phase under proper conditions, are given. We discussed the physics of electrons above liquid helium, complex plasmas and colloidal suspensions. Other related systems, i.e. charged density waves, vortices in type II superconductors and biological molecules, for which Wigner crystallization or ordering originate very intriguing features, are also introduced. Additionally, we presented the general features shown by these systems when they are driven by an external force.

A description of the model system and the classical limit is given in **Chapter 2**. Scaling transformations are introduced in order to render the model very general, i.e. no longer depending on particular features of the system, but only on the inter-particle interaction and the external confining potential. The numerical approaches to obtain the relevant properties of the system under investigation are, then, introduced. We presented optimization techniques, namely Monte Carlo simulations with the standard Metropolis algorithm and simulated annealing, which are used to study the ground state configurations and the melting properties. Furthermore, we discussed Molecular Dynamics simulations, focusing on the Langevin Molecular Dynamics approach, which is the numerical method used to investigate dynamical properties, namely the response to an external applied drive.

The competition between inter-particle interaction, in the form of electrostatic repulsion, and external confinement, which is assumed parabolic and acting in one direction, generates a chain-like system. The ground state configuration and the structural phase transitions for the chain-like system are examined in **Chapter 3**. Experimentally, using parabolically confined colloidal particles or dusty plasmas or electrons on the surface of liquid helium, Q1D systems have been realized. In the case of colloids and complex plasma the inter-particle interaction is described by a Yukawa potential, while in the case of electrons on liquid helium it is described by a Coulomb potential. We provided a model for these systems and studied the ground state configurations. For low densities the particles crystallize in a single chain; with increasing density a zig-zag (continuous) transition occurs and the single chain splits into two chains. Further increasing the density we found the remarkable behavior that the four-chain structure is stabilized before the three-chain structure. The $2 \rightarrow 4$ chain transition occurs through a zig-zag transition of each of the chains accompanied by a shift along the chain direction. This first 4 chain configuration has a relatively small stability range after which the system transits to a three chain configuration. For higher values of the density, the four chain configuration attains again the lowest energy. Then a further increase of density will lead to more chains, that is 5, 6 and so on. The structural transitions are all discontinuous (i.e. first order), except the $1 \rightarrow 2$ transition. The chain system is intrinsically anisotropic, because of the confinement acting only in one direction. This reflects into the fact that (i) inter-chain and intra-chain distances are different and (ii) the distances between two neighbor chains is not homogeneous along the y -direction in the multi-chain configurations ($n \geq 4$). When the number of chains is extremely large the structures are more isotropic. In the case of Coulomb interaction a more homogenous system of chains than in the case of Yukawa interaction was obtained. Evidence for the single and multi-chain formation and the zig-zag transition has been found in experiments.

Once the equilibrium configuration at zero temperature was known, we investigated the small oscillations of the particles around their equilibrium positions. The normal modes of a classical Q1D system of particles interacting

through a Yukawa-type potential are, therefore, studied in **Chapter 4**. Within the harmonic approximation and exploiting the translational invariance of the ordered system in the unconfined direction, we calculated analytically the dispersion curves for the normal modes. The normal modes consist of longitudinal (acoustical) modes and transversal (optical) modes. The number of acoustical branches is equal to the number of optical branches and is equal to number of chains in the system. The normal modes of a Q1D multi-chain system can be studied experimentally in a dusty plasma, where small charged particles are externally confined by electric fields in between two electrode. The normal modes of the system were calculated first neglecting dissipative effects (the gas drag in the case of a plasma crystal) and then considering explicitly the presence of friction, in order to make direct comparisons with the experimental findings. The effect of a constant magnetic field on the dispersion relations was investigated and we found that the acoustical and optical branches are significantly modified. We studied also the case of forced oscillations induced by an external driving force (laser beams in the experiment) and focused on the case of single chain structures made by a finite number of particles. Our theoretical results are compared with experimental data and a remarkably good agreement between theory and experiment is found.

In **Chapter 5** we discussed melting of the system, i.e. the transition from the solid to the liquid phase. We performed Monte Carlo simulation and used the modified Lindemann criterion to estimate the melting temperature. We found evidence that melting starts first in the unconfined direction and that in the case of multi-chain structures, for a large number of chains, the most external chains undergo the solid to liquid phase transition before the internal chains melt. Two different melting temperatures, one for the confined direction and the other one for the unconfined direction, are identified. The melting temperature in both directions shows a reentrant behavior as a function of the density of particles. A regime of frustration, where the system melts at a relatively low temperature, is identified around the structural transition points. In the case of the single chain structure, the melting presents different characteristics with respect to the multi-chain configurations. We paid particular attention to the single chain case and formulated a new melting criterion in order to take into account the correlations at different temperatures in this case.

Finally, in **Chapter 6**, we first examined the ground state and the dynamical properties of a classical Q1D infinite system in the presence of a local Lorentzian shaped constriction potential. By Monte Carlo simulations we found that at $T = 0$ the chain-like structures are slightly modified with respect to the cases discussed in the other chapters. Depending on the height and on the interaction range of the constriction barrier, a density gradient in the chain configuration is present near the constriction. Then we studied the response of the system when a constant external driving force is applied in the unconfined direction. We performed Langevin Molecular Dynamics simulations for different values of the driving force and for different temperatures in order to investigate the

transport properties of the system. We found that the constriction barrier and the friction pins the particles up to a critical value of the driving force. The pinned phase is a new static phase, with particles accumulating in the neighborhood of the constriction barrier and arranging themselves in such a way to balance the external drive. For values of the driving force which are higher than the critical threshold, the particles can overcome the potential barrier and the system depins. We analyzed in detail the depinning phenomenon and we found that the system can depin elastically or quasi-elastically depending on the strength of the constriction potential. The quasi-elastic flow is a new regime, where particles move together without keeping their neighbors, and is intimately related to the low dimensionality and to the specific features of the constriction. We found a crossover between elastic and quasi-elastic depinning with increasing constriction strength. In the case of elastic flow the chain-like structure, formed at $T = 0$ in the absence of external drive, is preserved, while in the case of quasi-elastic flow it is destroyed and a complex net of conducting channels is created. The elastic depinning is characterized by a critical exponent, which is on average $\beta \sim 0.66$ and does not depend on the number of chains. This is in excellent agreement with the theoretical and numerical findings on 2D systems exhibiting elastic depinning. The quasi-elastic depinning state has a critical exponent $\beta \sim 0.94$. We demonstrated that the values of the critical exponent are independent of the inter-particle interaction, ranging from Coulomb to Yukawa type, while the crossover between elastic and quasi-elastic flow depends on it. Furthermore, we showed that the system has a non linear response to the applied drive and that the linear regime is attained as the asymptotic behavior for large values of the driving force. The dependence of the dc conductivity with temperature and strength of the constriction was also investigated and it was found that there are significant differences between the single and multi-chain regimes. For large values of the external driving force even in the case of high constriction barrier, we showed that the system exhibits the phenomenon of dynamical reordering.

8

Samenvatting

Het doel van deze thesis was om in detail de statische, dynamische en smelteigenschappen van een klassiek quasi-eendimensionaal (Q1D) Wignerkristal te bestuderen. De mogelijkheid om een dergelijk Q1D systeem te realiseren en te onderzoeken is onlosmakelijk verbonden met de mogelijkheid om het systeem in één dimensie in te perken, wat tegenwoordig d.m.v. routine-experimenten bereikt kan worden door verschillende technieken voor verschillende systemen. Wij onderzochten in detail zowel oneindige als eindige systemen. De invloed van de interactiepotentiaal tussen de deeltjes, de beperkingspotentiaal, het effect van de temperatuur, externe drijfkrachten en de aanwezigheid van constricties werden kritisch onderzocht en de resultaten werden vergeleken met experimentele bevindingen.

In wat volgt vatten wij de inhoud van dit werk samen in de volgorde van behandeling in de voorbije hoofdstukken.

In **Hoofdstuk 1** werd een algemeen overzicht van de huidige doctoraats-thesis gegeven. Het concept van Wignerkristallisatie werd geïntroduceerd en voorbeelden van in het laboratorium gerealiseerde systemen die een dergelijke geordende fase in de juiste omstandigheden vertonen worden gegeven. Wij bespraken de fysica van elektronen boven vloeibaar helium, complexe plasma's en colloïdale suspensies. Andere gerelateerde systemen, d.w.z. geladen dichtheidsgolven, draaikolken in type-II supergeleiders en biologische moleculen, waarvoor de Wignerkristallisatie of ordening aanleiding geven tot zeer intrigerende

eigenschappen, worden ook geïntroduceerd. Bovendien stelden wij de algemene karakteristieken voor wanneer deze systemen door een externe kracht uit evenwicht worden gebracht.

Een beschrijving van het modelsysteem en de klassieke limiet wordt gegeven in **Hoofdstuk 2**. Schaaltransformaties worden geïntroduceerd om het model zeer algemeen weer te geven, d.w.z. niet meer afhankelijk van bijzondere eigenschappen van het systeem, maar slechts van de interactiepotentiaal tussen de deeltjes en de externe inperkingspotentiaal. Vervolgens worden de numerieke benaderingen om de relevante eigenschappen van het onderzochte systeem te verkrijgen geïntroduceerd. Wij stelden optimaliseringstechnieken voor, namelijk Monte Carlo-simulaties met het Metropolis-standaardalgoritme, en simuleerden afkoeling om de configuraties van de grondtoestand en de smelteigenschappen te bestuderen. Voorts bespraken wij Moleculaire Dynamica-simulaties, ons daarbij concentrerend op de Langevin-Moleculaire-Dynamica-benadering, de numerieke methode die wordt gebruikt om dynamische eigenschappen - de reactie op een externe aandrijving - te onderzoeken.

De competitie van verschillende interacties tussen de deeltjes onderling - interacties in de vorm van elektrostatische afstoting en een externe, parabolische opsluiting die in één richting aangelegd werd - veroorzaakt de vorming van een ketenachtige structuur. De configuratie van de grondtoestand en de structurele fase overgangen voor het ketenachtige systeem worden onderzocht in **Hoofdstuk 3**. Experimenteel werden Q1D systemen gerealiseerd gebruik makend van colloïdale deeltjes, 'dusty' plasma's of elektronen op het oppervlak van vloeibaar helium. In het geval van colloïdale deeltjes en complexe plasma's wordt de interactie tussen de deeltjes beschreven door een Yukawa potentiaal, terwijl in het geval van elektronen op vloeibaar helium de interactie door een Coulomb potentiaal wordt beschreven. Wij hebben een model voor deze systemen voorgesteld en bestudeerden de configuraties van de grondtoestand. Voor lage dichtheden kristalliseren de deeltjes tot één enkele keten; voor een toenemende dichtheid treedt er een zig-zag (continue) overgang op en de keten splitst zich op in twee ketens. Als de dichtheid verder verhoogd wordt, kwamen we tot de vaststelling van een opmerkelijk gedrag, nl. de structuur met vier ketens stabiliseert zich voordat de structuur met drie ketens stabiel wordt. De $2 \rightarrow 4$ overgang komt er door een zig-zag overgang van elk van de ketens en gaat gepaard met een verschuiving langs de richting van de keten. Deze configuratie van vier ketens is stabiel over slechts een klein dichtheidsinterval, nadien gaat het systeem over in een configuratie met drie ketens. Voor hogere dichtheden bereikt de configuratie met vier ketens opnieuw de laagste energie. Nadien zal een verdere verhoging van de dichtheid leiden tot meer ketens, nl. vijf, zes, enz. De structurele overgangen zijn allemaal discontinu (d.w.z. het zijn eerst orde overgangen), behalve de overgang $1 \rightarrow 2$. Het ketensysteem is intrinsiek anisotroop, aangezien de opsluiting slechts in één richting werd aangelegd. Dit vertaalt zich in het feit dat (i) inter-keten en intra-keten afstanden verschillend zijn en (ii) de afstanden tussen twee naburige ketens niet homogeen is langs de

y -richting in de multi-ketenconfiguraties ($n \geq 4$). Als het aantal ketens zeer groot is, zijn de structuren meer isotroop. In het geval van de Coulomb interactie werd een homogener systeem van ketens verkregen dan in het geval van de Yukawa interactie. Het bewijs voor de vorming van zowel enkelvoudige als meervoudige ketens en de zig-zag overgang werd waargenomen in experimenten.

Zodra de evenwichtsconfiguratie voor temperatuur nul gekend was, onderzochten wij de kleine schommelingen van de deeltjes rond hun evenwichtsposities. Deze normale trillingsmodes van een klassiek Q1D systeem van deeltjes interagerend via een Yukawa-type potentiaal werden bestudeerd in **Hoofdstuk 4**. Binnen de harmonische benadering en gebruikmakende van de translatie-invariantie van het systeem in de onbegrensde richting, berekenden wij analytisch de dispersierelaties voor de normale trillingsmodes. De normale trillingmodes bestaan uit longitudinale (akoestische) en transversale (optische) modes. Het aantal akoestische takken is gelijk aan het aantal optische takken en is gelijk aan het aantal ketens in het systeem. De normale trillingmodes van zo een Q1D multi-ketensysteem kunnen experimenteel worden bestudeerd in een 'dusty' plasma, waarin kleine geladen deeltjes uiterlijk door elektrische velden tussen twee elektroden worden opgesloten. De normale trillingmodes van het systeem werden eerst berekend zonder rekening te houden met dissipatieve effecten (de wrijving met deeltjes in het gas in het geval van een plasmakristal) en daarna in de aanwezigheid van wrijving om zo een directe vergelijking met de experimentele resultaten te maken. Het effect van een constant magneetveld op de dispersierelaties werd onderzocht en wij vonden dat de akoestische en optische takken beduidend worden gewijzigd. Wij bestudeerden ook het geval van gedwongen schommelingen die door een extern opgelegde kracht (laserstralen in het experiment) worden veroorzaakt en concentreerden ons hierbij op structuren met slechts één ketting bestaande uit een eindig aantal deeltjes. Onze theoretische resultaten werden vergeleken met experimentele gegevens en een opmerkelijk goede overeenkomst tussen theorie en het experiment werd gevonden.

In **Hoofdstuk 5** bespraken wij de overgang van het systeem van de gecondenseerde naar de vloeibare fase. Wij voerden enkele Monte Carlo-simulaties uit en door het gebruik van het gewijzigde Lindemann-criterium konden wij de smelttemperaturen schatten. Onze simulaties toonden aan dat het smelten eerst in de onbegrensde richting plaats grijpt. In het geval van multi-ketenstructuren smelten de buitenste ketens eerder dan de interne ketens. Twee verschillende smelttemperaturen, een in de ingeperkte richting en een andere in de onbegrensde richting, werden geïdentificeerd. De smelttemperatuur in beide richtingen toont een inspringend gedrag als functie van de dichtheid van de deeltjes. Een regime van frustratie, waarbij het systeem bij een vrij lage temperatuur smelt, wordt geïdentificeerd rond de structurele overgangspunten. In het geval van één enkel ketensstructuur, toont het smeltproces een verschillend gedrag aan in vergelijking met de multi-ketensconfiguraties. Wij besteedden bijzondere

aandacht het enkele keten geval en formuleerden een nieuw smeltcriterium dat correlaties bij verschillende temperaturen in rekening brengt.

Tot slot, in **Hoofdstuk 6**, onderzochten wij eerst de grondtoestand en de dynamische eigenschappen van een klassieke Q1D oneindig systeem in de aanwezigheid van een lokaal Lorentziaan constrictepotentiaal. Door Monte Carlo-simulaties vonden wij dat bij $T=0$ de keten-achtige structuren lichtjes gewijzigd zijn ten opzichte van diegene besproken in de andere hoofdstukken. Afhankelijk van de hoogte en op de interactielengte van de constrictiebarrière, is er een dichtheidsgradiënt in de ketenconfiguratie aanwezig dichtbij de constrictie. Vervolgens bestudeerden wij de reactie van het systeem bij een constante externe drijfkracht in de onbegrensde richting. Wij voerden de Langevin-Moleculaire-Dynamica-simulaties uit voor verschillende waarden van de drijvende kracht en voor verschillende temperaturen om de transporteigenschappen van het systeem te onderzoeken. Wij vonden dat de constrictiebarrière en de wrijving, de deeltjes vastpint tot een kritische waarde van de stuwende kracht bereikt wordt. De vastgepinde fase is een nieuwe statische fase met deeltjes die in de buurt van de constrictiebarrière accumuleren en zich schikken op een dergelijke manier om de externe aandrijving in evenwicht te brengen. Voor waarden van de stuwende kracht die groter zijn dan de kritieke drempel, kunnen de deeltjes loskomen van de potentiaalbarrière. Wij analyseerden gedetailleerd het ontpin fenomeen en vonden dat het systeem elastisch of quasi-elastisch ontpint afhankelijk van de sterkte van de constrictiepotentiaal. De quasi-elastische stroom is een nieuw regime waar de deeltjes samen bewegen zonder hun burens te houden, en is intiem verwant met de lage dimensionaliteit en met de specifieke eigenschappen van de constrictie. Wij vonden een overgang tussen het elastische en quasi-elastische ontpinnen met benemende constrictiesterkte. In het geval van elastische stroom wordt de keten-achtige structuur, gevormd bij $T=0$ en bij afwezigheid van een externe aandrijving, bewaard, terwijl in het geval van quasi-elastische stroom het vernietigd wordt en een complex net van geleidende kanalen wordt gecreëerd. Het elastische ontpinnen wordt gekenmerkt door een kritieke exponent β , die gelijk is aan dat gemiddelde en niet afhangt van het aantal ketens. Dit is in uitstekende overeenkomst met de theoretische en numerieke bevindingen over 2D-systemen die het elastisch ontpinnen aantonen. De quasi-elastische ontpinde toestand geeft een kritieke exponent met $\beta \sim 0.94$. Wij toonden aan dat de waarden van de kritieke exponent onafhankelijk is van de interactie tussen de deeltjes, gaande van Coulombtot Yukawa-type, terwijl de overgang van elastische en quasi-elastische stroom hiervan afhankelijk is. Voorts toonden we dat het systeem een niet lineaire response heeft op de toegepaste aandrijving en dat het lineaire regime asymptotisch bereikt wordt, voor grote waarden van de stuwende kracht. De afhankelijkheid van het gelijkstroom geleidingsvermogen van temperatuur en sterkte van de constrictie werd ook onderzocht en we vonden significante verschillen tussen de enkel en multi-ketenregimes. Voor grote waarden van de externe drijfkracht, zelfs in

het geval van hoge constrictiebarrière, toonden wij aan dat het systeem het fenomeen van dynamische herordening vertoont.

Appendix A

Chapter 3

A.1 ENERGY PER PARTICLE IN MULTI-CHAIN CONFIGURATIONS

The expressions for the energy in the configurations beyond the two-chain structure are presented below. All the distances are in units of the inter-chain distance a between adjacent particles.

For the three-chain structure:

$$E_3 = \frac{\tilde{n}_e}{3} \sum_{m=1}^{\infty} \frac{\exp(-3m\kappa/\tilde{n}_e)}{m} + \frac{4\tilde{n}_e}{9} \sum_{m=1}^{\infty} \frac{\exp(-3\kappa\sqrt{(m-1/2)^2 + c_3^2}/\tilde{n}_e)}{\sqrt{(m-1/2)^2 + c_3^2}} + \frac{2\tilde{n}_e}{9} \sum_{m=1}^{\infty} \frac{\exp(-3\kappa\sqrt{m^2 + 4c_3^2}/\tilde{n}_e)}{\sqrt{m^2 + 4c_3^2}} + 6\frac{c_3^2}{\tilde{n}_e^2} + \frac{\tilde{n}_e \exp(-6c_3\kappa/\tilde{n}_e)}{18c_3},$$

where the intra-chain distance c_3 is a variational parameter.

For the four-chain structure:

$$\begin{aligned}
E_4 = & \frac{\tilde{n}_e}{4} \sum_{m=1}^{\infty} \frac{\exp(-4\kappa\sqrt{(m-1/2)^2 + (c_4 - f_4)^2}/\tilde{n}_e)}{\sqrt{(m-1/2)^2 + (c_4 - f_4)^2}} + \\
& \frac{\tilde{n}_e}{4} \sum_{m=1}^l \frac{\exp(-4\kappa m/\tilde{n}_e)}{m} + \frac{\tilde{n}_e}{4} \sum_{m=1}^{\infty} \frac{\exp(-4\kappa\sqrt{(m^2 + (c_4 + f_4)^2}/\tilde{n}_e)}{\sqrt{m^2 + (c_4 + f_4)^2}} + \\
& \frac{\tilde{n}_e}{8} \sum_{m=1}^{\infty} \frac{\exp(-4\kappa\sqrt{(m-1/2)^2 + 4f_4^2}/\tilde{n}_e)}{\sqrt{(m-1/2)^2 + 4f_4^2}} + \\
& \frac{\tilde{n}_e}{8} \sum_{m=1}^{\infty} \frac{\exp(-4\kappa\sqrt{(m-1/2)^2 + 4c_4^2}/\tilde{n}_e)}{\sqrt{(m-1/2)^2 + 4c_4^2}} + \\
& \frac{\tilde{n}_e}{8} \frac{\exp[-4(c_4 + f_4)\kappa/\tilde{n}_e]}{c_4 + f_4} + \frac{8c_4^2}{\tilde{n}_e^2} + \frac{8f_4^2}{\tilde{n}_e^2},
\end{aligned}$$

where c_4 is the distance of an inner chain and f_4 is the distance of an outer chain from the middle of the structure. These distances are two variational parameters which have to be optimized numerically.

For the five-chain structure:

$$\begin{aligned}
E_5 = & \frac{4\tilde{n}_e}{25} \sum_{m=1}^{\infty} \frac{\exp(-5\kappa\sqrt{(m-1/2)^2 + (c_5 - f_5)^2}/\tilde{n}_e)}{\sqrt{(m-1/2)^2 + (c_5 - f_5)^2}} + \\
& \frac{\tilde{n}_e}{5} \sum_{m=1}^{\infty} \frac{\exp(-5\kappa m/\tilde{n}_e)}{m} + \frac{4\tilde{n}_e}{25} \sum_{m=1}^{\infty} \frac{\exp(-5\kappa\sqrt{m^2 + c_5^2}/\tilde{n}_e)}{\sqrt{m^2 + c_5^2}} + \\
& \frac{4\tilde{n}_e}{25} \sum_{m=1}^{\infty} \frac{\exp(-5\kappa\sqrt{(m-1/2)^2 + (c_5 + f_5)^2}/\tilde{n}_e)}{\sqrt{(m-1/2)^2 + (c_5 + f_5)^2}} + \\
& \frac{\tilde{n}_e}{50} \frac{\exp(-10c_5\kappa/\tilde{n}_e)}{c_5} + \frac{2\tilde{n}_e}{25} \sum_{m=1}^{\infty} \frac{\exp(-5\kappa\sqrt{m^2 + 4c_5^2}/\tilde{n}_e)}{\sqrt{m^2 + 4c_5^2}} + \\
& \frac{4\tilde{n}_e}{25} \sum_{m=1}^{\infty} \frac{\exp(-5\kappa\sqrt{(m-1/2)^2 + f_5^2}/\tilde{n}_e)}{\sqrt{(m-1/2)^2 + f_5^2}} + \\
& \frac{2\tilde{n}_e}{25} \sum_{m=1}^{\infty} \frac{\exp(-5\kappa\sqrt{(m^2 + 4f_5^2)}/\tilde{n}_e)}{\sqrt{m^2 + 4f_5^2}} + \frac{\tilde{n}_e \exp(-10f_5\kappa/\tilde{n}_e)}{50f_5} + \\
& \frac{2\tilde{n}_e}{25} \frac{\exp(-5c_5\kappa/\tilde{n}_e)}{c_5} + \frac{10c_5^2}{\tilde{n}_e^2} + \frac{10f_5^2}{\tilde{n}_e^2},
\end{aligned}$$

with the variational parameters c_5 and f_5 , which are the distance of an inner chain and outer chain respectively from the middle of the structure.

For the six-chain structure:

$$\begin{aligned}
E_6 = & \frac{\tilde{n}_e}{6} \sum_{m=1}^{\infty} \frac{\exp(-6\kappa m/\tilde{n}_e)}{m} + \frac{\tilde{n}_e}{18} \sum_{m=1}^{\infty} \frac{\exp(-6\kappa\sqrt{(m-1/2)^2 + 4h_6^2}/\tilde{n}_e)}{\sqrt{(m-1/2)^2 + 4h_6^2}} + \\
& \frac{\tilde{n}_e}{18} \sum_{m=1}^{\infty} \frac{\exp(-6\kappa\sqrt{(m-1/2)^2 + 4f_6^2}/\tilde{n}_e)}{\sqrt{(m-1/2)^2 + 4h_6^2}} + \frac{\tilde{n}_e}{18} \frac{\exp[-6(h_6 + g_6)\kappa/\tilde{n}_e]}{(h_6 + g_6)} + \\
& \frac{\tilde{n}_e}{18} \sum_{m=1}^{\infty} \frac{\exp(-6\kappa\sqrt{(m-1/2)^2 + 4g_6^2}/\tilde{n}_e)}{\sqrt{(m-1/2)^2 + 4g_6^2}} + \frac{\tilde{n}_e}{18} \frac{\exp(-6|h_6 - f_6|\kappa/\tilde{n}_e)}{|h_6 - f_6|} + \\
& \frac{\tilde{n}_e}{9} \sum_{m=1}^{\infty} \frac{\exp(-6\kappa\sqrt{(m-1/2)^2 + (h_6 - g_6)^2}/\tilde{n}_e)}{\sqrt{(m-1/2)^2 + (h_6 - g_6)^2}} + \frac{12f_6^2}{\tilde{n}_e^2} + \\
& \frac{\tilde{n}_e}{9} \sum_{m=1}^{\infty} \frac{\exp(-6\kappa\sqrt{(m-1/2)^2 + (h_6 + f_6)^2}/\tilde{n}_e)}{\sqrt{(m-1/2)^2 + (h_6 + f_6)^2}} + \frac{12g_6^2}{\tilde{n}_e^2} + \\
& \frac{\tilde{n}_e}{9} \sum_{m=1}^{\infty} \frac{\exp(-6\kappa\sqrt{(m-1/2)^2 + (g_6 - f_6)^2}/\tilde{n}_e)}{\sqrt{(m-1/2)^2 + (g_6 - f_6)^2}} + \frac{12h_6^2}{\tilde{n}_e^2} + \\
& \frac{\tilde{n}_e}{9} \sum_{m=1}^{\infty} \frac{\exp(-6\kappa\sqrt{m^2 + (h_6 - f_6)^2}/\tilde{n}_e)}{\sqrt{m^2 + (h_6 - f_6)^2}} + \frac{\tilde{n}_e}{18} \frac{\exp[-6(g_6 + f_6)\kappa/\tilde{n}_e]}{(g_6 + f_6)} + \\
& \frac{\tilde{n}_e}{9} \sum_{m=1}^{\infty} \frac{\exp(-6\kappa\sqrt{m^2 + (g_6 + f_6)^2}/\tilde{n}_e)}{\sqrt{m^2 + (g_6 + f_6)^2}} + \\
& \frac{\tilde{n}_e}{9} \sum_{m=1}^{\infty} \frac{\exp(-6\kappa\sqrt{m^2 + (h_6 + g_6)^2}/\tilde{n}_e)}{\sqrt{m^2 + (h_6 + g_6)^2}},
\end{aligned}$$

with f_6 , g_6 and h_6 the three chain distances from the middle of the crystal, starting from the inner one which are the variational parameters.

Appendix B

Chapter 4

B.1 EQUATIONS OF MOTION IN THE HARMONIC APPROXIMATION

The equations of motion for particles in the three-chain configuration in the presence of friction are in matrix form:

$$\begin{pmatrix} \ddot{x}'_n{}^{(1)} \\ \ddot{y}'_n{}^{(1)} \\ \ddot{x}'_n{}^{(2)} \\ \ddot{y}'_n{}^{(2)} \\ \ddot{x}'_n{}^{(3)} \\ \ddot{y}'_n{}^{(3)} \end{pmatrix} = \gamma \begin{pmatrix} \dot{x}'_n{}^{(1)} \\ \dot{y}'_n{}^{(1)} \\ \dot{x}'_n{}^{(2)} \\ \dot{y}'_n{}^{(2)} \\ \dot{x}'_n{}^{(3)} \\ \dot{y}'_n{}^{(3)} \end{pmatrix} + \begin{pmatrix} -B_1 & 0 & -B_3 & 0 & -B_5 & 0 \\ 0 & -B_2 & 0 & -B_4 & 0 & -B_6 \\ -B_3 & 0 & -B_1 & 0 & -B_3 & 0 \\ 0 & -B_4 & 0 & -B_2 & 0 & -B_4 \\ -B_5 & 0 & -B_3 & 0 & -B_1 & 0 \\ 0 & -B_6 & 0 & -B_4 & 0 & -B_2 \end{pmatrix} \begin{pmatrix} x'_j{}^{(1)} \\ y'_j{}^{(1)} \\ x'_j{}^{(2)} \\ y'_j{}^{(2)} \\ x'_j{}^{(3)} \\ y'_j{}^{(3)} \end{pmatrix}$$

where the superscript labels the row which the particle is sitting in. The coefficients are:

$$\begin{aligned}
B_1 &= \frac{\tilde{n}_e^3}{54} \sum_j \frac{e^{-3j\kappa/\tilde{n}_e}}{j^3} \left[2 + 6\frac{j\kappa}{\tilde{n}_e} + 9\frac{j^2\kappa^2}{\tilde{n}_e^2} \right], \\
B_2 &= -\frac{\tilde{n}_e^3}{54} \sum_j \frac{e^{-3j\kappa/\tilde{n}_e}}{j^3} \left(1 + 3\frac{j\kappa}{\tilde{n}_e} \right), \\
B_3 &= \frac{\tilde{n}_e^3}{54} \sum_j \frac{e^{-3\kappa r_{12}/\tilde{n}_e}}{r_{12}^5} \left[\left(j + \frac{1}{2} \right)^2 \left(\frac{9\kappa r_{12}}{\tilde{n}_e} + \frac{9\kappa^2 r_{12}^2}{\tilde{n}_e^2} + 3 \right) - r_{12}^2 \left(1 + \frac{3\kappa r_{12}}{\tilde{n}_e} \right) \right], \\
B_4 &= \frac{\tilde{n}_e^3}{54} \sum_j \frac{e^{-3\kappa r_{12}/\tilde{n}_e}}{r_{12}^5} \left[c_3^2 \left(\frac{9\kappa r_{12}}{\tilde{n}_e} + \frac{9\kappa^2 r_{12}^2}{\tilde{n}_e^2} + 3 \right) - r_{12}^2 \left(1 + \frac{3\kappa r_{12}}{\tilde{n}_e} \right) \right], \\
B_5 &= \frac{\tilde{n}_e^3}{54} \sum_j \frac{e^{-3\kappa r_{13}/\tilde{n}_e}}{r_{13}^3} \left(\frac{9\kappa r_{13}}{\tilde{n}_e} + \frac{9\kappa^2 r_{13}^2}{\tilde{n}_e^2} + 3 \right), \\
B_6 &= \frac{\tilde{n}_e^3}{54} \sum_j \frac{e^{-3\kappa r_{13}/\tilde{n}_e}}{r_{13}^5} \left[4c_3^2 \left(\frac{9\kappa r_{13}}{\tilde{n}_e} + \frac{9\kappa^2 r_{13}^2}{\tilde{n}_e^2} + 3 \right) - r_{13}^2 \left(1 + \frac{3\kappa r_{13}}{\tilde{n}_e} \right) \right],
\end{aligned}$$

where $r_{12} = \sqrt{(j+1/2)^2 + c_3^2}$ and $r_{13} = \sqrt{j^2 + 4c_3^2}$ and c_3 is the distance of the external rows from the y axis.

The equations of motion for the 2 chain structure can be obtained by the 4×4 sub-matrices which are included in the top left part of the matrix of the coefficients: the coefficients involved in this case are B_1 , B_2 , B_3 and B_4 , with the substitution $\tilde{n}_e/3 \rightarrow \tilde{n}_e/2$ and $c_3 \rightarrow c_2/2$.

The equations of motion for the single chain structure can be obtained by the 2×2 sub-matrices which are included in the top left part of the matrix of the coefficients: the coefficients involved in this case are B_1 , B_2 with the substitution $\tilde{n}_e/3 \rightarrow \tilde{n}_e$ and $c_3 = 0$

In the presence of a constant magnetic field $\vec{B} = (0, 0, B)$ the equations of motions for the chain structures are easily obtained from the equations of motion with $B = 0$, adding the coupling terms $\dot{y}_n^{(i)} \omega_c$ and $-\dot{x}_n^{(i)} \omega_c$ to the equations for x and y motion respectively, for particles sitting in the i^{th} row, with ω_c the cyclotron frequency.

Obviously, the case without friction is immediately recovered by setting $\gamma = 0$.

B.2 EIGENFREQUENCIES IN MULTI-CHAIN CONFIGURATIONS

The dynamical matrix for the three-chain structure is:

$$D = \begin{pmatrix} B'_1 & 0 & B'_3 & 0 & B'_5 & 0 \\ 0 & \omega_0^2 + B'_2 & 0 & B'_4 & 0 & B'_6 \\ B'_3 & 0 & B'_1 & 0 & B'_3 & 0 \\ 0 & B'_4 & 0 & \omega_0^2 + B'_2 & 0 & B'_4 \\ B'_5 & 0 & B'_3 & 0 & B'_1 & 0 \\ 0 & B'_6 & 0 & B'_4 & 0 & \omega_0^2 + B'_2 \end{pmatrix}$$

where the parameters are

$$\begin{aligned}
B'_1 &= \tilde{n}_e^3 \sum_{j=1}^{\infty} \frac{\exp(-3j\kappa/\tilde{n}_e)}{27j^3} [2 + 6j\kappa/\tilde{n}_e + 9j^2\kappa^2/\tilde{n}_e^2][1 - \cos(kaj)], \\
B'_2 &= -\tilde{n}_e^3 \sum_{j=1}^{\infty} \frac{\exp(-3j\kappa/\tilde{n}_e)}{27j^3} (2 + 3j\kappa/\tilde{n}_e)[1 - \cos(kaj)], \\
B'_3 &= \tilde{n}_e^3 \sum_{j=1}^{\infty} \frac{\exp(-3\kappa\sqrt{(j+1/2)^2+c^2}/\tilde{n}_e)}{27\sqrt{(j+1/2)^2+c^2}} \times \\
&\quad [\cos(ka(j+1/2)) - 1](j+1/2)^2 \left[\frac{9\kappa\sqrt{(j+1/2)^2+c_3^2}}{\tilde{n}_e} + \right. \\
&\quad \left. \frac{9\kappa^2[(j+1/2)^2+c_3^2]}{\tilde{n}_e^2} + 3 \right] - \left(1 + \frac{3\kappa\sqrt{(j+1/2)^2+c^2}}{\tilde{n}_e} \right) \times \\
&\quad [(j+1/2)^2+c_3^2], \\
B'_4 &= \tilde{n}_e^3 \sum_{j=1}^{\infty} \frac{\exp(-3\kappa\sqrt{(j+1/2)^2+c_3^2}/\tilde{n}_e)}{27\sqrt{(j+1/2)^2+c_3^2}} \times \\
&\quad [\cos(ka(j+1/2)) - 1]c_3^2 \left[\frac{9\kappa\sqrt{(j+1/2)^2+c_3^2}}{\tilde{n}_e} + \right. \\
&\quad \left. \frac{9\kappa^2[(j+1/2)^2+c_3^2]}{\tilde{n}_e^2} + 3 \right] - \left[1 + \frac{3\kappa\sqrt{(j+1/2)^2+c_3^2}}{\tilde{n}_e} \right] \times \\
&\quad [(j+1/2)^2+c_3^2], \\
B'_5 &= \tilde{n}_e^3 \sum_{j=1}^{\infty} \frac{\exp(-3\kappa\sqrt{j^2+4c_3^2}/\tilde{n}_e)}{27(j^2+4c_3^2)\sqrt{j^2+4c_3^2}} [\cos(kaj) - 1] \times \\
&\quad \left[\frac{9\kappa\sqrt{j^2+4c_3^2}}{\tilde{n}_e} + \frac{9\kappa^2(j^2+4c_3^2)}{\tilde{n}_e^2} + 3 \right], \\
B'_6 &= \tilde{n}_e^3 \sum_{j=1}^{\infty} \frac{\exp(-3\kappa\sqrt{j^2+4c_3^2}/\tilde{n}_e)}{27\sqrt{j^2+4c_3^2}} [\cos(kaj) - 1] \times \\
&\quad \left[\left(\frac{9\kappa\sqrt{j^2+4c_3^2}}{\tilde{n}_e} + \frac{9\kappa^2(j^2+4c_3^2)}{\tilde{n}_e^2} + 3 \right) 4c_3^2 - \left(1 + \frac{3\kappa\sqrt{j^2+4c_3^2}}{\tilde{n}_e} \right) \times \right. \\
&\quad \left. (j^2+4c_3^2) \right],
\end{aligned}$$

The eigenfrequencies and the eigenmodes are respectively the eigenvalues and the eigenvectors of the dynamical matrix.

The modes for the single-chain can be obtained by the top left part of the matrix D which forms a 2×2 sub-matrix and involves the elements B'_1 and B'_2 with the same substitutions indicated in the previous section.

Similarly, the modes for the two-chain structure can be obtained by the 4×4 sub-matrix which is included in the top left part of matrix D and involves the elements B'_1, B'_2, B'_3 and B'_3 with the same substitutions indicated in the previous section.

Explicitly, the eigenfrequencies are:
for the single chain configuration:

$$\begin{aligned}\omega_{ac}^{(1)} &= \sqrt{B'_1 - \gamma^2/4 - i\gamma/2}, \\ \omega_{opt}^{(2)} &= \sqrt{1 + B'_2 - \gamma^2/4 - i\gamma/2},\end{aligned}$$

for the 2 chain configuration:

$$\begin{aligned}\omega_{ac}^{(1)} &= \sqrt{B'_1 + B'_3 - \gamma^2/4 - i\gamma/2}, \\ \omega_{opt}^{(1)} &= \sqrt{B'_2 + B'_4 - \gamma^2/4 - i\gamma/2}, \\ \omega_{ac}^{(2)} &= \sqrt{1 + B'_1 - B'_3 - \gamma^2/4 - i\gamma/2}, \\ \omega_{opt}^{(2)} &= \sqrt{1 + B'_2 - B'_4 - \gamma^2/4 - i\gamma/2},\end{aligned}$$

and, finally, for the 3 chain configuration:

$$\begin{aligned}\omega_{ac}^{(1)} &= \sqrt{B'_1 - B'_5 - \gamma^2/4 - i\gamma/2}, \\ \omega_{opt}^{(1)} &= \sqrt{1 + B'_2 - B'_6 - \gamma^2/4 - i\gamma/2}, \\ \omega_{ac}^{(2)} &= \sqrt{B'_1 + B'_5/2 + \sqrt{B'^2_5 + 8B'^2_3/2} - \gamma^2/4 - i\gamma/2}, \\ \omega_{opt}^{(2)} &= \sqrt{1 + B'_2 + B'_6/2 + \sqrt{B'^2_6 + 8B'^2_4/2} - \gamma^2/4 - i\gamma/2}, \\ \omega_{ac}^{(3)} &= \sqrt{B'_1 + B'_5/2 - \sqrt{B'^2_5 + 8B'^2_3/2} - \gamma^2/4 - i\gamma/2}, \\ \omega_{opt}^{(3)} &= \sqrt{1 + B'_2 + B'_6/2 - \sqrt{B'^2_6 + 8B'^2_4/2} - \gamma^2/4 - i\gamma/2}.\end{aligned}$$

Obviously, the case without friction is immediately recovered by setting $\gamma = 0$.

B.3 AMPLITUDE OF DISPLACEMENTS

We present the analytical expressions for the displacements $A_i^{x,y}$ calculated from the Kramer's rule in the case of a system of $N = 29$ particles. The central

particle at which the driving force is acting is labeled with $N = 0$. For reasons of symmetry $A_{-l}^{x,y} = A_l^{x,y}$.

$$\begin{aligned}
A_0^{x,y} &= (a^2 - b^2)(-b^2 - ba + a^2)(-b^2 + ba + a^2) \times \\
&\quad (b^4 + 4b^3a - 4b^2a^2 - ba^3 + a^4)(b^4 - 4b^3a - 4b^2a^2 + ba^3 + a^4)C/D; \\
A_1^{x,y} &= -ab(-b^3 - 2b^2a + ba^2 + a^3)(b^3 - 2b^2a - ba^2 + a^3) \times \\
&\quad (-7b^6 + 14b^4a^2 - 7b^2a^4 + a^6)C/D; \\
A_2^{x,y} &= ab^2(-a^6 + a^5b + 5a^4b^2 - 4a^3b^3 - 6a^2b^4 + 3ab^5 + b^6) \times \\
&\quad (-a^6 - a^5b + 5a^4b^2 + 4a^3b^3 - 6a^2b^4 - 3ab^5 + b^6)C/D; \\
A_3^{x,y} &= -ab^3(-3b^2 + a^2)(a^2 - b^2)(-2b^2 + a^2)(b^4 - 4b^2a^2 + a^4)C/D; \\
A_4^{x,y} &= -b^4(-a^5 + a^4b + 4a^3b^2 - 3a^2b^3 - 3ab^4 + b^5) \times \\
&\quad (a^5 + a^4b - 4a^3b^2 - 3a^2b^3 + 3ab^4 + b^5)C/D; \\
A_5^{x,y} &= -ab^5(-a^2 - ba + b^2)(-a^2 + ba + b^2)(a^4 - 5a^2b^2 + 5b^4)C/D; \\
A_6^{x,y} &= b^6(a^2 - b^2)(-b^3 - 3b^2a + a^3)(b^3 - 3b^2a + a^3)C/D; \\
A_7^{x,y} &= -ab^7(-2b^2 + a^2)(2b^4 - 4b^2a^2 + a^4)C/D; \\
A_8^{x,y} &= b^8(b^3 - 2b^2a - ba^2 + a^3)(-b^3 - 2b^2a + ba^2 + a^3)C/D; \\
A_9^{x,y} &= -ab^9(-3b^2 + a^2)(a^2 - b^2)C/D; \\
A_{10}^{x,y} &= b^{10}(-b^2 + ab + a^2)(-b^2 - ab + a^2)C/D; \\
A_{11}^{x,y} &= ab^{11}(2b^2 - a^2)C/D; \\
A_{12}^{x,y} &= b^{12}(a^2 - b^2)C/D; \\
A_{13}^{x,y} &= -ab^{13}C/D; \\
A_{14}^{x,y} &= -b^{14}/D,
\end{aligned}$$

where $D = a(-3b^2 + a^2)(5b^4 - 5b^2a^2 + a^4)(b^8 - 8b^6a^2 + 14b^4a^4 - 7b^2a^6 + a^8)$. In the case of displacements along the x -direction: $a = \omega'^2 + i\gamma'\omega' - 2b$, $b = (\tilde{n}_e^3/2) \exp(-\kappa/n)(2 + 2\kappa/\tilde{n}_e + \kappa^2/\tilde{n}_e^2)$ and $C = F_0^x$, while in the case of displacements along the y -direction: $a = \omega'^2 - 1 + i\gamma'\omega' - 2b$, $b = -(\tilde{n}_e^3/2) \exp(-\kappa/\tilde{n}_e)(1 + \kappa/\tilde{n}_e)$ and $C = F_0^y$.

References

1. E. Wigner, Phys. Rev. **46**, 1002 (1934).
2. N. Metropolis, A.W. Rosenbluth, M.N. Rosenbluth, A.M. Teller and E. Teller, J. Chem. Phys. **21**, 1087 (1953).
3. R.C. Gann, S. Chakravarty and G.V. Chester, Phys. Rev. B **20**, 326 (1979).
4. R.H. Morf, Phys. Rev. Lett. **43**, 931 (1979).
5. J. Wineland and W. M. Itano, Phys. Today **40** (6), 34 (1987); C. N. Cohen Tannoudji and W. D. Phillips, ibid. **43** (10), 33 (1990).
6. B. Tanatar and D. M. Ceperley, Phys. Rev. B **39**, 5005 (1989).
7. J. Yoon, C. C. Li, D. Shahar, D. C. Tsui, and M. Shayegan, Phys. Rev. Lett. **82**, 1744 (1999).
8. R. S. Crandall and R. Williams, Phys. Lett. A **34**, 404 (1971).
9. C. C. Grimes and G. Adams, Phys. Rev. Lett. **42**, 795 (1979).
10. R. C. Ashoori, Nature (London), **379**, 413 (1996).
11. J. H. Chu and L. I, Phys. Rev. Lett. **72**, 4009 (1994).
12. H. Thomas, G. E. Morfill, V. Demmel, J. Goree, B. Feuerbacher and D. Möhlmann, Phys. Rev. Lett. **73**, 652 (1994).

13. Y. Hayashi and K. Tachibana, Japan J. Appl. Phys. **33**, L804 (1994).
14. A. Melzer, T. Trottenberg, and A. Piel, Phys. Lett. A **191**, 301 (1994).
15. S. Nesper, C. Bechinger, P. Leiderer, and T. Palberg, Phys. Rev. Lett. **79**, 2348 (1997).
16. R. Bubeck, C. Bechinger, S. Nesper, and P. Leiderer, Phys. Rev. Lett. **82**, 3364 (1999).
17. B. G. Levi, Phys. Today **41** (9), 17 (1988).
18. F. Diedrich, E. Peik, J. M. Chen, W. Quint, and H. Walther, Phys. Rev. Lett. **59**, 2931 (1987).
19. A. Rahman and J. P. Schiffer, in: *Condensed Matter Theories*, Vol. **2**, eds. P. Vashishta *et al*, (Plenum Press, New York, 1987), p. 33.
20. J. Beebe-Wang, N. Elander, and R. Schuch, Phys. Scripta **46**, 506 (1992).
21. D. H. E. Dubin and T. M. O'Neil, Phys. Rev. Lett. **60**, 511 (1988).
22. Y. Kondo, J. S. Korhonen, M. Krusius, V. V. Dmitriev, E. V. Thuneberg, and G. E. Volovik, Phys. Rev. Lett. **68**, 3331 (1992).
23. E. J. Yarmachuk and R. E. Packard, J. Low Temp. Phys. **46**, 479 (1982).
24. W. I. Glaberson and K. W. Schwarz, Physics Today **40** (2), 54 (1987).
25. F. Chevy, K. W. Madison, and J. Dalibard, Phys. Rev. Lett. **85**, 2223 (2000).
26. A. A. Abrikosov, Zh. Eksp. Teor. Fiz. **32**, 1442 (1957).
27. D. Reefman and H. B. Brom, Physica C **183**, 212 (1991).
28. E. O. Budrene and C. B. Howard, Nature (London) **376**, 49 (1995).
29. L. Tsimring, H. Levine, I. Aranson, E. Ben-Jacob, I. Cohen, O. Shochet, and W. N. Reynolds, Phys. Rev. Lett. **75**, 1859 (1995).
30. M. Saint Jean, C. Even, and C. Guthmann, Europhys. Lett. **55**, 45 (2001).
31. P. Leiderer, W. Ebner, and V. B. Shikin, Surf. Sci. **113**, 405 (1987).
32. P. L. Elliott, S. S. Nazin, C. I. Pakes, L. Skrbek, W. F. Vinen, and G. F. Cox, Phys. Rev. B **56**, 3447 (1997).
33. P. Glasson, V. Dotsenko, P. Fozooni, M. J. Lea, W. Bailey, G. Papageorgiou, S. E. Andresen, and A. Kristensen, Phys. Rev. Lett. **87**, 176802 (2001).

34. P. M. Platzman and M. I. Dykman, *Science* **284**, 1967 (1999).
35. T. Graham, *Journal of the Chemical Society of London*, **17**, 318 (1864)
36. D. A. Weitz and W. B. Russel, *MRS Bulletin* **29**, 82 (2004).
37. I. Rouzina and V. A. Bloomfield, *J. Chem. Phys.* **100**, 9977 (1996).
38. A. Valkering, J. Klier, and P. Leiderer, *Physica B* **284**, 172 (2000).
39. J. Chakrabarti, H. R. Krishnamurthy, and A. K. Sood, *Phys. Rev. Lett.* **73**, 2923 (1994).
40. H. Löwen, *J. Phys.: Condens. Matt.* **13**, R415 (2001).
41. V. A. Frolov, C. N. Likos and H. Löwen, *J. Phys.: Condens. Matt.* **16**, S4103 (2004).
42. S. A. Tatarkova, A. E. Carruthers, and K. Dholakia, *Phys. Rev. Lett.* **89**, 283901 (2002).
43. J. Baumgartl, M. Brunner, and C. Bechinger, *Phys. Rev. Lett.* **93**, 168301 (2004).
44. L. Radzihovsky, E. Frey, and D. R. Nelson, *Phys. Rev. E* **63**, 031503 (2001); E. Frey, D. R. Nelson, and L. Radzihovsky, *Phys. Rev. Lett.* **83**, 2977 (1999).
45. R. Haghgoie and P. S. Doyle, *Phys. Rev. E* **70**, 061408 (2004)
46. R. A. Segalman, A. Hexemer, and E. J. Kramer, *Phys. Rev. Lett.* **91**, 196101 (2003).
47. G. S. Selwyn, J. S. McKillop, K. Haller, and J. Wu, *J. Vac. Sci. Technol. A* **8**, 1726 (1990).
48. P. Belenguer, J. P. Blondeau, L. Boufendi, M. Toogood, A. Plain, A. Bouchoule, C. Laure, and J. P. Boeuf, *Phys. Rev. A* **46**, 7923 (1992).
49. H. Ikezi, *Phys. Fluids* **29**, 1764 (1986).
50. S. Nunomura, D. Samsonov, and J. Goree, *Phys. Rev. Lett.* **84**, 5141 (2000).
51. B. Liu, K. Avinash, and J. Goree, *Phys. Rev. Lett.* **91**, 255003 (2003).
52. A. Melzer, V. Schweigert, I. Schweigert, A. Homann, S. Peters, and A. Piel, *Phys. Rev. E* **54**, R46 (1996).
53. M. Kong, B. Partoens, and F. M. Peeters, *New Journal of Physics* **5**, 23 (2003).

54. L. I, W. T. Juan, C. H. Chiang, and J. H. Chu, *Science* **272**, 1626 (1996).
55. C. H. Chiang and L. I, *Phys. Rev. Lett.* **77**, 647 (1996).
56. W. T. Juan and L. I, *Phys. Rev. Lett.* **80**, 3073 (1998).
57. U. Konopka, G. E. Morfill, and L. Ratke, *Phys. Rev. Lett.* **84**, 891 (2000).
58. A. Melzer, *Phys. Rev. E* **67**, 016411 (2003).
59. M. Kong, PhD thesis, Universiteit Antwerpen, 2004.
60. V. A. Schweigert and F. M. Peeters, *Phys. Rev. B* **51**, 7700 (1995).
61. T. Misawa, N. Ohno, K. Asano, M. Sawai, S. Takamura, and P. K. Kaw, *Phys. Rev. Lett.* **86**, 1219 (2001).
62. J. B. Pieper and J. Goree, *Phys. Rev. Lett.* **77**, 3137 (1996).
63. M. Kong, B. Partoens, and F. M. Peeters, *Phys. Rev. E* **67**, 021608 (2003).
64. M. Rosenberg and G. Kalman, *Phys. Rev. E* **56**, 7166 (1997).
65. B. Liu, J. Goree, V. Nosenko, and L. Boufendi, *Phys. Plasmas* **10**, 9 (2003).
66. A. Homann, A. Melzer, S. Peters, and A. Piel, *Phys. Rev. E* **56**, 7138 (1997).
67. B. Liu, K. Avinash, and J. Goree, *Phys. Rev. E* **69**, 036410 (2004).
68. B. Liu, J. Goree, *Phys. Rev. E* **71**, 046410 (2005).
69. S. Earnshaw, *Trans. Camb. Phil. Soc.* **7**, 97
70. H. C. Nägerl, W. Bechter, J. Eschner, F. Schmidt-Kaler, and R. Blatt, *Appl. Phys. B: Lasers Opt.* **B66**, 603 (1998).
71. D. J. Wineland, J. C. Bergquist, W. M. Itano, J. J. Bollinger, and C. H. Manney, *Phys. Rev. Lett.* **59**, 2935 (1987).
72. T. B. Mitchell, J. J. Bollinger, D. H. E. Dubin, X.-P. Huang, W. M. Itano and R. H. Baughman, *Science* **282**, 1290 (1998).
73. M. Drewsen, C. Brodersen, L. Hornekær, J. S. Hangst and J. P. Schiffer, *Phys. Rev. Lett.* **81**, 2878 (1998).
74. S. L. Gilbert, J. J. Bollinger, and D. J. Wineland, *Phys. Rev. Lett.* **60**, 2022 (1988).
75. J. N. Tan, J. J. Bollinger, B. Jelenkovic, and D. J. Wineland, *Phys. Rev. Lett.* **75**, 4198 (1995).

76. G. Birkel, S. Kassner, and H. Walther, *Nature* **357**, 310 (1992).
77. M. Block, A. Drakoudis, H. Leuthner, P. Seibert, and G. Werth, *J. Phys. B* **33**, L375 (2000).
78. J. D. Prestage, A. Williams, L. Maleki, M. J. Djomehri, and E. Harabetian, *Phys. Rev. Lett.* **66**, 2964 (1991).
79. S. Talapatra and A. D. Migone, *Phys. Rev. Lett.* **87**, 206106 (2001)
80. A. Siber, *Phys. Rev. B* **66**, 235414 (2002).
81. M. T. Cvitas and A. Siber, *Phys. Rev. B* **67**, 193401 (2003).
82. J. I. Cirac and P. Zoller, *Phys. Rev. Lett.* **74**, 4091 (1995).
83. R. E. Thorne, *Phys. Today* (**5**), 42 (1996).
84. G. Grüner, *Rev. Mod. Phys.* **60**, 1129 (1988).
85. B. Baelus, PhD thesis, Universiteit Antwerpen, 2003; M. Milosevic, PhD thesis, Universiteit Antwerpen, 2004.
86. H. F. Hess, R. B. Robinson, R. C. Dynes, J. M. Valles, Jr., and J. V. Waszczak, *Phys. Rev. Lett.* **62**, 214 (1989).
87. E. Sardella, M. M. Doria and P. R. S. Netto, *Phys. Rev. B* **60**, 13158 (1999).
88. G. Carneiro, *Phys. Rev. B* **57**, 6077 (1998).
89. C. C. de Souza Silva, L. R. E. Cabral, and J. Albino Aguiar, *Phys. Rev. B* **63**, 134256 (2001).
90. R. Besseling, P. H. Kes, T. Dröse, and V. M. Vinokur, *New J. Phys.* **7**, 71 (2005).
91. G. Blatter, M. V. Feigel'man, V. B. Geshkenbein, A. I. Larkin, and V. M. Vinokur, *Rev. Mod. Phys.* **66**, 1125 (1994).
92. Yu. E. Lozovik and E. A. Rakoch, *Phys. Rev. B* **57**, 1214 (1998).
93. V. A. Bloomfield, *Curr. Opin. Struct. Biol.* **6**, 334 (1996).
94. W. M. Gelbart, R. F. Bruinsma, P. A. Pincus, and V. A. Parsegian, *Phys. Today* **53** (9), 38 (2000).
95. B. I. Shklovskii, *Phys. Rev. Lett.* **82**, 3268 (1999).
96. F. Oosawa, *Biopolymers* **6**, 1633 (1968); G. S. Manning, *J. Chem. Phys.* **51**, 924 (1969).

97. N. Grønbech-Jensen, R. J. Mashl, R. F. Bruinsma, and W. M. Gelbart, *Phys. Rev. Lett.* **78**, 2477 (1997).
98. T. E. Angelini, H. Liang, W. Wriggers, and G. Wong, *PNAS* **100**, 8634 (2003).
99. C. Reichhardt and C. J. Olson, *Phys. Rev. Lett.* **89**, 078301 (2002).
100. P. Le Doussal and T. Giamarchi, *Phys. Rev. B* **52**, 1242 (1995)
101. P. Le Doussal and T. Giamarchi, *Phys. Rev. B* **57**, 11356 (1998).
102. A. I. Larkin and Y. N. Ovchinnikov, *Sov. Phys. JETP* **38**, 854 (1974).
103. D. S. Fisher, *Phys. Rev. B* **31**, 1396 (1985).
104. P. B. Littlewood, in *Charge Density Waves in Solids: Proceedings, Budapest, 1984*, edited by G. Hutiray and J. Slyom (Springer-Verlag, Berlin, 1985).
105. L. Sneddon, M. C. Cross, and D. S. Fisher, *Phys. Rev. Lett.* **49**, 292 (1982).
106. O. Narayan and D. S. Fisher, *Phys. Rev. B* **46**, 11520 (1992).
107. J. Chen, Y. Cao, and Z. Jiao, *Phys. Rev. E* **69**, 041403 (2004).
108. U. Yaron, P. L. Gammel, D. A. Huse, R. N. Kleiman, C. S. Oglesby, E. Bucher, B. Batlogg, D. J. Bishop, K. Mortensen, K. Clausen, C. A. Bolle, and F. DeLaCruz, *Phys. Rev. Lett.* **73**, 2748 (1994).
109. A. E. Koshelev and V. M. Vinokur, *Phys. Rev. Lett.* **73**, 3580 (1994).
110. K. Moon, R. T. Scalettar, and G. T. Zimnyi, *Phys. Rev. Lett.* **77**, 2778 (1996).
111. S. Ryu, M. HELLERQVIST, S. Doniach, A. Kapitulnik, and D. Stroud, *Phys. Rev. Lett.* **77**, 5114 (1996).
112. F. Pardo, F. De La Cruz, P. L. Gammel, C. S. Oglesby, E. Bucher, B. Batlogg, and D. J. Bishop, *Phys. Rev. Lett.* **78**, 46334636 (1997).
113. F. Perruchot, PhD thesis, Ecole Polytechnique, Paris, 1995.
114. M. Tinkham, *Introduction to Superconductivity* (McGraw-Hill, New York, 1975).
115. B. Partoens and P. S. Deo, *Phys. Rev. B* **69**, 245415 (2004).
116. W. K. Hastings, *Biometrika* **57**, 97 (1970).

117. D. M. Ceperley, *J. Stat. Phys.* **63**, 1237 (1991).
118. S. Geman and D. Geman, *IEEE Transactions on Pattern Analysis and Machine Intelligence* **6**, 721 (1984).
119. F. Ercolessi, *A Molecular Dynamic Primer*, SISSA, Trieste (1996).
120. S. Nose, *Prog. Theor. Phys. Supp.* **103**, 1 (1991).
121. L. Verlet, *Phys. Rev.* **159**, 98 (1967).
122. M. P. Allen and D. J. Tildesley, *Computer simulation of liquids*, Oxford, 1987.
123. H. J. C. Berendsen and W. F. van Gunsteren, in *Molecular dynamics simulation of statistical-mechanical systems*, Eds. G. Ciccotti and W. G. Hoover (North-Holland, Amsterdam, 1986).
124. M. Bixon and R. Zwanzig, *Phys. Rev.* **187**, 267 (1969).
125. H. Mori, *Prog. Theor. Phys.* **33**, 423 (1965).
126. J. L. Garca-Palacios and F. J. Lzaro, *Phys. Rev. B* **58**, 14937 (1998).
127. R. Mannella, *Phys. Rev. E* **69**, 041107 (2004).
128. L. Bonsall and A. A. Maradudin, *Phys. Rev. B* **15**, 1959 (1977).
129. D. Knuth, *The art of computer programming*(Addison-Wesley, Reading MA, 2nd edition, 1973).
130. M. P. Lilly, K. B. Cooper, J. P. Eisenstein, L. N. Pfeiffer, and K. W. West, *Phys. Rev. Lett.* **82**, 394 (1999).
131. E. Dagotto, T. Hotta, and A. Moreo, *Physics Reports*, **344**, 1 (2001).
132. Yu. Z. Kovdrya, *Low Temperature Physics* **29**, 77 (2003).
133. G. M. Whitesides and A. D. Stroock, *Phys. Today* **54** (6), 42 (2001).
134. K. Zahn, R. Lenke, and G. Maret, *Phys. Rev. Lett.* **82**, 2721 (1999).
135. N. D. Mermin, *Phys. Rev.* **171**, 272 (1968).
136. S. J. Chen and D. H. E. Dubin, *Phys. Rev. Lett.* **71**, 2721 (1993).
137. H. J. Schultz, *Phys. Rev. Lett.* **71**, 1864 (1993).
138. L. I. Glazman, I. M. Ruzin, and B. I. Shklovskii, *Phys. Rev. B* **45**, 8454 (1992).

139. D. Pines, *Elementary excitations in solids* (Addison-Weiley, N.Y., 1963), p. 13.
140. E. Y. Andrei, G. Deville, D. C. Glattli, F. I. B. Williams, E. Paris, and B. Etienne, *Phys. Rev. Lett.* **60**, 2765 (1988).
141. H. L. Stormer and R. L. Willett, *Phys. Rev. Lett.* **62**, 972 (1989).
142. J. M. Kosterlitz and D. J. Thouless, *J. Phys. C* **5**, L124 (1972); B. I. Halperin and D. R. Nelson, *Phys. Rev. Lett.* **41**, 121 (1978); A. P. Young, *Phys. Rev. B* **19**, 1855 (1979).
143. Q. H. Wei, C. Bechinger, D. Rudhardt, and P. Leiderer, *Phys. Rev. Lett.* **81**, 2606 (1998).
144. J. M. Ziman, *Principles of the Theory of Solids* (Cambridge University Press, Cambridge, 1972), p. 39-41.
145. D. S. Fisher, *Phys. Rev. B* **26**, 5009 (1982).
146. G. Goldoni and F. M. Peeters, *Phys. Rev. B* **53**, 4591 (1996).
147. L. Candido, J. P. Rino, N. Studart, and F. M. Peeters, *J. Phys.: Condens. Matter.* **10**, 11627 (1998).
148. A. A. Koulakov and B. I. Shklovskii, *Phys. Rev. B* **57**, 2352 (1998).
149. L. D. Landau and E. M. Lifshitz, *Elasticity Theory* (Reed Educational and Professional Publishing, Exeter, 1996), Sec. 24.
150. J. H. Van Leeuwen, *J. Physique* **6**, 361 (1921).
151. S. S. Sokolov and O. I. Kirichek, *Low Temp. Phys.* **20**, 599 (1994).
152. A. V. Chaplik, *Sov. Phys. - JETP* **35**, 395(1972).
153. F. Lindemann, *Z. Phys.* **11**, 609 (1910).
154. S. A. Cho, *J. Phys. F: Met. Phys.* **12**, 1069 (1982).
155. V. M. Bedanov and F. M. Peeters, *Phys. Rev. B* **49**, 2667 (1994).
156. V. M. Bedanov, G. V. Gadiyak, and Yu. E. Lozovik, *Phys. Lett. A* **109**, 289 (1985).
157. D. B. Chklovskii, B. I. Shklovskii, and L. I. Glazman, *Phys. Rev. B* **46**, 4026 (1992).
158. E. Y. Andrei, Ed., *Two dimensional Electron Systems on Helium and Other Cryogenic Substrates* (Academic Press, New York, 1991).

159. K. M. S. Bajaj and R. Mehrotra, *Physica B* **194-196**, 1235 (1994).
160. R. Côté and H. A. Fertig, *Phys. Rev. B* **48**, 10955 (1993).
161. I. V. Schweigert, V. A. Schweigert, and F. M. Peeters, *Phys. Rev. B* **60**, 14665 (1999); *Phys. Rev. Lett.* **82**, 5293 (1999).
162. Y. V. Nazarov, *Europhys. Lett.* **32**, 443 (1995).
163. A. Brown, *Can. J. Chem.* **52**, 791 (1974).
164. P. Segovia, D. Purdie, M. Hengsberger, and Y. Baer, *Nature (London)* **402**, 504 (1999).
165. N. W. Ashcroft and N. D. Mermin, *Solid State Physics* (Philadelphia, PA: Holt Saunders, 1976).
166. X. Wang, A. Bhattacharjee, and S. Hu, *Phys. Rev. Lett.* **86**, 2569 (2001).
167. A. Homann, A. Melzer, R. Madani, and A. Piel, *Phys. Lett. A* **242**, 173 (1998).
168. S. V. Vladimirov, P. V. Shevchenko, and N. F. Cramer, *Phys. Rev. E* **56**, R74 (1997).
169. H. Goldstein, *Classical mechanics* (New Delhi, PA: Narosa Publishing House, 1985).
170. W. Fogle, and H. Perlstein, *Phys. Rev. B* **6**, 1402 (1972).
171. M. Charalambous, J. Chaussy, and P. Lejay, *Phys. Rev. B* **45**, R5091 (1992).
172. S. Bhattacharya and M. J. Higgins, *Phys. Rev. Lett.* **70**, 2617 (1993).
173. T. Nattermann, S. Stepanow, L. H. Tang, and H. Leschom, *J. Phys. I* **2**, 1483 (1992).
174. O. Narayan and D. S. Fisher, *Phys. Rev. B* **48**, 7030 (1993).
175. W. G. Hoover, *Phys. Rev. A* **31**, 1695 (1985).
176. R. Kubo, M. Toda, and N. Hashitume, *Non Equilibrium Statistical Mechanics* (Springer-Verlag, Berlin, 1992).
177. Y. Cao, J. Zhengkuan, and H. Ying, *Phys. Rev. B* **62**, 4163 (2000).
178. R. Mannella, *Int. J. Mod. Phys. C* **13**, 1177 (2002).
179. P. Drude, *Ann. Phys. (Leipzig)* **1**, 566 (1900).

180. Y. Cao, Z. Jiao, and H. Ying, *Phys. Rev. B* **62**, 4163 (2000).
181. Y. Cao and Z. Jiao, *Physica C* **321**, 177 (1999).
182. E. H. Brandt, *Phys. Rev. Lett.* **50**, 1599 (1983).
183. A. Tonomura, H. Kasai, O. Kamimura, T. Matsuda, K. Harada, J. Shimoyama, K. Kishio, and K. Kitazawa, *Nature (London)* **397**, 308 (1999).
184. H. J. Jensen, A. Brass, and A. J. Berlinsky, *Phys. Rev. Lett.* **60**, 1676 (1988); M. C. Faleski, M. C. Marchetti, and A. A. Middleton, *Phys. Rev. B* **54**, 12427 (1996).
185. C. J. Olson, C. Reichhardt, and F. Nori, *Phys. Rev. Lett.* **81**, 3757 (1998).
186. O. Narayan and D. S. Fisher, *Phys. Rev. Lett.* **68**, 3615 (1992).
187. C. R. Myers and J. P. Sethna, *Phys. Rev. B* **47**, 11171 (1993).
188. A. Pertsinidis and X. S. Ling, *Bull. Am. Phys. Soc.* **46**, 181 (2001);
189. A. A. Middleton and N. S. Wingreen, *Phys. Rev. Lett.* **71**, 3198 (1993).
190. D. Carpentier and P. Le Doussal, *Phys. Rev. Lett.* **81**, 1881 (1998).
191. S. Bhattacharya and M. J. Higgins, *Phys. Rev. B* **49**, 10005 (1994).
192. M. C. Hellerqvist, D. Ephron, W. R. White, M. R. Beasley, and A. Kapitulnik, *Phys. Rev. Lett.* **76**, 4022 (2003).
193. R. Besseling, N. Kokubo, and P. H. Kes, *Phys. Rev. Lett.* **91**, 177002 (2003).
194. L. Sneddon, M. C. Cross, and D. S. Fisher, *Phys. Rev. Lett.* **49**, 292 (1982).
195. A. Schmidt and W. Hauger, *J. Low Temp. Phys.* **11**, 667 (1973).
196. J. Watson and D. S. Fisher, *Phys. Rev. B* **55**, 14909 (1997).